

# **The Star Forming Core of Mon R2**

Jean Giannakopoulou

Submitted in partial fulfillment  
of the requirements for the degree of  
Master of Science

Saint Mary's University  
Halifax, Nova Scotia  
September 1993

Copyright Jean Giannakopoulou 1993



National Library  
of Canada

Acquisitions and  
Bibliographic Services Branch

395 Wellington Street  
Ottawa, Ontario  
K1A 0N4

Bibliothèque nationale  
du Canada

Direction des acquisitions et  
des services bibliographiques

395, rue Wellington  
Ottawa (Ontario)  
K1A 0N4

*Your title / Votre référence*

*Our title / Notre référence*

**The author has granted an irrevocable non-exclusive licence allowing the National Library of Canada to reproduce, loan, distribute or sell copies of his/her thesis by any means and in any form or format, making this thesis available to interested persons.**

**L'auteur a accordé une licence irrévocable et non exclusive permettant à la Bibliothèque nationale du Canada de reproduire, prêter, distribuer ou vendre des copies de sa thèse de quelque manière et sous quelque forme que ce soit pour mettre des exemplaires de cette thèse à la disposition des personnes intéressées.**

**The author retains ownership of the copyright in his/her thesis. Neither the thesis nor substantial extracts from it may be printed or otherwise reproduced without his/her permission.**

**L'auteur conserve la propriété du droit d'auteur qui protège sa thèse. Ni la thèse ni des extraits substantiels de celle-ci ne doivent être imprimés ou autrement reproduits sans son autorisation.**

ISBN 0-315-84894-4

**Canada**

## TABLE OF CONTENTS

TABLE OF CONTENTS.....	i
THE EXAMINING COMMITTEE.....	iii
ACKNOWLEDGMENTS.....	iv
ABSTRACT.....	v
LIST OF TABLES.....	vi
LIST OF FIGURES.....	vii
I. INTRODUCTION.....	1
a. Star formation.....	1
b. Molecular outflows.....	4
c. Summary of previous work on the Mon R2 region.....	8
i) General description of the molecular cloud.....	8
ii) Outflow(s).....	11
iii) Structure of the cloud core: studies of emission lines from molecules.....	14
1) CS.....	15
2) HCN.....	16
3) H <sub>2</sub> CO.....	16
4) NH <sub>3</sub> .....	17
5) HCO <sup>+</sup> .....	18
iv) H II region.....	19
v) Infrared cluster.....	24
1) IRS 1.....	25
2) IRS 2.....	27
3) IRS 3.....	27
4) Other infrared sources.....	30
II. OBSERVATIONS.....	32
a. Data.....	32
b. Comments on the CO line shapes.....	40
III. MORPHOLOGY OF THE GAS.....	42
IV. DERIVATION OF PHYSICAL PARAMETERS.....	58
a. Optical depth.....	58
b. Excitation temperature.....	60
c. Column density.....	60
d. Mass.....	63
e. Excitation temperature and mass in the optically thin limit.....	64

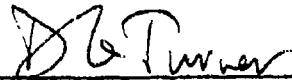
V. ANALYSIS OF OBSERVATIONS.....	67
a. Optical depth versus velocity.....	67
b. Excitation temperature versus velocity.....	73
c. Column density of CO versus velocity.....	82
d. Mass and other properties of the high-velocity clumps.....	89
e. Energetics of the clumps and implications for the cloud core.....	97
VI. DISCUSSION.....	104
a. Comparison of our CO map with other work.....	104
i) Comparison of a 2.2 $\mu\text{m}$ image with the CO clump distribution.....	104
ii) The CO clump distribution compared with maps of other molecules.....	106
1) HCN.....	106
2) H <sub>2</sub> CO.....	109
3) CS and HCO <sup>+</sup> .....	112
4) NH <sub>3</sub> .....	115
iii) Comparison of CO clump distribution with sub-millimeter and millimeter continuum maps.....	117
iv) Comparison of the column densities calculated from absorption lines in <sup>13</sup> CO with those obtained from CO emission lines.....	129
b. CO high-velocity clumps and the large-scale CO outflow.....	137
VII. CONCLUSIONS.....	142
REFERENCES.....	146
CIRRICULUM VITAE.....	151

THE EXAMINING COMMITTEE



---

Dr. G. F. Mitchell  
Professor of Astronomy  
Saint Mary's University  
(Thesis Supervisor)



---

Dr. D. G. Turner  
Professor of Astronomy  
Saint Mary's University



---

Dr. G. A. Welch  
Professor of Astronomy  
Saint Mary's University



---

Dr. T. I. Hasegawa  
Department of Astronomy  
Saint Mary's University

## ACKNOWLEDGMENTS

These acknowledgments are not meant to cover this thesis alone, but to include the entire experience of my Masters' degree. Above all I would like to express my gratitude to Dr. George F. Mitchell who provided the primary inspiration and encouragement, and shared not only his ideas about physics but also his philosophy about life. I am grateful to Dr. Gary A. Welch, for his comments on the text of this thesis, and for what I learned from him, and to Dr. David G. Turner for his suggestions on how to improve the text. I would like to thank Dr. Tatsuhiko I. Hasegawa for his insights on the subject matter of my thesis and for his encouragement during my defense.

Of my friends, there are four in particular who should be mentioned, without whose support and help it would not have been possible for me to complete this degree. First of all, I am very grateful to Linda Baker not only for her contribution to the aesthetics of my thesis, but also for her constant support during the past two years. Jeremy Beckett, besides putting up with me when I was under severe stress, added some poetry in my life. I am grateful to Shawn Young who is always supportive and one of the best listeners I have ever met. Last, but certainly not least, I want to thank Jonathan Druid Dursi for all his care and help, which were especially critical during the final phase of the thesis.

My fellow graduate students, Melvin Blake, Yonghui Xie, Lifang Ma and Georgi Mandushev enriched my cultural experiences. I would like to thank them for their friendship, and to wish them all every success in their academic careers and personal lives.

Finally, I am grateful to my family and to many people that in one way or another over the past two years, through their love and assistance, have contributed to this degree. Many thanks to all.

## ABSTRACT

In this thesis, the nature of the star forming core of the Mon R2 cloud is investigated using new, high spatial resolution observations. The new data include: maps of  $^{12}\text{CO}$   $J=3\rightarrow 2$ , HCN  $J=4\rightarrow 3$  and  $\text{H}_2\text{CO}$   $J_{K_1, K_2} = 5_{1,5} \rightarrow 4_{1,4}$ , spectra of  $^{12}\text{CO}$   $J=2\rightarrow 1$  and  $^{13}\text{CO}$   $J=3\rightarrow 2$  at 12 positions, an infrared M-band spectrum, and finally sub-millimeter and millimeter continuum maps (450  $\mu\text{m}$ , 800  $\mu\text{m}$ , 1100  $\mu\text{m}$  and 1300  $\mu\text{m}$ ).

Based on the spatial distribution of the intensity of the  $^{12}\text{CO}$   $J=3\rightarrow 2$  transition, we present a qualitative description of the region which consists of complexes and clumps. The complexes surround a central area of lower intensity which corresponds to the compact H II region in the cloud core. The radiation from the sub-millimeter and millimeter continuum maps is believed to be due to thermal emission from dust, located in and around the H II region. Some differences between the maps are believed to be due to the increasing importance in the millimeter maps of free-free emission from ionized gas.

The complexes incorporate 13 smaller intensity peaks (clumps), which have large masses (2.7 to 0.007  $M_{\odot}$ ) and large velocity dispersions (typically 30 km/s). The CO clumps are not distributed in a bipolar fashion. They probably formed from the interaction of the large outflow with the ambient gas. The source of the outflow is not clearly identified. We propose that the outflow could originate from IRS 3, which has gone through a quiescent phase.

The CO excitation temperature,  $T_{\text{ex}}$ , varies between 5 and 60 K. Although the CO  $J=3\rightarrow 2$  transition can locate the position of the dense gas, it misses a large fraction of the dense quiescent gas (70-80%) due to self-absorption.

The sum of the magnetic and the gravitational energy ( $12 \times 10^{45}$  erg) is somewhat smaller than the total kinetic energy of the inner core of the Mon R2 cloud ( $15 \times 10^{45}$  erg), and, hence, the core is either in the process of disruption or in dynamical equilibrium.

## LIST OF TABLES

Table I	Coordinates of the 12 Observed Positions in the $^{12}\text{CO}$ $J=2\rightarrow 1$ and $^{13}\text{CO}$ $J=3\rightarrow 2$ Transitions.....	35
Table II	Characteristics of the High-Velocity Clumps Seen in the $^{12}\text{CO}$ $J=3\rightarrow 2$ Map.....	57
Table III	Excitation Temperatures for the 12 Positions.....	77
Table IV	Masses of the CO Clumps.....	92
Table V	Molecular Hydrogen Number Density of the CO Clumps.....	94
Table VI	Energetics of Clumps.....	99
Table VII	Possible Associations of CO Clumps with Continuum Clumps and Infrared Sources.....	129
Table VIII	$^{13}\text{CO}$ $v=0\rightarrow 1$ Absorption Lines in Mon R2 IRS 3.....	134

## LIST OF FIGURES

Figure 1	$^{12}\text{CO}$ J=1 $\rightarrow$ 0 Contour Map of the Mon R2 Cloud.....	10
Figure 2	$^{12}\text{CO}$ J=1 $\rightarrow$ 0 Contour Map of the Outflow .....	13
Figure 3	Model of the Brightness Distribution of the H II region.....	23
Figure 4	1.65, 2.2, 10 and 20 $\mu\text{m}$ Maps of the Infrared Cluster.....	26
Figure 5	2.2 $\mu\text{m}$ Contour Map and Polarization Vector Map of the Infrared Cluster.....	28
Figure 6	1.65 $\mu\text{m}$ to 20 $\mu\text{m}$ Energy Distributions of IRS 2 and IRS 3.....	29
Figure 7	$^{12}\text{CO}$ J=3 $\rightarrow$ 2 Spectral Line Map.....	33
Figure 8	$^{12}\text{CO}$ J=3 $\rightarrow$ 2 and $^{13}\text{CO}$ J=3 $\rightarrow$ 2 Spectral Lines.....	36
Figure 9	$^{12}\text{CO}$ J=2 $\rightarrow$ 1 Spectral Lines.....	38
Figure 10	Contour Map of the Integrated Intensity of the $^{12}\text{CO}$ J=3 $\rightarrow$ 2 Emission....	43
Figure 11	Contour Channel Maps of the $^{12}\text{CO}$ J=3 $\rightarrow$ 2 Emission.....	44
Figure 12	Optical Depth of $^{13}\text{CO}$ Versus Velocity for the 12 Positions.....	68
Figure 13	Uncertainties (%) in the Optical Depth and in the Excitation Temperature Versus Velocity.....	72
Figure 14	Excitation Temperature Versus Velocity for the 12 Positions.....	74
Figure 15	Superposition of all Excitation Temperature Versus Velocity Plots.....	78
Figure 16	Excitation Temperature at Position 4 (-10", 60").....	80
Figure 17	Column Density Versus Velocity for the 12 Positions.....	83
Figure 18	Uncertainties (%) in the Optical Depth, the Excitation Temperature and the Column Density Versus Velocity.....	86
Figure 19	$T_{\text{ex}} \exp(33.18/T_{\text{ex}})$ Versus Excitation Temperature.....	88
Figure 20	Spatial Distribution of the CO Clumps.....	96
Figure 21	Distribution of the CO Clumps Superimposed on a 2.2 $\mu\text{m}$ Image.....	105

Figure 22	Integrated Intensity Maps of HCN $J=4 \rightarrow 3$ Emission.....	107
Figure 23	Integrated Intensity Maps of H <sub>2</sub> CO $J_{K_a, K_c} = 5_{1,3} \rightarrow 4_{1,3}$ Emission.....	110
Figure 24	Superposition of the CO Clumps on an HCO <sup>+</sup> Map.....	113
Figure 25	Superposition of the CO Clumps on a NH <sub>3</sub> Map.....	117
Figure 26	870 $\mu$ m and 1300 $\mu$ m Continuum Maps.....	119
Figure 27	450 $\mu$ m, 800 $\mu$ m, 1100 $\mu$ m and 1300 $\mu$ m Continuum Maps.....	121
Figure 28	Superposition of the CO Clumps on our 800 $\mu$ m Map.....	123
Figure 29i	Superposition of the 1.3 cm continuum map on our 450 $\mu$ m Map.....	126
Figure 29ii	Superposition of the 1.3 cm continuum map on our 1100 $\mu$ m Map.....	127
Figure 30	Infrared M-band Fundamental Absorption Spectrum in <sup>13</sup> CO.....	133
Figure 31	Excitation Diagram for <sup>13</sup> CO.....	135
Figure 32	Bipolarity of Diffuse Component.....	139
Figure 33	CO Clump Mass Versus the Bulk Velocity.....	141

## I. INTRODUCTION

### a. Star formation

Molecular clouds are considered to be the main star forming sites (Zuckerman et al. 1976). However, if the characteristic values of density ( $n_{\text{H}_2} = 10^3\text{-}10^6 \text{ cm}^{-3}$  or more) and radius (5-10 parsecs) are taken into account, then clearly these values must change by many orders of magnitude to become comparable with those of a typical star. The obvious physical process that could be responsible for the necessary compression is the gravitational collapse of the cloud. If the cloud is dense enough to be unstable against gravitational collapse, then the self-shielding of the gas from external ultraviolet photons will be adequate to maintain a cold molecular core. Less dense clouds can be invaded by ultraviolet photons which have enough energy to dissociate molecular hydrogen and to warm the cloud core.

In a quantitative analysis it is useful to assume that the only force that acts on the molecular cloud is its gravitational force, ignoring magnetic fields, rotation and external pressure from the surrounding gas. The cloud will contract provided the gravitational energy is larger than its internal kinetic energy. If the relative magnitude of the internal pressure is small, then the cloud will undergo a free-fall collapse. According to Dyson and Williams (1980), for collapse to occur the free-fall time must be less than the time taken

for the information that the pressure is increasing to travel across the cloud (at the speed of sound  $v_s$ ). If the cloud has a uniform density  $\rho_0$ , then the critical mass for the cloud to collapse is given by the Jeans mass:

$$M_{\text{crit}} = \sqrt{\frac{3\pi^5}{32}} v_s^3 G^{-3/2} \rho_0^{-1/2},$$

where  $G$  is the gravitational constant.

From this oversimplified scenario we find that the critical mass for cool molecular clouds (typically  $n_{\text{H}_2} = 5 \times 10^3 \text{ cm}^{-3}$  and  $T = 20 \text{ K}$ ) is about 30 solar masses ( $M_{\odot}$ ), which corresponds to a critical radius of 0.3 parsecs (pc). Since molecular clouds are typically several parsecs in size, such a small critical radius indicates that a molecular cloud could contain many subsections which collapse independently; this would also explain the observed tendency of stars to form in groups. As a subsection starts collapsing, the critical mass decreases as the density increases, and therefore, the cloud will separate into even smaller entities. This hierarchical fragmentation will not continue indefinitely. The lower limit for the mass will be set by the increasing gas opacity which will not allow the thermal radiation from the gas and the dust to escape. Not only will the temperature of these fragments rise, but also their sound speed and their critical mass will increase, since the latter is proportional to the sound speed. Models that propose a clumpy structure for molecular clouds (Norman and Silk 1980; Blitz and Shu 1980) imply that a cloud with clumps forms stars on small scales but is quite resistant to overall collapse. Therefore, it is not surprising that a large-scale collapse of a molecular cloud has never been observed.

It should be obvious that the formation of real stars is an extremely complicated process. A comparison of the observed star forming efficiency of 2% with the predicted one of 20-50% [Lada et al. (1984)] shows that mechanisms that slow down or stop the collapse must be sought. The most promising mechanism is associated with the presence of magnetic fields in the molecular clouds. The ions in these clouds, although they are relatively few (1 part in  $10^7$ ), are the only species that are affected by magnetic fields. As the neutral particles succumb to gravitational forces, they are slowed down due to friction with the ions controlled by the magnetic field. There are other factors that also need to be taken into account, for example, turbulence and the rotation of the cloud. They undoubtedly contribute to supporting the cloud cores, but are not thought to be the major supporting mechanisms. Observations indicate (Shu et al. 1987) that the rotation rates of the cloud cores are too small to stabilize them. Furthermore, turbulence would dissipate on short time scales (500,000 years).

Despite the supporting mechanisms, the clouds form condensations. What processes might then lead these new condensations to star formation? The condensation that will eventually form a star collapses in a highly non-uniform, "inside-out" manner, forming another condensed configuration. Because the core possesses angular momentum, it forms a central protostar with a disk in its equatorial plane; both are deeply embedded in the still-infalling envelope of dust and gas.

As time proceeds more of the rotating and inflowing material will fall preferentially onto the disk. Observations indicate that T Tauri stars are

usually found distributed throughout dense molecular clouds. This is not always the case for stars of higher mass. Some prominent high-mass protostars, such as GL 490 and GL 2591, are at the centre of their cloud. Many cases of high-mass protostars, however, seem to form in a sequential fashion from one edge of the molecular cloud to another, for example Cepheus OB 3, W5 and W4 (Elmegreen 1992). The Mon R2 region contains many B stars. When one group of its B stars evolves, it can ionize the surrounding gas, thus creating H II regions. As the H II region expands, it compresses more gas, increasing the density. This leads to the next generation of massive stars. Although there are no published data that indicate that the stars in the Mon R2 cloud have formed sequentially, it should be noted that the compact H II region seen in the cloud core compresses the gas around the H II region, as will be seen in our CO observations.

## b. Molecular outflows

From the previous discussion one would expect to find mass inflow in star forming regions, however, the observations came as a surprise. Zuckerman et al. (1976), for example, found in a small region in the Orion Molecular Cloud that the width of the CO emission lines was 180 km/s\*. This velocity is much larger than that observed throughout the cloud (5 km/s) and, of course, supersonic since the speed of sound is approximately a few  $\times$  0.1 km/s. Moreover, one of the most intriguing characteristics that emerge

---

\* The notation km/s will be used for units of velocity rather than km s

from many observations of the gas motions in star forming regions is their bipolarity, i.e. the receding gas (red-shifted) is spatially displaced with comparison to the approaching (blue-shifted) gas.

These motions could in principle be interpreted as any of the following: collapse, rotation, expansion, or turbulence. Rotation can be ruled out by the presence of very high velocities over relatively large areas, because they would indicate the presence of masses  $\approx 10^4 M_{\odot}$  versus the observed  $100 M_{\odot}$ . Furthermore, the bipolarity of the moving gas makes collapse and turbulence highly unlikely candidates for explaining the nature of the gas motion, because it is hard to imagine collapse happening in a collimated fashion. The consensus is that these motions show the presence of molecular outflows. At least 150 molecular outflows are now known (Fukui 1989).

Lada (1985) distinguishes three types of outflows: bipolar (73% of his sample of 41 outflows), symmetrical (10%) and monopolar (17%). Symmetrical outflows show approaching and receding gas in the same region, while monopolar outflows show either approaching or receding gas. Most outflows are bipolar; this is the case for the outflow seen in Mon R2.

We can summarize other physical properties of the outflows. Their dimensions are typically between 0.1 and 4 pc and their masses range between 0.1 and  $100 M_{\odot}$ . The energy of these outflows derived from the observed masses and velocities is enormous,  $10^{43}$ - $10^{48}$  ergs (Snell 1987). The dynamical time scales for various outflows, simplistically approximated by the ratio of the outflow's size to its radial velocity, range between  $10^3$  and  $10^5$  years, with a canonical value of  $10^4$  years.

This brings up the issue of where and with what rate these outflows occur. Since the typical age of an outflow is  $2 \times 10^4$  years, this leads to a rate of birth of outflow progenitors of  $1.1 \times 10^{-3} \text{ years}^{-1} \text{ kpc}^{-2}$  (Snell 1987), which is comparable to the rate of star formation of all stars more massive than the Sun. This is an indication that all stars with  $M > M_{\odot}$  undergo mass loss via molecular outflows. Furthermore, the statistics permit all stars to go through an outflow phase.

The most popular idea for explaining these outflows is associated with the presence of an ionized stellar wind, created by a young stellar object or by an accretion disk surrounding the object. The wind accelerates the ambient gas creating perhaps a thin shell of swept-up material at the interface of the wind with the molecular cloud. One of the aims of the observations discussed in this thesis is to identify the stellar source of the outflow. However, none of the known infrared objects in the Mon R2 core can be clearly labeled as the source. We suggest that IRS 3 could be responsible for the large outflow.

It is useful to compare the energy supplied by the ionized wind with the energy of the outflow. In most cases the luminous energy of the wind is smaller than that of the outflow. Lada (1985) suggests this may be because: (i) the winds are variable with time and they are observed as they are going through their quiet phase, (ii) there is an important neutral component which carries most of the wind momentum and energy, or (iii) the wind velocities are underestimated. Although there is no overwhelming proof for any of these hypotheses, there is evidence that a fast neutral atomic wind

exists in some outflows, for example NGC 2071 (Bally and Stark 1983), HH7-11 (Lizano et al. 1988), DR 21 (Russell et al. 1992), and L1551 (van der Werf et al. 1989; Giovanardi et al. 1992). To our knowledge there has been no search for a neutral wind in the Mon R2 cloud.

Another important problem is the collimation mechanism for the outflow. There are at least three proposed mechanisms. First, the collimated outflow may be due to a bipolar wind originating at the surface of the protostar or in the surrounding accretion disk. Alternatively, a flattened density distribution may be able to collimate an initially spherical wind into two opposite jets (Königl 1982; Torrelles et al. 1983). Both of these mechanisms predict that the dense gas should have a disk-like morphology with a symmetry axis parallel to the flow. A third possible mechanism to cause bipolar outflows is related to the hydromagnetic winds which originate in the envelopes of rotating, magnetized disks (Pudritz and Norman 1983; Pudritz 1985). Although we will not address the collimation issue for the CO outflow seen in the Mon R2 cloud, it should be noted that our CO, HCN and H<sub>2</sub>CO observations do not show a flattened structure around IRS 3 or any of the other luminous infrared sources.

### c. Summary of previous work on the Mon R2 region

#### *d) General description of the molecular cloud*

Mon R2 (galactic coordinates are  $l = 216^\circ$  and  $b = -12^\circ$ ) is an association of stars illuminating nine reflection nebulae and was first identified by van den Bergh (1966). The nebulae lie chiefly along a line running roughly east-west about  $2^\circ$  (30 pc) in length. Four of the nebulae correspond to NGC objects: NGC 2185, NGC 2183, NGC 2182 and NGC 2170 (Tirion et al. 1992).

The distance to the reflection nebulae derived initially by Racine (1968) was 830 pc. In 1970, this value was revised to 950 pc by Racine and van den Bergh (1970). However, Herbst and Racine (1976) conclude that  $(830 \pm 50)$  pc is the best determined distance, and this value is used here, unless otherwise stated. These authors presented photometric data for 29 stars in the Mon R2 association and concluded that the reflection nebulae are illuminated by zero-age main-sequence (ZAMS) B1-B9 stars. From an Hertzsprung-Russell diagram of stars in the region, Herbst and Racine proposed that star formation began in the Mon R2 cloud between 6 and 10 million years ago.

The reflection nebulae seem to have formed in a molecular cloud, which is frequently referred to as Mon R2. This cloud was discovered when Loren et al. (1974) detected CO in emission across the more optically obscured parts of the region. Kutner and Tucker (1975) presented CO  $J=1 \rightarrow 0$  emission observations of a  $3'.5 \times 3'.5$  region using a beam width of  $2'.6$ . The strongest

peak ( $T_R = 31$  K) in CO emission lies among three reflection nebulae vdB68, vdB69 and NGC 2170, and is not identified with any of them.

A more complete survey in CO  $J=1 \rightarrow 0$  was conducted by Maddalena et al. (1986). The beam was larger than that of Kutner and Tucker, but the sampling was more thorough. Figure 1 indicates that the Mon R2 cloud is an elliptical giant molecular cloud with dimensions of  $7^\circ.6 \times 2^\circ.8$  (110 pc  $\times$  40 pc). It is situated approximately 150 pc south of the galactic plane and its major axis lies approximately parallel to the plane. Hughes and Baines (1985) note that the reflection nebulae and the H II regions in this cloud have a remarkable distribution: 28 out of the 30 objects are confined to a narrow strip that is  $0^\circ.5$  (7 pc) wide and  $8^\circ$  (115 pc) long.

Maddalena et al. estimated that the mass of the cloud is  $0.9 \times 10^5 M_\odot$ . This value is consistent with the spatially limited CO surveys of Kutner and Tucker ( $M > 0.32 \times 10^5 M_\odot$  for an area of  $3^\circ.5 \times 3^\circ.5$ ) and Loren ( $M = 0.23 \times 10^5 M_\odot$  for an area of  $20' \times 35'$ ) if the uncertainties are considered.

We will not emphasize the characteristics of the whole Mon R2 cloud, but will focus on some of the interesting features that are associated with the core of the cloud. The most prominent feature is a very large molecular outflow detected in CO. The core also contains a compact H II region and H<sub>2</sub>O and OH masers (Downes et al. 1975). Finally, there is an infrared cluster located in the cloud core, the nature of which needs to be investigated. All of these phenomena are indications that the cloud is a site of recent, possibly ongoing, star formation, which makes this region so interesting.

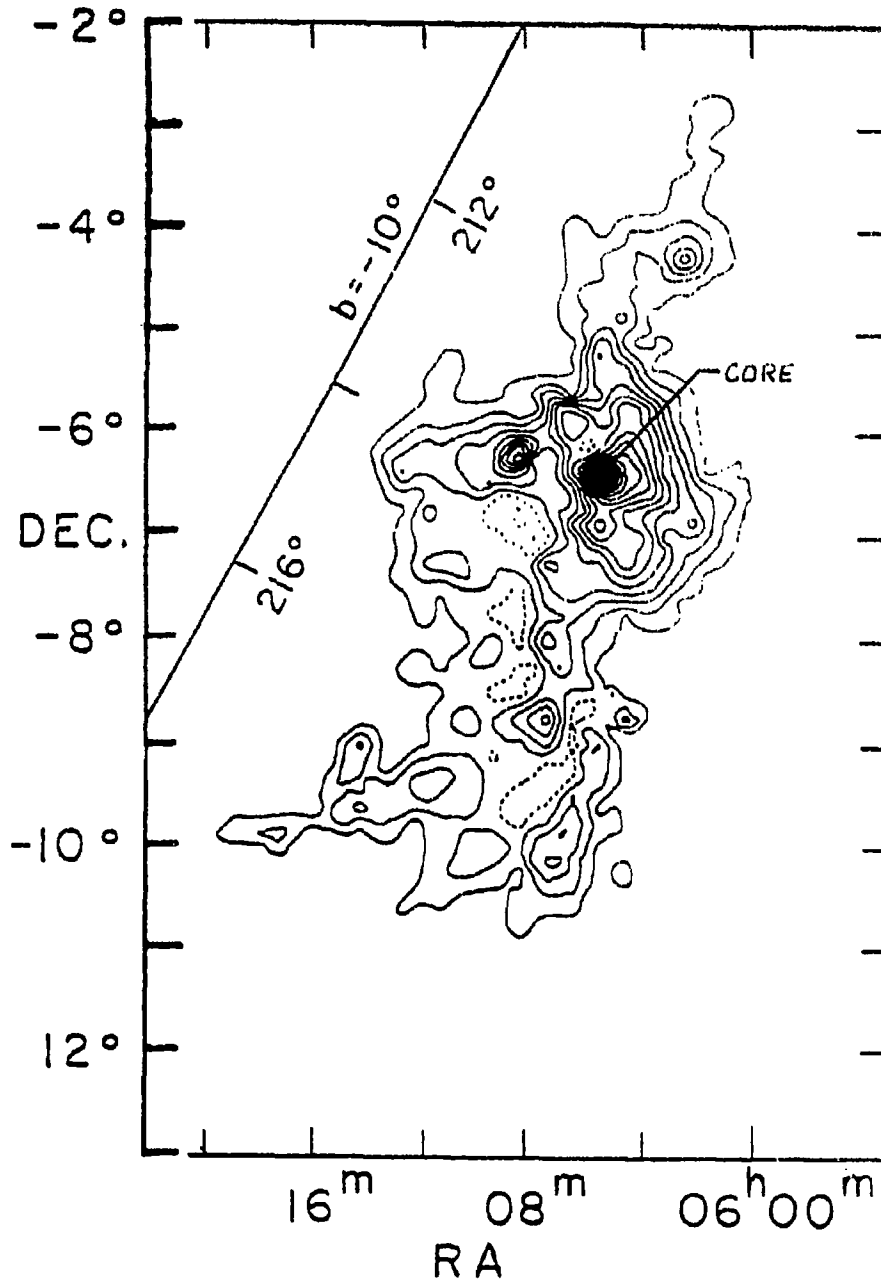


**Fig. 1** The Mon R2 cloud mapped in CO  $J=1 \rightarrow 0$ . The interval between contours is 2.6 K km/s and the lowest contour level is at 1.5 K km/s (adapted from Maddalena et al. 1986).

The CO outflow is discussed in section (ii), the structure of the cloud core from molecular studies is presented in section (iii), the compact H II region is described in section (iv), and the infrared cluster is considered in section (v).

### ii) Outflow(s)

Loren et al. (1974) were the first to detect  $^{12}\text{CO}$  and  $^{13}\text{CO}$   $J=1\rightarrow 0$  emission in the Mon R2 region. Many CO observations followed because this study indicated broad line wings in the CO spectra, which suggested the presence of high-velocity gas. Studies of the Mon R2 region in CO  $J=1\rightarrow 0$  include those of Snell and Loren (1977), Loren (1977), and Bally and Lada (1983). In what follows, we focus on more recent studies.

Wolf et al. (1990) mapped the Mon R2 region in  $J=1\rightarrow 0$  transitions of  $^{12}\text{CO}$ ,  $^{13}\text{CO}$  and  $\text{C}^{18}\text{O}$  with a beam width of approximately  $90''$ . They concluded that the velocity components around the infrared cluster show bipolar symmetry and are spatially fairly distinct (although the approaching and receding gas overlap close to the origin). These two characteristics suggest that the presence of receding and approaching gas is the result of a collimated molecular outflow. They also note that the Mon R2 outflow extends over  $28'$  (6.8 pc), which makes it one of the largest outflows. The dynamical time scale ( $t_d$ ) for the outflow is computed by Wolf et al. as the ratio of the average dimension of the outflow over its characteristic velocity. These authors find that  $t_d = 10^5$  years.

According to Wolf et al., the mass of the outflow is about  $180 M_{\odot}$  and approximately 50% of the surrounding ambient molecular cloud has been swept up by the outflow during the course of its evolution. The outflow has an unusual, bent morphology and is roughly parallel to the direction of the magnetic field in the cloud. The receding gas is spatially more confined in the plane of the sky than the approaching gas, which could be due to the geometry of the flow.

Observations at a somewhat higher resolution (beam width of  $60''$ ), covering a  $10' \times 20'$  area of the Mon R2 outflow, are discussed by Meyers-Rice and Lada (1991) (Figure 2). Their CO  $J=1 \rightarrow 0$  map suggests that the outflow consists of two distinct pairs of bipolar lobes which partially overlap. The observed velocity in two of the four lobes increases with the projected distance from the flow centre, which they assume to be IRS 1. These authors explain this linear expansion law as self-sorting of the flow material, which is driven by a more or less steady force or wind. If a steady force is applied to a medium consisting of clumps of differing mass and size, then clumps of the smallest dimension and mass would experience the greatest acceleration and move farthest from the central source with time. It should be noted, however, that our higher resolution observations do not indicate that the CO gas in the core of the Mon R2 cloud is distributed according to its velocity.

Meyers-Rice and Lada propose that the Mon R2 flow cannot be described easily by a single collimated flow. They suggest that the flow consists of the superposition of two physically distinct bipolar outflows which independently originate from separate infrared sources in the cluster of young stellar objects at the centre of the outflow activity. One of these flows

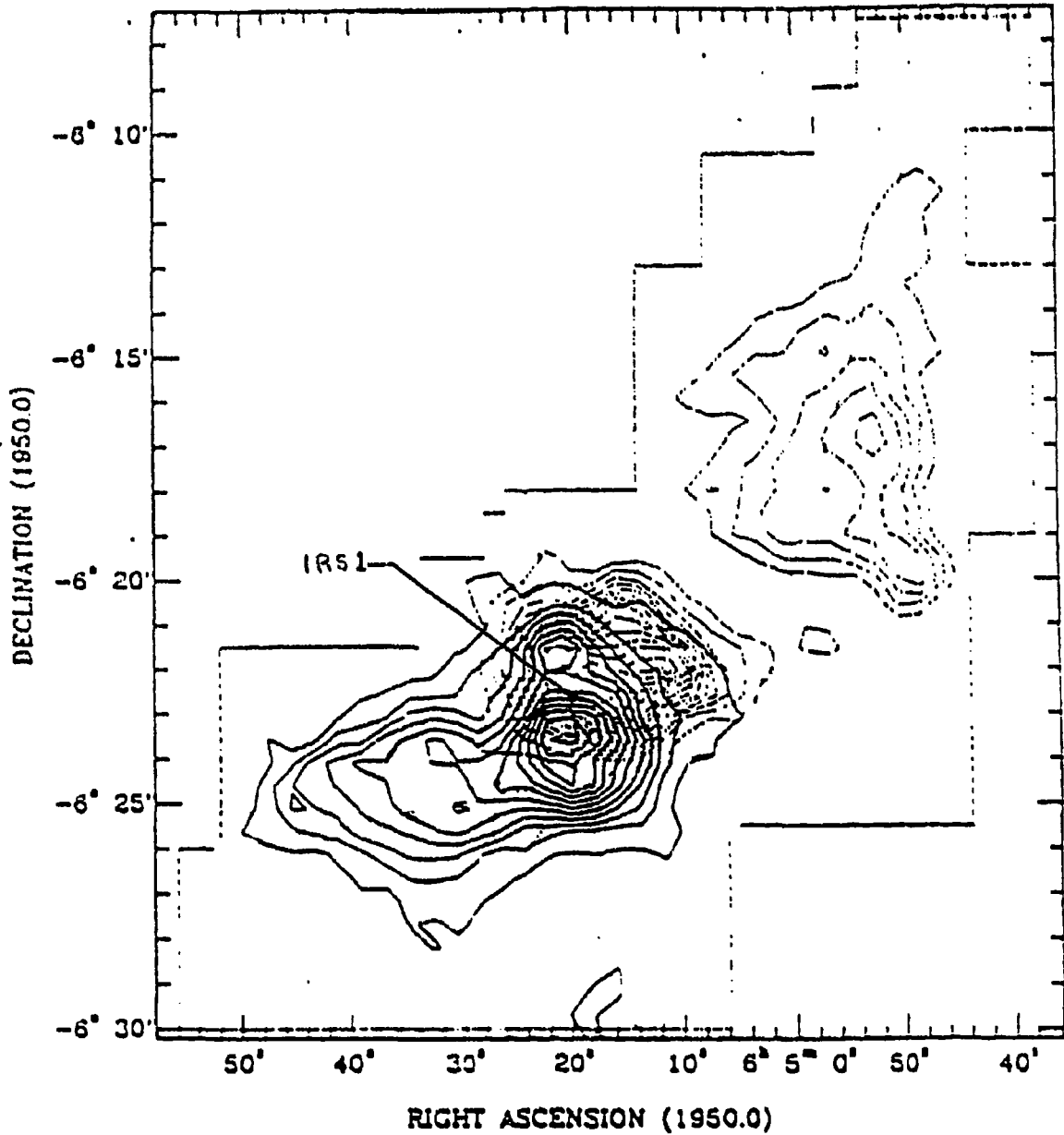


**Fig. 2** An integrated intensity CO  $J=1 \rightarrow 0$  contour map (60" beam): The contours of emission from receding gas are solid and from approaching gas are dashed. The position of IRS 1 is marked. Both maps have their lowest contour level at 10 K km/s, and the interval between contours is 5 K km/s and 10 K km/s respectively. Meyers-Rice and Lada suggest that the flow consists of two physically distinct bipolar outflows which originate from separate infrared sources (adapted from Meyers-Rice and Lada 1991)

(Mon R2a) consists of extended lobes and is collimated to some extent. The other flow (Mon R2b) consists of two compact lobes and is poorly collimated. The higher outflow velocities present in this second, compact flow suggest that its poor collimation might be due to a small angle of inclination with respect to the line of sight and that its major axis is roughly orthogonal to that of the more extended and collimated outflow. Our CO observations indicate that there is a bipolar diffuse component consistent with Mon R2a. However, the complicated velocity structure revealed by our observations suggests that the gas motions are probably more complex than one would expect from a superposition of two outflows.

iii) Structure of the cloud core: studies of emission lines from molecules

A measurement of the excitation of interstellar molecules can provide a means of determining physical conditions in molecular clouds. In particular, the measurement of a number of transitions of a single molecular species provides our only generally applicable method of determining the molecular hydrogen densities within these clouds. Molecular hydrogen densities, as determined by measurements on different clouds and different molecules within an individual cloud, are known to vary over a range of several orders of magnitude ( $10^3$ - $10^6$  cm<sup>-3</sup>). This is found by exploiting the range of critical densities for different species.

Besides <sup>12</sup>CO, very important information can be obtained from <sup>13</sup>CO, which is not only useful for studying the gas kinematics but also provides an

estimate of the total gas mass. The central region of the Mon R2 cloud was first mapped in the  $^{13}\text{CO } J=1 \rightarrow 0$  (110 GHz) transition by Loren (1977) with a beam width of 2'.6. Montalban et al. (1990) mapped an area of 20' x 16' in the same transition with a beam width of 4'.4.

The molecular cloud has been mapped in the emission lines of various other molecular species besides CO. Other species are detectable only in the denser part of the cloud, with dimensions of approximately 10' x 10' or less, depending on the molecule in question. In what follows, we emphasize observations that are comparable to our CO observations of the cloud core (radius  $\cong 1'$ ).

#### 1) CS

Many low resolution studies have been made in CS: Kutner and Tucker (1975), Linke and Goldsmith (1980), and Montalban et al. (1990). One such study by Heyer et al. (1986) showed that the strongest CS  $J=2 \rightarrow 1$  emission peak in the map (beam width of 56") was located near the position of the infrared sources and extended towards the west. The radius of the region was about 1' (0.24 pc). They also obtained a map of the CS  $J=5 \rightarrow 4$  (245 GHz) emission (beam width of 22") within the central 1' cloud core of Mon R2. This high rotational transition probes densities on the order of  $10^6 \text{ cm}^{-3}$ . For this inner region the density Heyer et al. calculated is  $5-10 \times 10^5 \text{ cm}^{-3}$ . Both maps are featureless. This region of 1' radius defined by the CS emission is considered in what follows to be the core of the Mon R2 cloud. It is in this central core where the CO emission peaks, according to our new observations.

Wolf et al. (1990) present CS observations of  $J=2 \rightarrow 1$  emission with a beam width of  $1'.9$  and of  $J=5 \rightarrow 4$  emission with a beam width of  $23''$ . The dense CS core surrounds the infrared cluster at the origin of the CO outflow [discussed further in subsection (v) below]. These authors infer that the core may have a flattened structure, but the evidence is hardly compelling. A comparison of the spatial distributions of emission from the  $J=2 \rightarrow 1$  and  $J=5 \rightarrow 4$  transitions of CS suggests a steep density gradient in the core.

## 2) HCN

Kutner and Tucker (1975) mapped HCN  $J=1 \rightarrow 0$  (88.6 GHz) emission and found that it peaks on the infrared cluster. The HCN  $J=1 \rightarrow 0$  map with a  $15''$  beam of Richardson et al. (1988) indicates that the two peaks located northeast and southwest are separated by  $2'$  (0.5 pc). We discuss our new HCN  $J=4 \rightarrow 3$  emission maps in Chapter VI.

## 3) H<sub>2</sub>CO

Loren et al. (1974) were the first to detect the H<sub>2</sub>CO  $J_{K_1, K_2} = 2_{1,1} \rightarrow 1_{1,1}$  transition (140 GHz) at the core of Mon R2. They found that the half-intensity radius of formaldehyde is  $3'.3$  (0.8 pc). The spectrum of the  $J_{K_1, K_2} = 1_{1,1} \rightarrow 1_{1,0}$  (4830 MHz or 6 cm) transition of H<sub>2</sub>CO obtained by Downes et al. (1975) has two absorption-line features at velocities of 8.0 and 11.1 km/s. It should be noted that at approximately the same velocities we see absorption features in our CO maps (at 7.6 km/s and 11.3 km/s). This is an indication that at least some of the molecular cloud is in front of the H II region. There is no other

recent study of the Mon R2 core in  $\text{H}_2\text{CO}$ . We present new  $\text{H}_2\text{CO}$  observations at sub-millimeter wavelengths in Chapter VI.

#### 4) $\text{NH}_3$

Macdonald et al. (1981) observed  $\text{NH}_3$  (1,1) and (2,2) emission (at 23.69 GHz and 23.72 GHz) in this region (2.2' beam width). Observations by Willson and Folch-Pi (1981) and Torrelles et al. (1983) with an angular resolution of 1'.5 and 1'.4, respectively, show that the  $\text{NH}_3$  emission is contained within an ellipsoidal region about 8'  $\times$  5' in extent. This structure is centered south of the compact objects. These studies, however, have low resolution and, therefore, do not give detailed information about the cloud core.

Studies by Montalban et al. (1990) of the ammonia emission distribution (beam width of 42") show evidence for clumps with diameters of a few  $\times$  0.1 pc and masses between 1 and 65  $M_\odot$ . Torrelles et al. (1990) made high-resolution observations (3") of  $\text{NH}_3$  (1,1) and  $\text{NH}_3$  (2,2) emission with the VLA, and these show several small condensations that constitute an arc-like structure located 40" to the southwest of the H II region. The reason for the displacement of the ammonia structure from the edge of the H II region is not yet understood. Within the arc, there is a clear temperature gradient, with the highest temperatures toward the northeast inner edge of the arc-like structure. This implies, according to Torrelles et al., interaction of the exciting source(s) of the H II region and/or the stellar wind with the ambient dense molecular gas.

Both  $\text{NH}_3$  studies suggest that the kinetic temperature in the cloud core is typically between 20 K to 30 K, increasing to over 45 K toward the position of the embedded infrared sources. Montalban et al. suggest that the high temperature is caused from heating due to the photoelectric effect on dust grains. The ultraviolet radiation that is responsible for the heating of the gas originates from the B0 star which is exciting the compact H II region. This will be discussed in the next subsection (iv). Montalban et al. note, however, that the ultraviolet radiation causing the heating should also dissociate the  $\text{NH}_3$  molecules. In order to explain that  $\text{NH}_3$  is only partially photodissociated at the cloud edge, Montalban et al. propose that gas phase ammonia is being evaporated from dust grain mantles according to the Gusten and Fiebig (1988) model.

#### 5) $\text{HCO}^+$

From observations of  $\text{HCO}^+$  emission by Loren (1977) and Richardson et al. (1988) two peaks were identified that were separated by 2' (as is the case for the map of HCN emission). However, since these surveys were done at low resolution, we will not dwell on their results.

Gonatas et al. (1992) used single-dish measurements with the FCRAO (Five College Radio Observatory) 14 m antenna with a 58" beam width to observe the core of Mon R2 in  $\text{HCO}^+$  ( $J=1 \rightarrow 0$ ).  $\text{HCO}^+$  emission was detectable over a 4' x 4' region with two main condensations: one in the NE and one in the SW. Gonatas et al. also observed  $\text{HCO}^+$  ( $J=1 \rightarrow 0$ ) emission with a beam width of 9".8 using the Hat Creek interferometer. Their study suggests the presence of two regions of high intensity which almost engulf an area of low

intensity. This high resolution map has similar overall morphology with the single-dish map, although it reveals a very clumpy structure. It is not clear how much of the clumpiness is real. All the clumps detected by Gonatas et al. have about the same shape and size, which coincides with the beam size.

Characteristics of the Mon R2 cloud core can be deduced from previous molecular line work. The core has a large density gradient and the density reaches values as high as  $10^6 \text{ cm}^{-3}$ . All molecules (with the exception of ammonia) show a similar structure: two emission peaks in the northeast and the southwest surround an almost circular region that has minimum intensity. The shape of the core is roughly circular. Furthermore, it is clear that the gas is clumpy, but at what scale is uncertain. These issues will be addressed in the light of our observations.

#### *iv) H II region*

Prior to the CO observations of Loren et al. (1974), 13 radio sources had been observed inside the cloud boundary during surveys at 1.4 GHz conducted by Shimmins et al. (1966) and by Ehrman et al. (1970). One radio-continuum thermal source was seen: G213.7-12.6 [PKS 0605-06 in the survey by Shimmins et al. or OH-009 in the survey by Ehrman et al.]. The source is identified with an H II region and is located in the core of the cloud.

When the Mon R2 region was studied by Downes et al. (1975) at 10.7 GHz (about 3 cm) with a beam width of 77", it became apparent that the H II region has inner structure. It consists of two components: an extended

envelope of low density ( $1.9 \times 10^2 \text{ cm}^{-3}$ ) with a diameter of about  $3'$ , and a strong compact source with a diameter of about  $22''$  and an electron density of  $9.6 \times 10^3 \text{ cm}^{-3}$ . This structure suggests that the H II region is expanding in two environments with different densities, the less dense matter being the interstellar medium surrounding the cloud. Gilmore (1980) proposes that this is a "blister" type H II region, as described by Israel (1978). In the blister model, the exciting star of the H II region is located near the edge of the neutral cloud. The star causes an ionization front to move through the cloud. When the ionization front crosses the molecular cloud boundary, the ionized gas expands into the intercloud medium creating a diffuse component. Thus, the H II region can consist of one or more small and bright peaks, surrounded by a larger, less intense envelope. Additional evidence that has been used to argue that the H II region is closer to the rear side of the cloud is that the OH and H<sub>2</sub>CO lines at 6 cm are seen in absorption against the radio continuum source (Downes et al. 1975; Loren 1977).

Gilmore suggests that the two components of the H II region are probably excited by the same star. The total infrared luminosity (for  $1.65 \mu\text{m} < \lambda < 250 \mu\text{m}$ ) of the compact portion of the H II region, as determined by Thronson et al. (1980), is approximately  $4 \times 10^4 L_{\odot}$ . If the far-infrared luminosity is used in conjunction with Rubin's method (1978), the required Lyman continuum photon luminosity is  $5.6 \times 10^{47} \text{ s}^{-1}$ . Following Panagia (1973), Hackwell et al. (1982) find that the ZAMS spectral type must be between O9.5 and B0.

A very important study of the H II region is that of Massi et al. (1985); their VLA observations at 1.3 cm and 6 cm have up to 1" resolution. Their observations indicate that the compact component is almost circular with a 27" diameter and its maximum flux density occurs near its southeast edge. Maps at 1.65  $\mu\text{m}$ , 2.2  $\mu\text{m}$ , 10  $\mu\text{m}$  and 20  $\mu\text{m}$  by Beckwith et al. (1976) were used by Massi et al. to determine the exciting source of the H II region. These authors measured the 1.65  $\mu\text{m}$  flux in their 10" beam width at the position of IRS 1 to be 0.04 Jy (1 Jansky =  $10^{-26}$  W m<sup>-2</sup> Hz<sup>-1</sup>). What is the source of this 1.65  $\mu\text{m}$  flux? Is it due to the ionized gas or to the star that excites the H II region? Massi et al. interpolate from their 1.3 cm data that the contribution of the free-free and bound-free emission from the ionized gas would be, if reddening is not considered, 0.87 Jy at 1.65  $\mu\text{m}$ . To compute the contribution of the gas to the observed flux they consider the extinction towards the source. Assuming the minimum extinction observed,  $A_V \cong 23$  magnitudes (Simon et al. 1983), Massi et al. find that the contribution from the ionized gas is at most 0.006 Jy at 1.65  $\mu\text{m}$  (15% of the total flux from the position of IRS 1 at 1.65  $\mu\text{m}$ ). The fraction can be smaller if the extinction is 33 magnitudes as Natta et al. (1986) find. Massi et al. conclude that the 1.65  $\mu\text{m}$  emission from IRS 1 is from the star that ionizes the H II region.

Another interesting feature is that IRS 1 seen at 1.65  $\mu\text{m}$  is displaced 7" from the peak of the radio emission. The centimeter wavelength emission is due to free-free emission and is stronger at higher gas densities. Thus, the reason for the displacement of the radio emission peak from the position of the ionizing star may be that the gas close to the star must be at a lower density than that at the southeast edge of the H II region.

The fact that the radio emission ridge or arc is only a fraction of the circumference suggests an offset of the ionizing star with respect to the centre of the shell, noted by Massi et al. They point out that the ionizing star (IRS 1 in the 1.65  $\mu\text{m}$  image) is not at the centre of the H II region, but is offset 2" toward the radio peak. Massi et al. managed to successfully model the morphology of the H II region as a 2"-thick shell photoionized by a star which is offset by 6.5" from the radio peak. Figure 3 indicates the reproduction of the H II region from their model, which is in excellent agreement with the observations. Massi et al. discuss the physical processes that can give rise to the implied geometry. First, the shell must be broken on its northwestern part in order to explain the diffuse component. The high-velocity gas that rushes from this rupture ensures the presence of a region depleted in gas around the ionizing star and, hence, a shell-like morphology occurs (Bedjin and Tenorio-Tagle 1981).

The structure of the H II region implies a rather advanced stage of evolution of the blister. According to Bodenheimer et al. (1979), if the star was at an initial distance of 90% of the Strömgen radius from the cloud edge, the maximum speed of the outflowing gas would be 30 km/s. Thus, we estimate that the diffuse H II region of Mon R2 must be at least  $1.2 \times 10^4$  years old to have attained its present 3' angular size.

Very high-resolution (0".4) VLA observations of the compact component of the H II region of Mon R2 were carried out by Wood and Churchwell (1989) at 2 cm and 6 cm. The value of 24" as a mean diameter of the compact H II region was adopted. There is excellent agreement between these data and the observations of Massi et al. According to Wood and

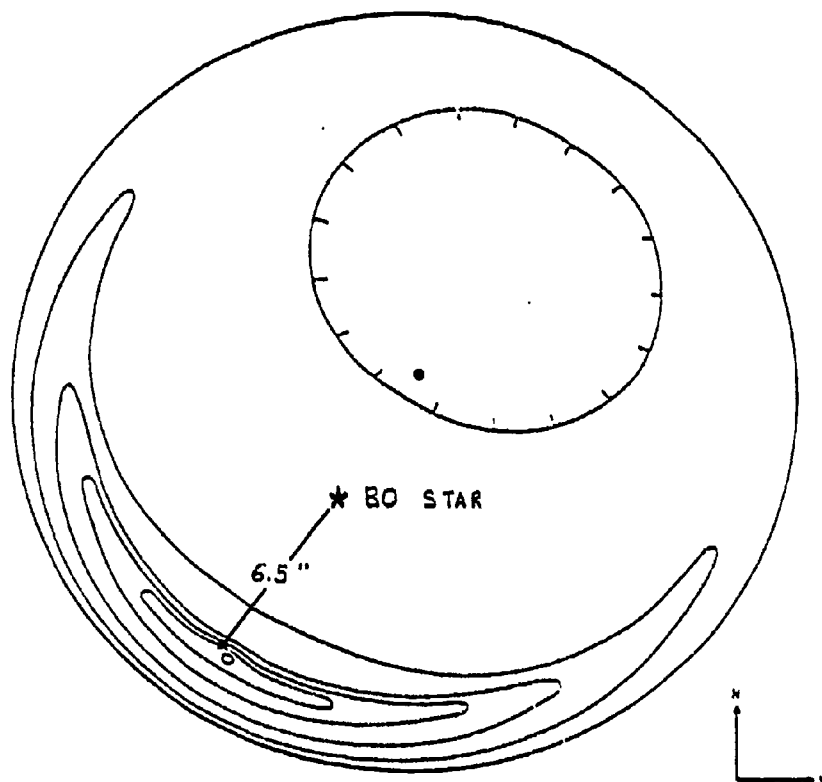


**Fig. 3** The surface brightness distribution of the HII region according to Massi et al.'s model. These authors propose that this distribution is due to the photoionization of a shell by a star (indicated by the star) which is offset from the centre of the shell. The centre of the shell is at the dot and the displacement of the star from the radio peak is 6.5" (adapted from Massi et al. 1985).

Churchwell, the morphology of Mon R2 is cometary, i.e. the ionization front is parabolic and the surface brightness along the parabola's axis of symmetry decreases gradually from the 'head' to the 'tail'. The presence of masers and the nearly parabolic shape of the ionization front suggest that the H II region may have been produced by the bow shock of an O or B star moving supersonically through the molecular cloud (Hughes and Viner 1976). The speed of sound in a typical molecular cloud is 0.2 km/s. Therefore, the space velocity is supersonic, since the velocity dispersion of OB associations is typically 2 km/s. Although this model seems to successfully explain other cometary ultra-compact H II regions, it does not seem necessary in the case of Mon R2. The blister model has been examined thoroughly and works well. The cometary or bow shock model has not been applied in detail to the Mon R2 compact H II region.

#### *v) Infrared cluster*

The Mon R2 star forming region has been mapped at a number of infrared wavelengths from 1.65 to 100  $\mu\text{m}$  (Aspin and Walther 1990; Beckwith et al. 1976; Hackwell et al. 1982; Thronson et al. 1980). Beckwith et al. first discovered five compact near-infrared sources, which are located near the centre of the dense molecular cloud core and are optically obscured. Aspin and Walther (1990) found additional infrared sources in a higher resolution (1".2) 2.2  $\mu\text{m}$  image of the cluster. We will discuss separately some of the characteristics of the more important infrared sources.

### 1) IRS 1

It has been noted that the ionizing star of the H II region is of spectral type around B0; the expected unreddened  $1.65 \mu\text{m}$  flux from this type of star is  $1.2 \text{ Jy}$ , according to Massi et al. This flux is 30 times greater than the average radiation from the gas in the H II region in a  $10''$  beam measured by Beckwith et al.; hence the exciting star should be seen in the  $1.65 \mu\text{m}$  map. This excludes the only other likely candidate, IRS 2, as the exciting star of the H II region, because it does not appear at  $1.65 \mu\text{m}$  (Figure 4). The locations of IRS 3, 6 and 7 make them implausible candidates for the exciting star. The only strong  $1.65 \mu\text{m}$  source within the H II region is IRS 1. Therefore, IRS 1 in the  $1.65 \mu\text{m}$  map is the likely ionizing star of the H II region.

Images of the infrared cluster at  $10$  and  $20 \mu\text{m}$  by Hackwell et al. (1982) are consistent with the images by Beckwith et al. (Figure 4). Both of these studies indicate that the appearance of IRS 1 changes significantly with wavelength. From the previous discussion of Massi et al., IRS 1 at  $1.65 \mu\text{m}$  is directly associated with the B0 star that excites the H II region. At intermediate wavelengths ( $2 \mu\text{m} < \lambda < 10 \mu\text{m}$ ) IRS 1 is a point source, which indicates that it is probably an embedded star seen by the scattering of the surrounding dust or reddened by the foreground dust. At longer wavelengths IRS 1 becomes an extended source, probably due to the emission from dust enclosed in and surrounding the H II region.

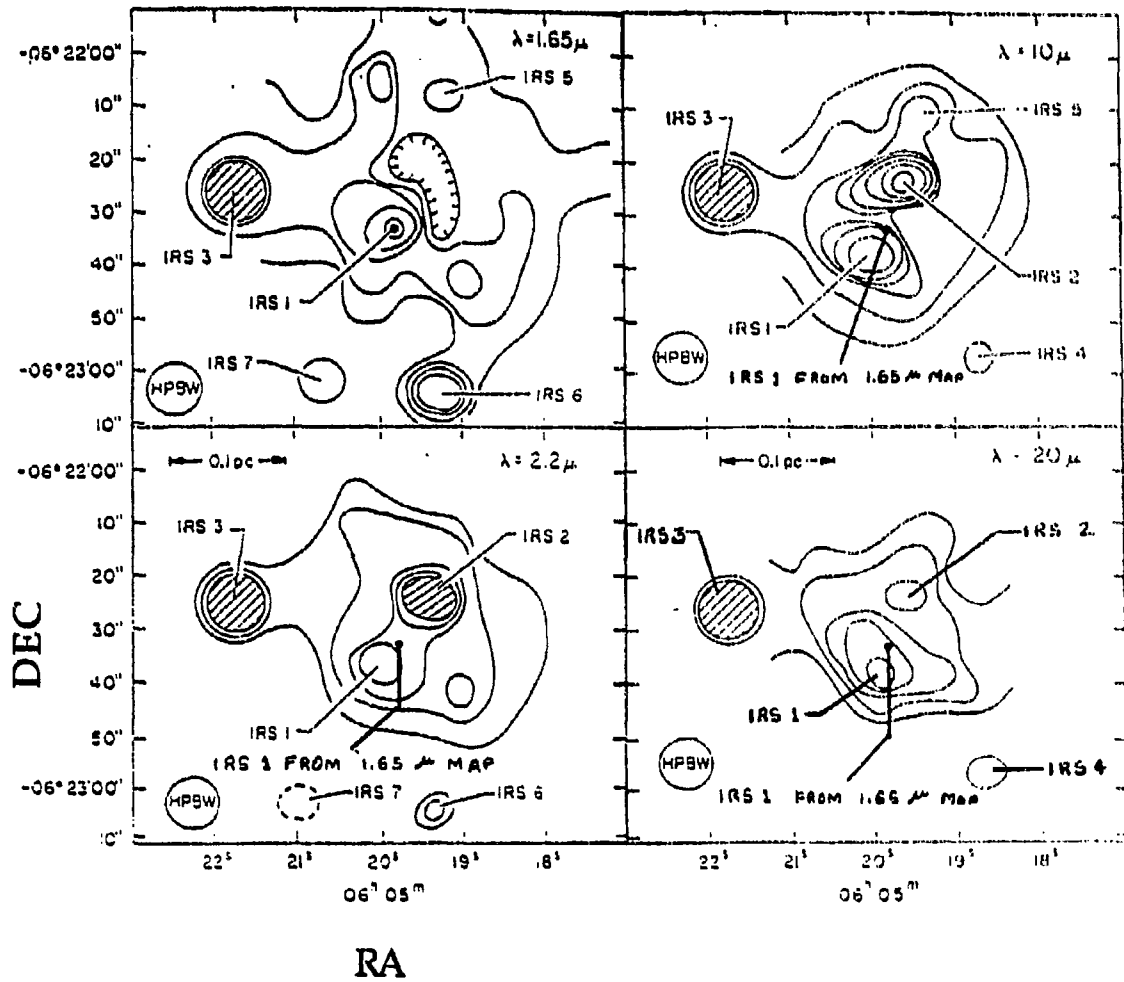


**Fig. 4** Infrared maps at  $1.65 \mu$ ,  $2.2 \mu$ ,  $10 \mu$ ,  $20 \mu$  of the cluster of embedded sources. The beam is  $10''$ . Note that the flagged contour on the  $1.65 \mu$  around the position of IRS 2 represents an area of minimum flux, in contrast with the  $2.2 \mu$  map where IRS 2 is prominent (adapted from Beckwith et al. 1976)

## 2) IRS 2

The most striking feature of the polarization map at  $2.2 \mu\text{m}$  by Aspin and Walther (Figure 5) is the ring-like structure surrounding IRS 2. The flux from this structure is strongly polarized, with the polarization vectors oriented perpendicular to the direction toward IRS 2. Hodapp (1987) suggests that IRS 2 is the illuminating source of the shell.

Figure 6 indicates that IRS 2 and IRS 3 have  $1.65 \mu\text{m} - 20 \mu\text{m}$  energy distributions typical of young or pre-main-sequence objects. This conclusion is based on the characteristics of their continuum spectra: the intensity rises sharply for  $\lambda < 8 \mu\text{m}$ , turns over at around  $9 \mu\text{m}$  and remains constant between  $10 \mu\text{m}$  and  $20 \mu\text{m}$ . This behaviour is predicted by models of young objects (Bedijn et al. 1978). The central object in each case is believed to be a massive main-sequence star still surrounded by a large amount of infalling dust and gas. The visual and UV radiation of each central star is completely absorbed by this opaque dust shell and is remitted at infrared wavelengths.

## 3) IRS 3

IRS 3 is a high-mass protostellar system which is one of the brightest thermal infrared sources in the Galaxy. From Figure 5 it is evident that IRS 3 is associated with its own nebulosity and does not affect the polarization pattern seen in the shell around IRS 2. This led Hodapp (1987) to argue that IRS 3 is not physically near the shell but some distance away along the line-of-sight. It seems likely that IRS 3 is a separate site of star formation (the shell associated with IRS 2 being the first). Additional evidence for active star formation in IRS 3 is its association with an  $\text{H}_2\text{O}$  maser (Downes et al. 1975).

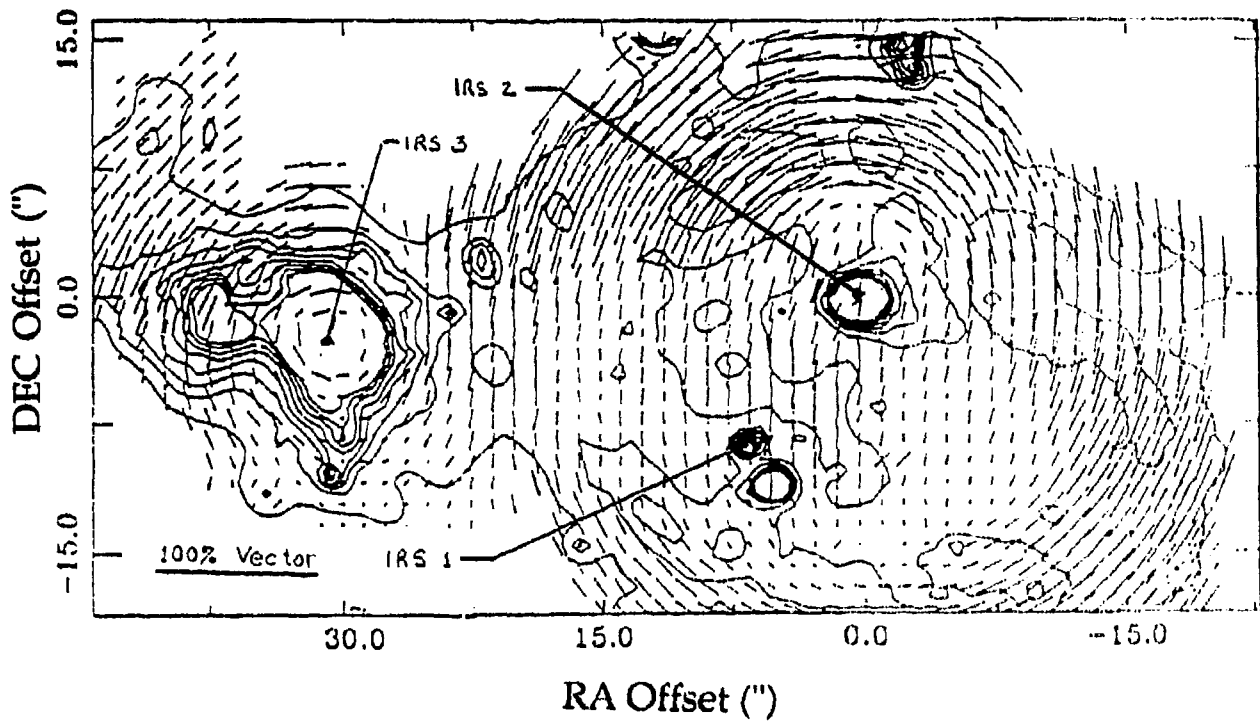


**Fig. 5**  $2.2 \mu\text{m}$  contour map and polarization vector map of the infrared cluster (adapted from Aspin and Walther, 1990 b). The map is centered on IRS 2 ( $0'', 0''$ ) and the offsets are given in arcseconds. IRS 1 is at ( $6'', -8''$ ) and IRS 3 is at ( $-30'', -3''$ ).

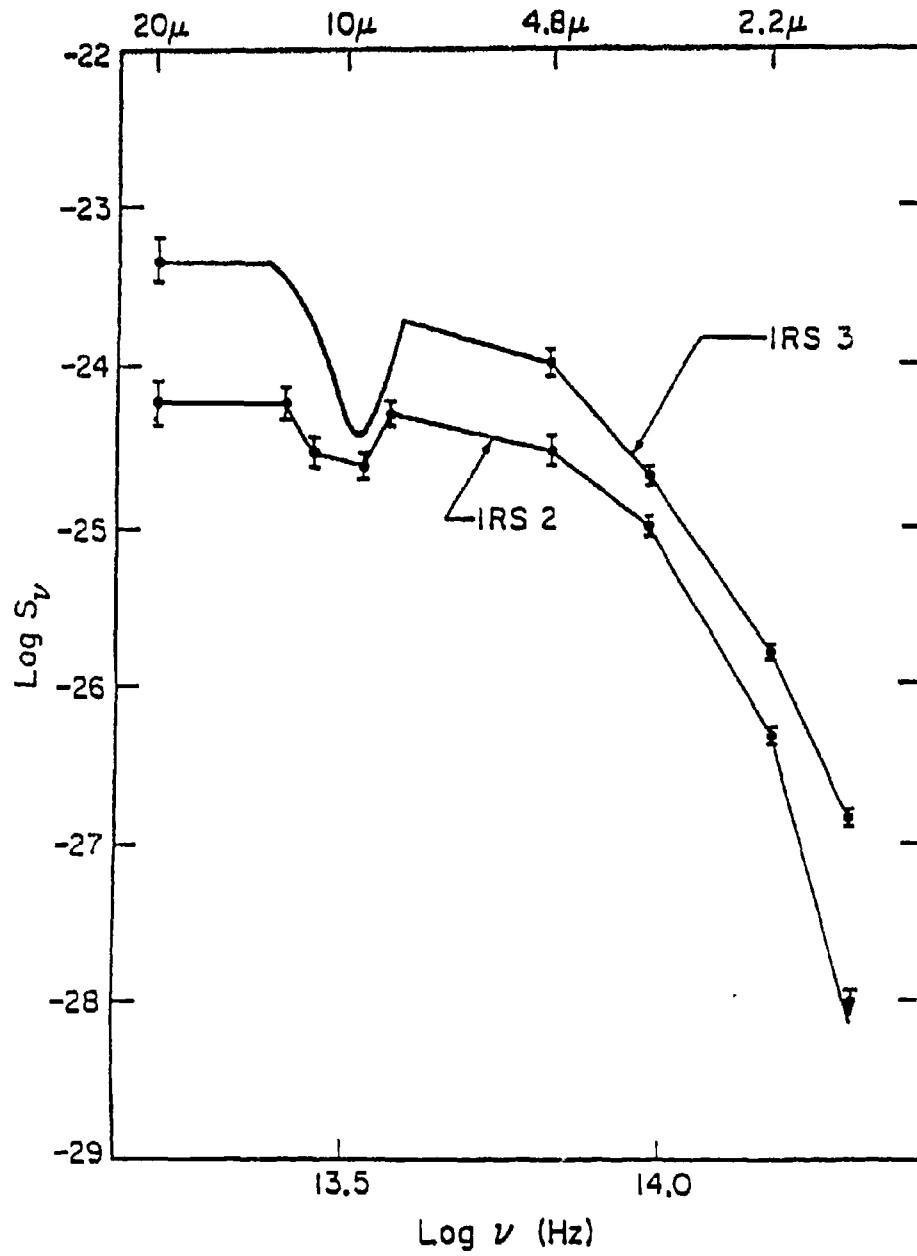


**Fig. 6** 1.65  $\mu$ m to 20  $\mu$ m energy distributions of IRS 2 and IRS 3 (adapted from Beckwith et al. 1977).

Our CO observations show that in the vicinity of IRS 3 there is high-velocity gas, a good indication that this infrared source could be the source of the large CO outflow.

#### 4) *Other infrared sources*

The 2.2  $\mu\text{m}$  images of Aspin and Walther (1990) show not only the seven sources that Beckwith et al. (1976) identified, but also ten additional point-like sources in the field. These are labeled as IRS 1a, aj, ajj, and b through h. The images indicate that IRS 1, IRS 2, IRS 3 and IRS 5 are all associated with nebulosity, while IRS 4, IRS 6 and IRS 7 are isolated from the shell-H II region and may be either embedded sources, background sources or foreground objects. Additional photometry is needed to clarify this.

IRS 5 is in the northern part of the shell and is apparently an extended knot rather than a point source. It is peculiar that IRS 5 geometrically does not form part of the shell but is offset from the general elliptical structure by about 5". If, as proposed by Hodapp, the shell structure is defined by the density of the ambient molecular cloud into which it is expanding, it is possible that the density is low in this region and the H II region has expanded further in this direction than in others. IRS 5 may therefore be located at the interface between the H II region and molecular cloud. Further evidence for this will be given when we discuss our millimeter continuum data (Chapter VI).

We present our new observations in Chapter II, the morphology of our CO emission maps in Chapter III, a brief summary of the derivations of

various physical quantities in Chapter IV, the calculations of important quantities such as temperature and column density in Chapter V, a discussion of our results and their implications in Chapter VI, and, finally, our conclusions in Chapter VII.

## II. OBSERVATIONS

### a. Data

All line emission spectra from a  $3' \times 3'$  area in the Mon R2 core region were obtained with the 15 m James Clerk Maxwell Telescope (JCMT) on Mauna Kea, Hawaii. Observations of  $^{12}\text{CO}$   $J=3 \rightarrow 2$  (345 GHz) and  $^{13}\text{CO}$   $J=3 \rightarrow 2$  (330 GHz) emission lines were carried out by G. F. Mitchell and H.E. Matthews in December 1991 and March 1992. The  $^{12}\text{CO}$   $J=2 \rightarrow 1$  (230 GHz) spectra were obtained by L. Avery during Canadian Service Observing Time in April 1992. The observed intensity for the three transitions is in the form of antenna temperature  $T_A^*$ , which is the antenna temperature corrected for atmospheric and telescope losses (Mitchell 1992).

$^{12}\text{CO}$   $J=3 \rightarrow 2$  observations consist of a 290-positions map ( $19 \times 16$ ) with a  $10''$  grid pattern separation (Figure 7). For the  $J=3 \rightarrow 2$  transition of both  $^{12}\text{CO}$  and  $^{13}\text{CO}$ , the "common-user" receiver B3i was used. This is a single-channel receiver based on a lead-alloy SIS detector, and covers a range of frequencies between 300 GHz and 380 GHz. The half-power beam width (HPBW) is  $15''$  (0.06 pc at the distance of Mon R2) and the beam efficiency is 0.50, according to "The JCMT: A Guide for the Prospective User" by H.E. Matthews (1992). The integration time for the  $^{12}\text{CO}$  spectra was 120 seconds and for  $^{13}\text{CO}$  spectra was 300 seconds. All observations were done in a position switching mode in which the telescope is alternatively switched between the source and a nearby reference position with no emission.

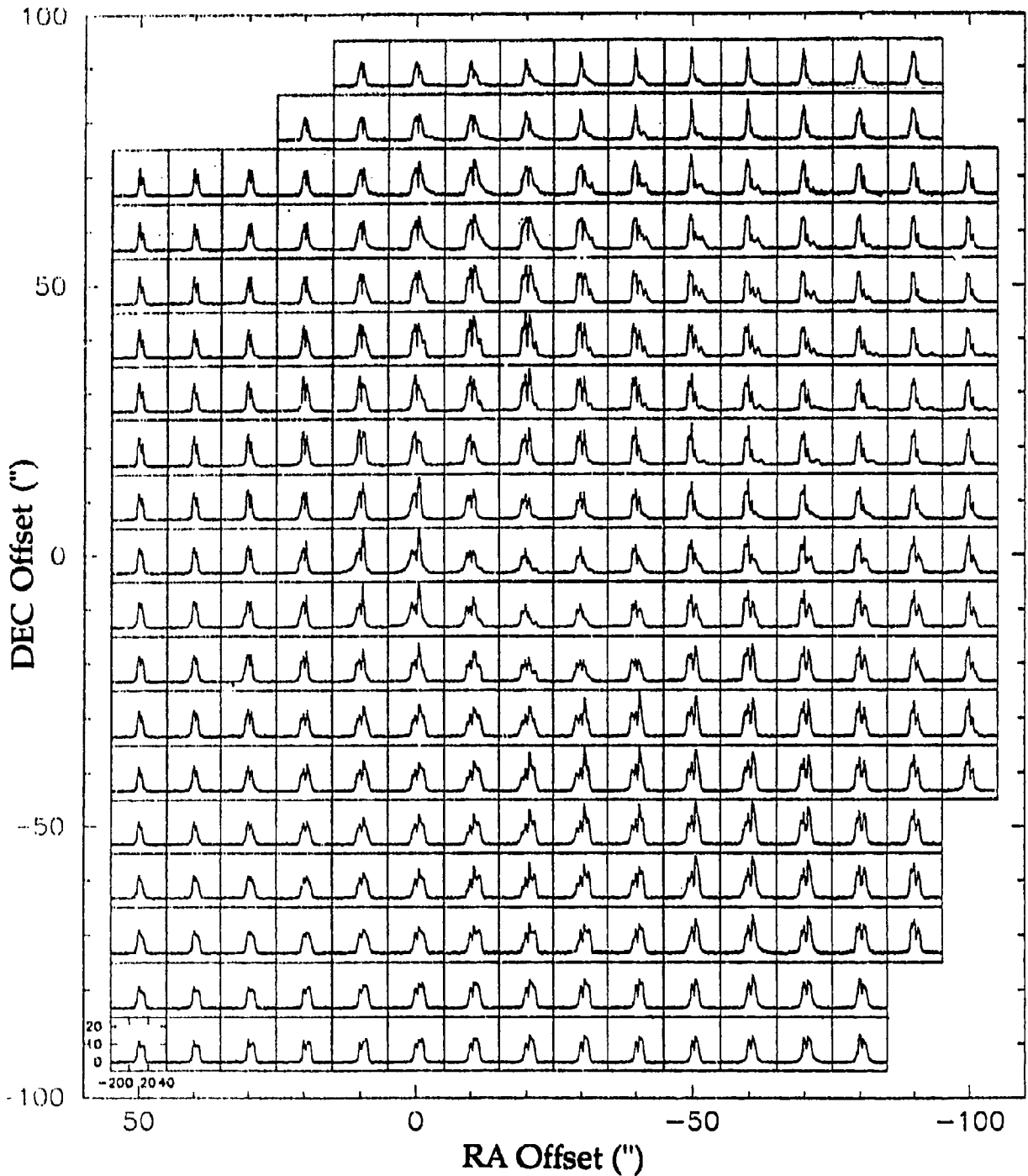


**Fig. 7** A 19 x 16 map of 290  $^{12}\text{CO}$   $J=3\rightarrow 2$  spectra on a 10" grid. All spectra plot a measure of the observed intensity versus LSR velocity. The observed intensity is in the form of antenna temperature corrected for atmospheric and telescope losses,  $T_A^*$ . The positions are given as R.A. and DEC offsets ( $\Delta\alpha$ ,  $\Delta\delta$ ) expressed in arcseconds from Mon R2 IRS 3 [ $\alpha(1950) = 06^{\text{h}}05^{\text{m}}21.^{\text{s}}50$ ,  $\delta(1950) = -06^{\circ}22'26''$ ]. East and North are positive.

$^{12}\text{CO}$   $J=2\rightarrow 1$  and  $^{13}\text{CO}$   $J=3\rightarrow 2$  spectra were observed at 12 positions in the core of the Mon R2 region. These positions were chosen because they coincided with peaks of the antenna temperature in the  $\text{CO}$   $J=3\rightarrow 2$  map. Table I contains a list of all observed positions. In Table I and subsequently, positions are given as offsets in R.A. and DEC ( $\Delta\alpha$ ,  $\Delta\delta$ ) in arcseconds from Mon R2 IRS 3 [ $\alpha(1950) = 06^{\text{h}}05^{\text{m}}21^{\text{s}}.50$ ,  $\delta(1950) = -06^{\circ}22'26''$ ]. East and North are positive. The  $^{12}\text{CO}$   $J=3\rightarrow 2$  and  $^{13}\text{CO}$   $J=3\rightarrow 2$  spectra are presented at common scales in Figure 8 (i and ii); the  $^{12}\text{CO}$  spectra are shifted by 5 K with respect to the  $^{13}\text{CO}$  spectra. The data reduction was carried out by G. F. Mitchell and the author using the SPECX package (Padman 1988).

For the  $^{12}\text{CO}$   $J=2\rightarrow 1$  transition at 230 GHz, the "common-user" receiver A2 was used. Receiver A2 is a single-channel device built around a lead-alloy SIS mixer; the receiver is used for a range of frequencies between 210 GHz and 280 GHz. The half-power beam width (HPBW) and the beam efficiency at 230 GHz are 21" and 0.63, respectively (Matthews 1992). The spectra of  $^{12}\text{CO}$   $J=2\rightarrow 1$  emission are shown in Figure 9 (i and ii).

Observations of two other molecules complement the CO data. Both HCN  $J=4\rightarrow 3$  (354.5 GHz) and  $\text{H}_2\text{CO}$   $J_{K_1, K_2} = 5_{1,5} \rightarrow 4_{1,4}$  (351.7 GHz) maps were obtained by G. F. Mitchell and H. E. Matthews in November of 1992 with a 15" beam. During the same period, they observed the Mon R2 core in the sub-millimeter and millimeter continuum at four wavelengths—450  $\mu\text{m}$ , 800  $\mu\text{m}$ , 1100  $\mu\text{m}$  and 1300  $\mu\text{m}$ —with the UKT14 bolometer system of the JCMT. The sub-millimeter and millimeter continuum data will be discussed in Chapter VI.

**TABLE I**  
**COORDINATES OF THE TWELVE OBSERVED POSITIONS**  
**IN THE  $^{12}\text{CO}$  J=2 $\rightarrow$ 1 and  $^{13}\text{CO}$  J=3 $\rightarrow$ 2 TRANSITIONS**

Position number	Offset ( $\Delta\alpha, \Delta\delta$ ) from IRS 3 $\alpha(1950) = 06^{\text{h}}05^{\text{m}}21^{\text{s}}.5,$ $\delta(1950) = -06^{\circ}22'26''$
1	10", 20"
2	0", 0"
3	-10", -20"
4	-10", 60"
5	-20", -70"
6	-20", -10"
7	-20", 40"
8	-40", -40"
9	-40", 60"
10	-50", -60"
11	-60", -10"
12	-80", 30"

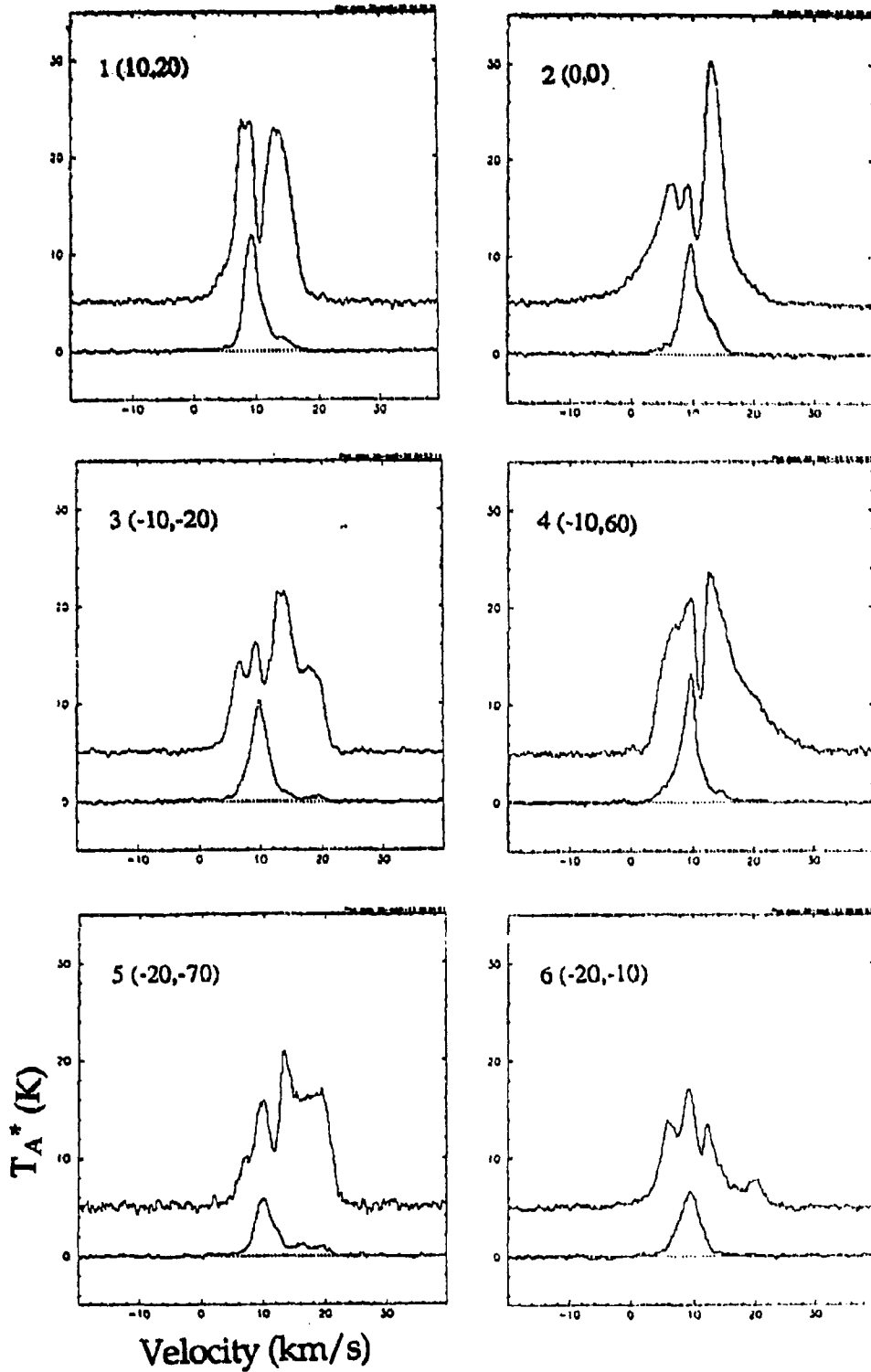


**Fig. 8 i** First six pairs of  $^{12}\text{CO}$   $J=3 \rightarrow 2$  (345 GHz) and  $^{13}\text{CO}$   $J=3 \rightarrow 2$  (330 GHz) spectra are presented to the same scale, with the  $^{12}\text{CO}$  spectra shifted by 5 K with respect to the  $^{13}\text{CO}$  spectra. The half power beam width is  $15''$  and the integration times are respectively 120 sec and 300 sec. In the upper left corner their position number and coordinates are given.

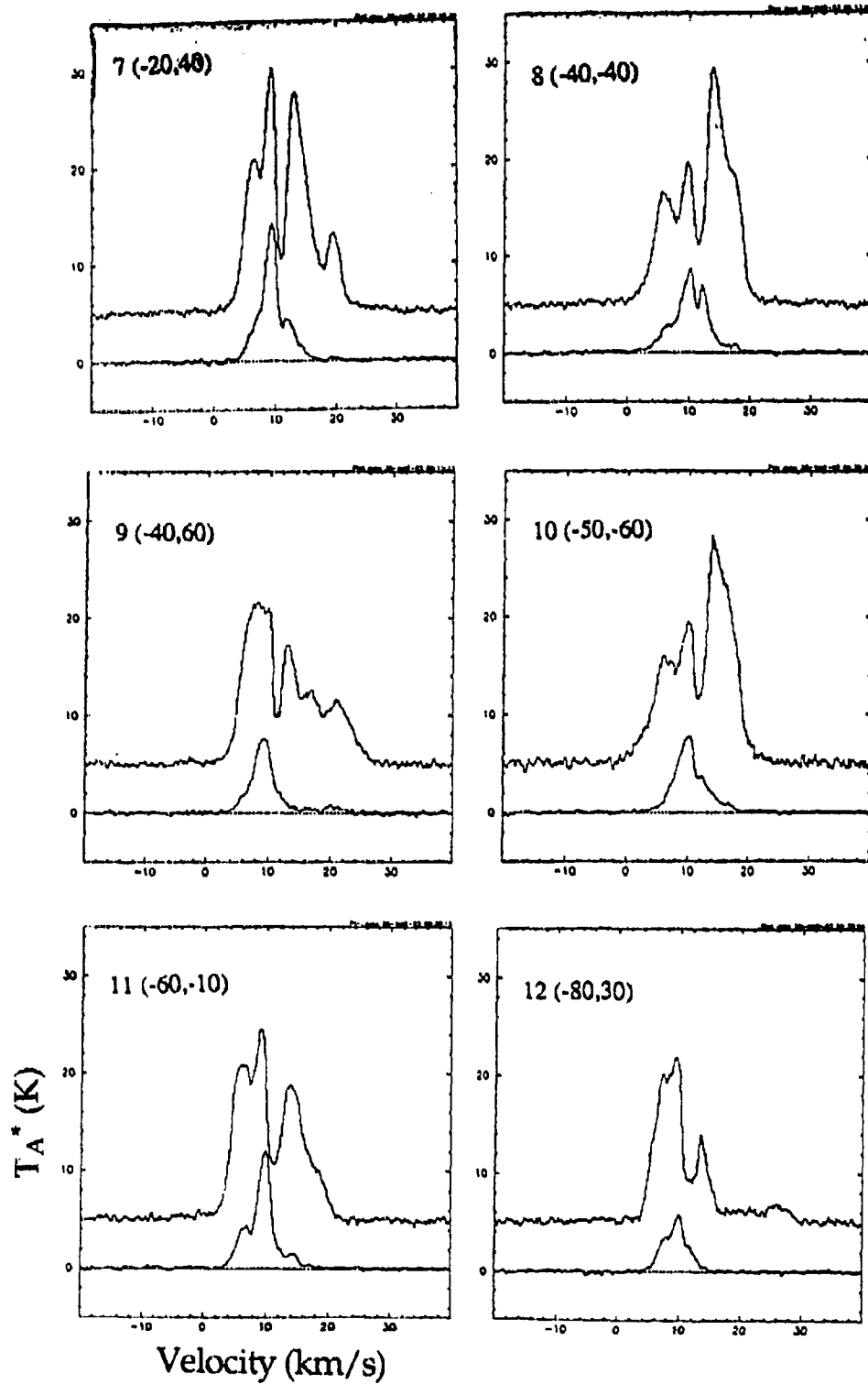


**Fig. 8 ii** Last six pairs of  $^{12}\text{CO}$   $J=3\rightarrow 2$  (345 GHz) and  $^{13}\text{CO}$   $J=3\rightarrow 2$  (330 GHz) spectra are presented to the same scale, with the  $^{12}\text{CO}$  spectra shifted by 5 K with respect to the  $^{13}\text{CO}$  spectra. The half power beam width is  $15''$  and the integration times are respectively 120 sec and 300 sec. In the upper left corner their position number and coordinates are given.

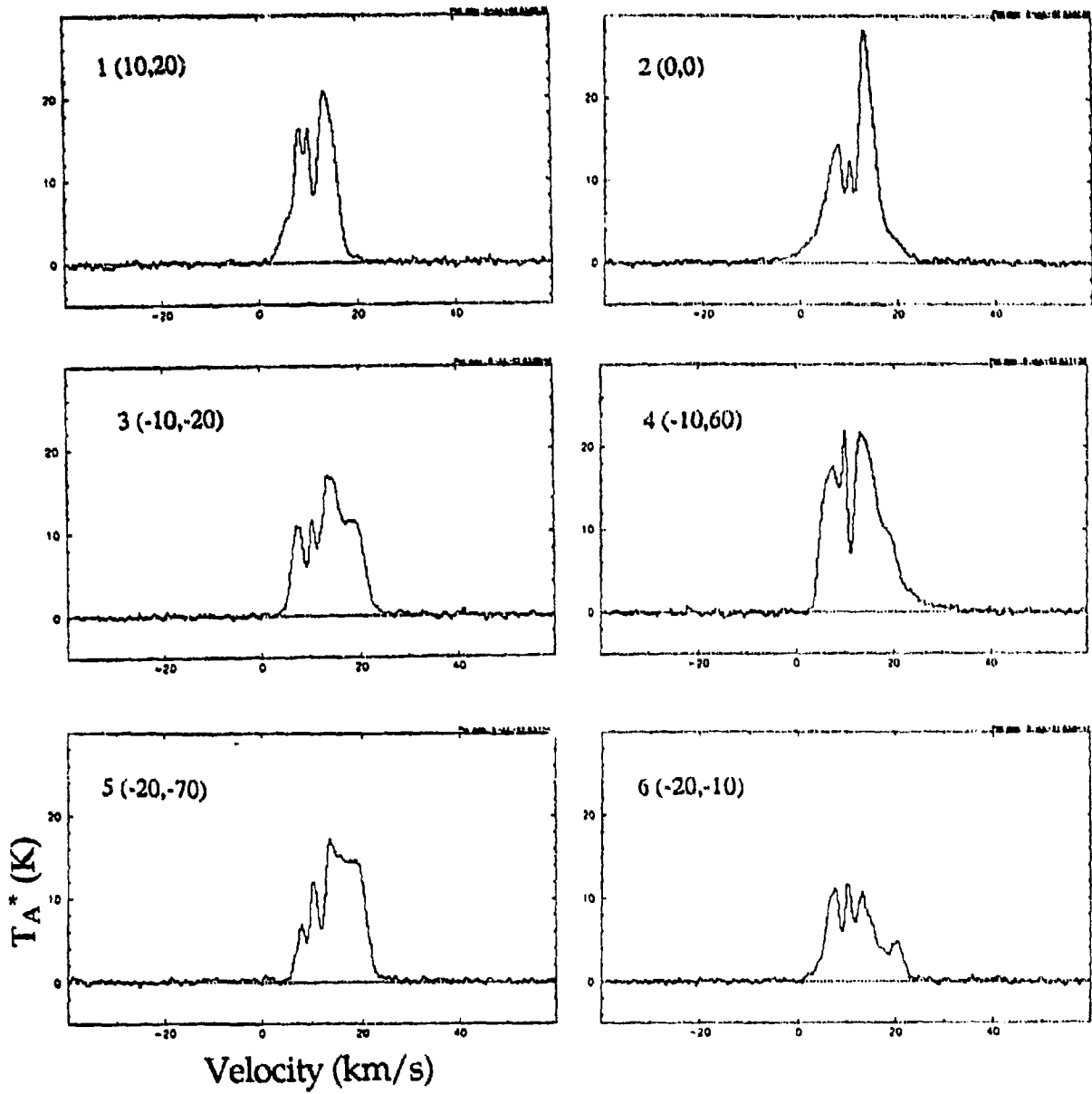


**Fig. 9 i** The  $^{12}\text{CO}$   $J=2 \rightarrow 1$  (230 GHz) spectra at positions 1 to 6; the number and coordinates of each position are given in the upper left corner. The half-power beam width is  $21''$ . The integration time is 120 sec.

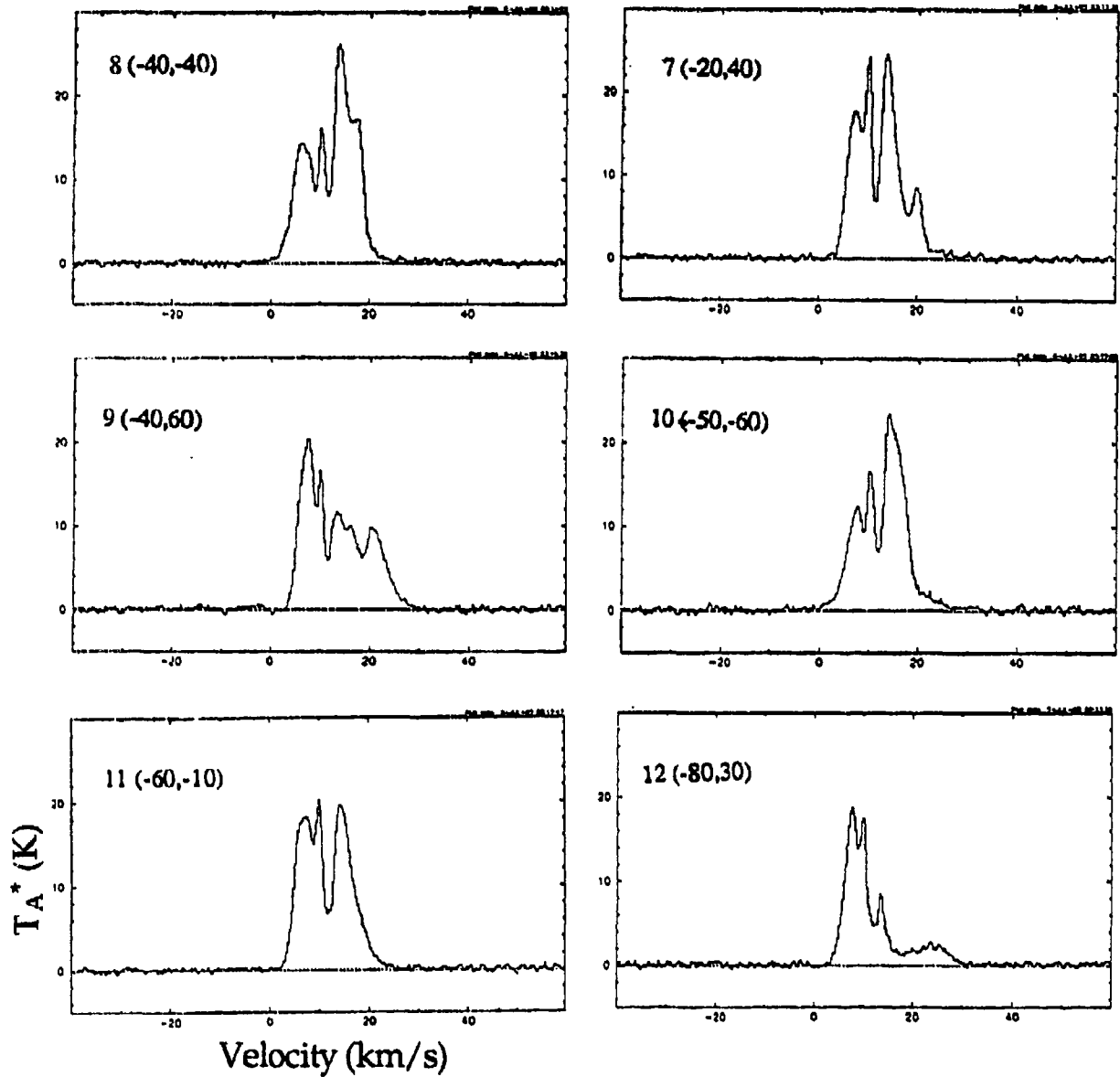


**Fig. 9 ii** The  $^{12}\text{CO}$   $J=2 \rightarrow 1$  (230 GHz) spectra at positions 7 to 12; the number and coordinates of each position are given in the upper left corner. The half-power beam width is  $21''$ . The integration time is 120 sec.

This thesis also makes use of a new high resolution (6.9 km/s) infrared absorption spectrum in the M-band (4.7  $\mu\text{m}$ ), obtained by G. F. Mitchell and J.-P. Maillard (1993) using the Fourier Transform Spectrometer on the Canada France Hawaii Telescope (CFHT) on Mauna Kea, Hawaii. Data reduction for the infrared absorption spectroscopy was done by G.F. Mitchell, and is briefly outlined in Chapter VI.

### b. Comments on the CO line shapes

From **Figures 8 and 9** it is clear that the CO emission lines are very complex. A general observation is that the spectral lines are asymmetric with respect to the velocity of the line centre at 10.3 km/s. The approaching gas (blue-shifted) seems to be more tightly constrained in velocity relative to the line centre than the receding gas, which exhibits a slower and irregular decrease in strength with increasing velocity. This is a simplified picture since the lines are very complicated when examined in detail.

Six features recur in most of the spectra of the  $^{12}\text{CO}$   $J=3\rightarrow 2$  map: maxima near 6.7 km/s, 9.3 km/s and 13.0 km/s and minima near 7.6 km/s, 11.3 km/s and 16.4 km/s. Three of these appear in all spectra: the maxima at 9.3 km/s and 13.0 km/s, and the minimum at 11.3 km/s. There is a positive velocity shift at which a dip in the  $^{12}\text{CO}$  emission occurs (11.3 km/s) relative to the velocity of the  $^{13}\text{CO}$  emission peak (10.3 km/s). This shift implies that the self-absorbing layer is moving away from the observer towards the cloud

core. The simplest interpretation is that some part of the cloud is still contracting. A second fairly common absorption feature is seen at approximately 7.6 km/s. Since its velocity differs by almost 3 km/s from the cloud's velocity, this absorption feature is likely to arise in a foreground cloud. Finally, the dip seen at 16.4 km/s is not an absorption feature but is a true emission minimum. Emission seen beyond 16.4 km/s represents high-velocity gas with respect to the quiescent gas.

### III. MORPHOLOGY OF THE GAS

It will become clear that a great wealth of information on the core of Mon R2 can be extracted from the emission lines of the carbon monoxide transitions. The spectral lines, however, do not reveal spatial information in an intuitive way. Software has therefore been created which is capable of assembling contour maps of integrated intensity over a range of velocities based on the data from the spectra (in this case we use the SPECX package).

Figure 10 shows the integrated intensity of the  $^{12}\text{CO}$   $J=3\rightarrow 2$  emission over all velocities. There are three main regions (or complexes) where the emission peaks: one in the north, one in the east and one in the southwest, and they are located around an almost circular area of low intensity. In Figures 11 (a, b, c and d) the integrated intensity maps are displayed sequentially for the velocity range between 0.25 km/s and 25 km/s. The intensity is integrated over 0.5 km/s intervals for velocities between 0.25 km/s to 5 km/s and 15 km/s to 25 km/s. For velocities between 5 km/s and 15 km/s, the intensity is integrated over 1 km/s intervals.

At the highest velocities of the approaching-gas maps in Figure 11 a there is significant emission only at the position of IRS 3 (0", 0"). As the velocity approaches that of the line centre (10.3 km/s), multiple features appear. The difference between the apparent intensity of the map at 4.75 and 5.50 km/s is not real; it is due to a change in the zero point of the intensity.

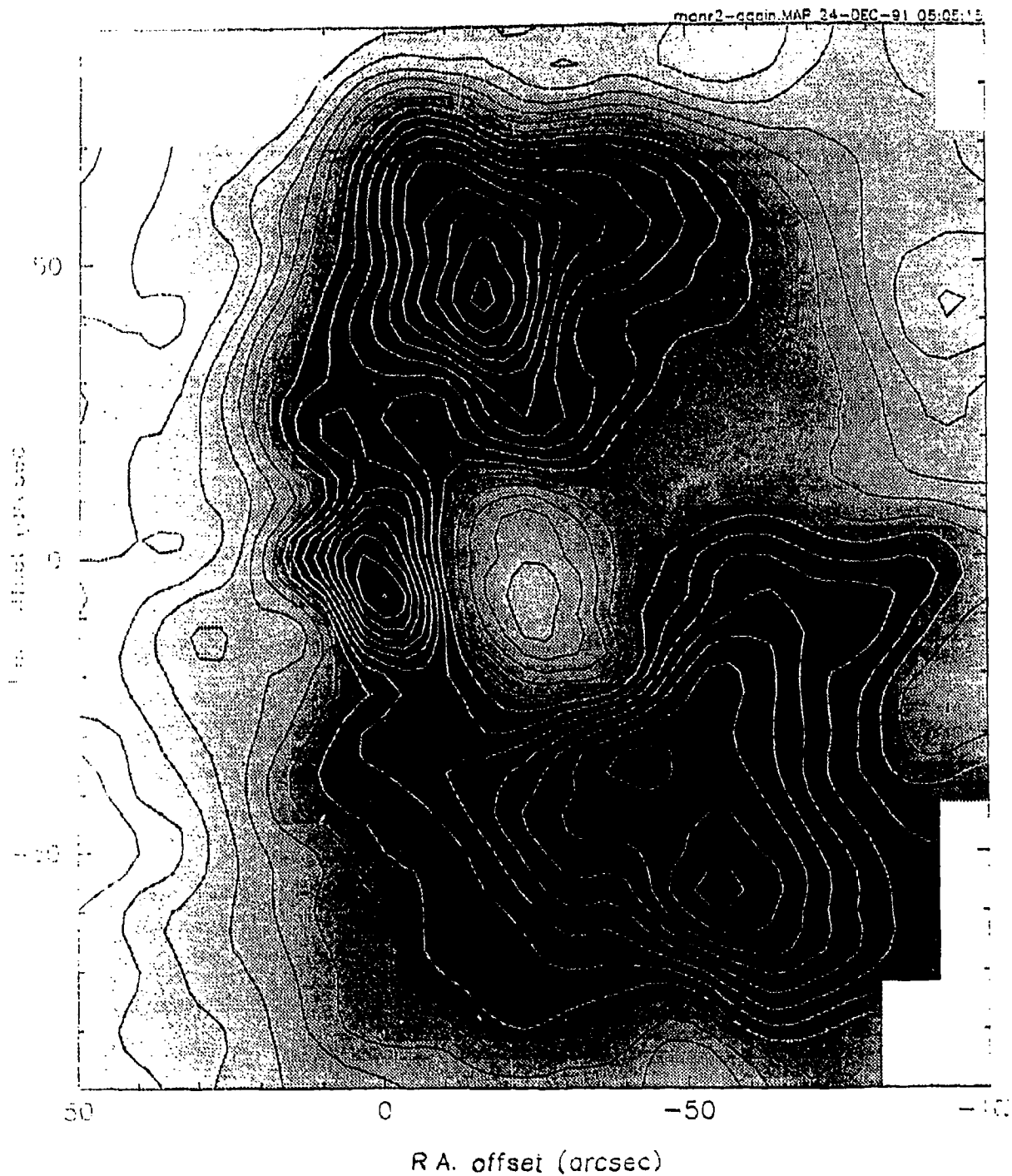


**Fig.10** The integrated intensity of the CO  $J=3 \rightarrow 2$  emission for all velocities where CO emission is clearly detectable (-10 km/s to 30 km/s). There are three main emission peaks: one in the north, one in the east and one in the southwest, which surround an almost circular area of low intensity. The lowest contour is at 70 K km/s, the interval between contours is 10 K km/s, and the highest contour is at 230 K km/s.



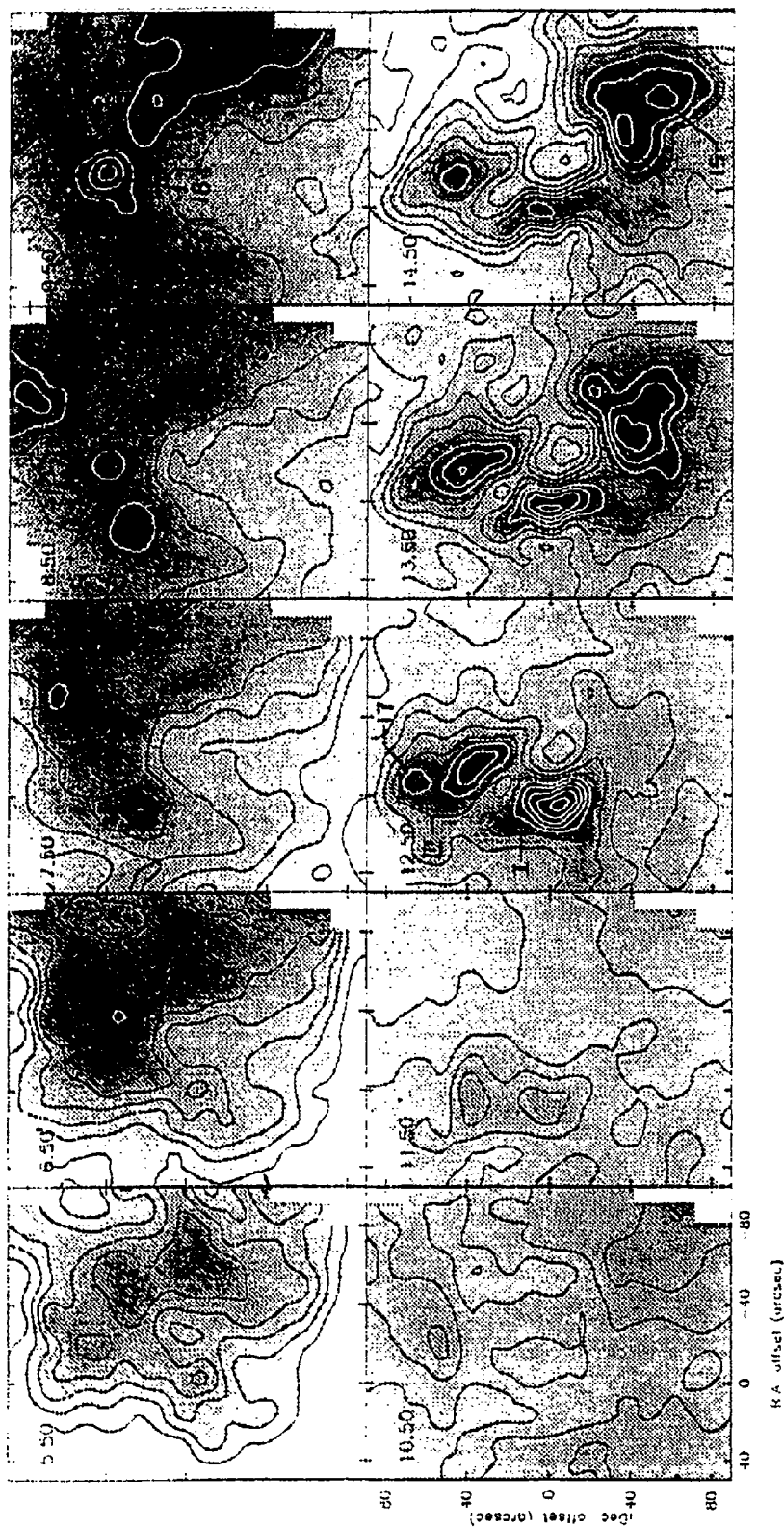


**Fig. 11 (b)** Integrated intensity over 1 km/s intervals for velocities between 5 km/s to 15 km/s. The contours differ by 2.5 K km/s. The velocity in the upper left corner in the panels denotes the middle of each velocity interval over which the intensity is integrated.

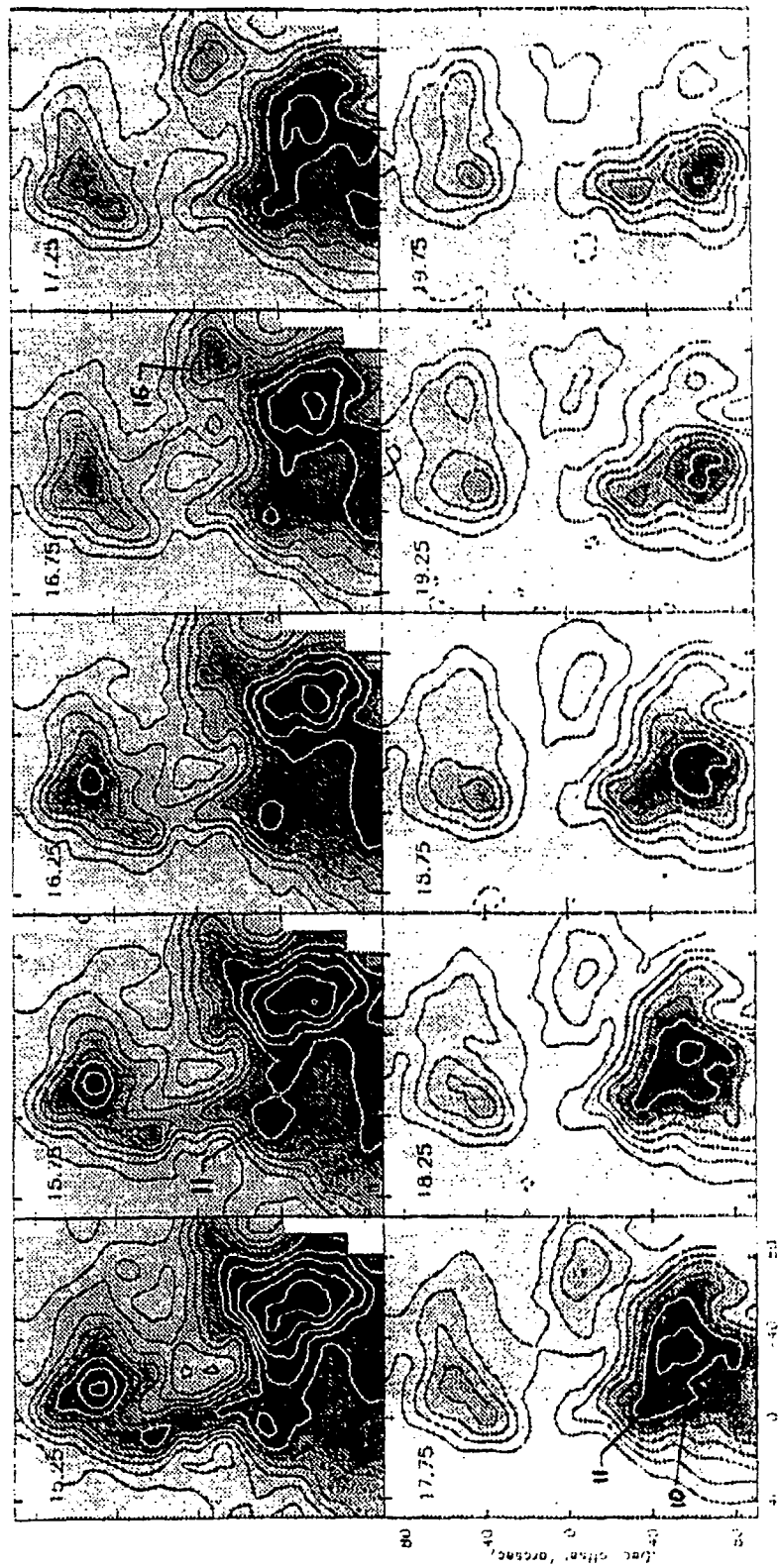


**Fig. 11 (c)** Integrated intensity over 1 km/s intervals for velocities between 15 km/s to 20 km/s. The contours differ by 1 K km/s. The velocity in the upper left corner in the panels denotes the middle of each velocity interval over which the intensity is integrated.

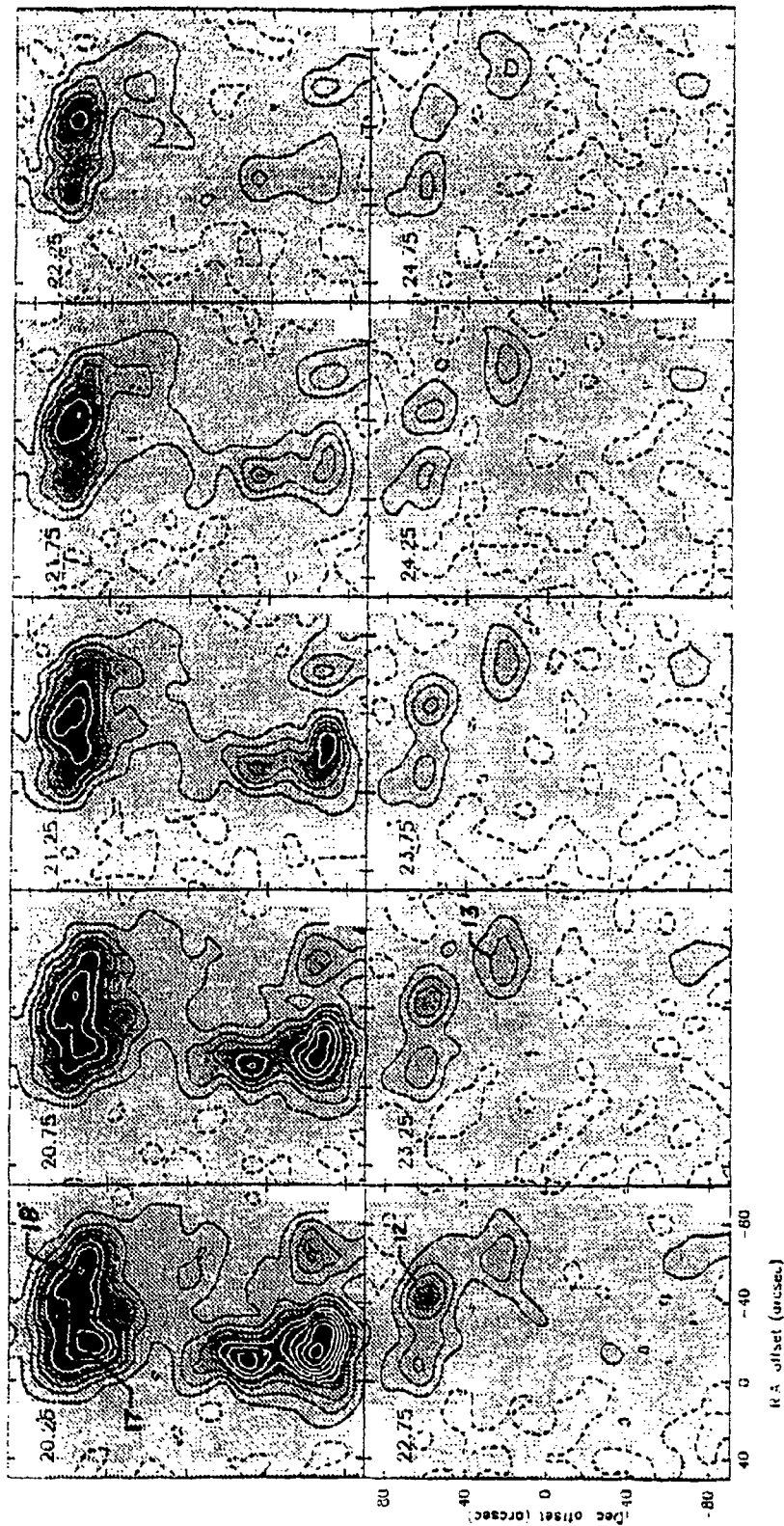


**Fig. 11 (d)** Integrated intensity over 0.5 km/s intervals for velocities between 20 km/s to 25 km/s. The contours differ by 0.5 K km/s. The velocity in the upper left corner in the panels denotes the middle of each velocity interval over which the intensity is integrated.

Each group of 10 channel maps has an independent scale chosen automatically by the software (SPECX) in order to accommodate the maximum intensity. Figures 11 b, c and d indicate that the general morphology of the receding gas changes and three new emission peaks appear at high velocities not present in the maps of approaching gas. Note that the maps for the velocity range between 10 and 12 km/s (two lower left in Figure 11b) are not representative due to the self-absorption of the gas, as discussed in Chapter V. An intriguing feature of all the maps is that there is an almost circular region that has a relatively low intensity in the centre of the core region. We will examine this in more detail in Chapter VI.

It is interesting that the CO emission shows no clear bipolarity in the channel maps and some positions have both approaching and receding gas. However, a widespread approaching component is concentrated toward the north part of the mapped region and a receding diffuse component lies preferentially on the south part of the region. For example, compare the 9.50 km/s channel (approaching gas) with the 16.75 km/s (receding gas).

We have already mentioned that there are two commonly-occurring absorption features in the  $^{12}\text{CO}$   $J=3\rightarrow 2$  spectra near 7.6 km/s and 11.3 km/s. The minimum seen at 7.6 km/s probably arises in a foreground cloud. The 11.3 km/s feature may result from the collapse of the self-absorbing outer layers of the cloud. Channel maps for velocities within 1 km/s of the velocity of the cloud are affected by the strong self-absorption dip seen in the spectra. Line intensities for these velocities are not a reliable measure of the column density.

It is attractive to interpret the CO intensity peaks as evidence for the presence of denser entities in the gas. It is clear from **Figure 11** that the channel maps show clumpiness on a variety of scales. We present a two-level qualitative description of the region consisting of complexes and clumps. A complex is a reasonably large, distinct region of enhanced intensity that has an irregular shape on the maps. Circular or oval intensity peaks within complexes will be referred to as clumps. Clumps have typical diameters of between 10" and 20" as opposed to about 60" for the complexes. We first examine the channel maps to find the large structures, i.e. the complexes. The discussion for the various individual clumps within each complex will follow.

There are two different groups of complexes, one for the approaching gas and one for the receding gas. Both groups form an incomplete ring-like structure around the circular area that represents an intensity minimum ("hole"). Note that, for brevity, the maps that have been integrated for approaching (or receding) velocities with respect to the centre of the line are referred to as maps of approaching (or receding) gas. The maps in **Figure 11 a** indicate the presence of four main complexes of approaching gas, referred to as A, B, C, D. **Figure 11 b** shows three complexes of receding gas, referred to as I, II and III. We discuss later the characteristics of the high-velocity clumps in each complex.

The first complex that appears in the maps of approaching gas is complex A. Complex A is in the east and is centered on IRS 3 at ( $\Delta\alpha = 0''$ ,  $\Delta\delta = 0''$ ). It is large (45" x 30") and has a circular shape until the velocity reaches 0.75 km/s. Thereafter it is elongated. Complex A includes clump 1 (0", -10")

is the brightest and most persistent clump. After 2.25 km/s, a second emission peak (clump 4) develops toward the northwest at (-15", 20"). Finally, there is another intensity peak (clump 9) at (15", -35) which appears at 4 km/s and is loosely associated with complex A.

Complex B is in the southwest (**Figure 11 a**) and is centered on (-50", -20"). B is more extended than A, with dimensions 60" x 50". The complex first appears at 1.25 km/s with two close but distinct clumps numbered 2 (-50", -20") and 3 (-50", -50"), of which clump 2 has a double structure and is by far the brightest in this complex. At 2.75 km/s, there is a northwest extension, clump 5 (-80", 0"), which has a complicated velocity structure (see **Figure 11 a**).

Complex C is in the north, centered on (-20", 50"). It appears at 2.75 km/s and persists until 5.5 km/s (**Figure 11 a and b**). Complex C has an elusive shape; however, its size is approximately 40" x 60". It embraces two peaks, clumps 6 (-5", 55") and 8 (-30", 65"). Complexes A and D seem to be aligned and well collimated. This is also true for B and C, but to a smaller extent.

Complex D (-50", 30") is in the northwest, becomes evident at 2.75 km/s, and is very prominent at 4.75 km/s (see **Figure 11 a**). This is the only complex that has no corresponding receding gas. Complex D is the smallest one (30"x 40"); it has an oval shape and it contains clump 7 (-55", 30").

The channel maps in **Figure 11 b, c and d** indicate the presence of three major complexes of emission from receding gas, although this separation is less natural than in the maps of approaching gas.

Complex I appears in the 11.5 km/s map (see **Figure 11 b**); it is very possible that the complex would appear in maps for smaller velocities if the channel maps were not distorted by the self-absorption of the gas. Complex I lies on the east side of the mapped region and is centered on (0", 0"). The complex has a very elongated shape, which looks like a bridge between complexes II and III. Complex I can be detected only to velocities of 15.25 km/s map and includes clump 1 (0", -10").

Complex II appears after 8.50 km/s and is present at least until 24.75 km/s. Its dimensions are in excess of 120" x 70", making it the largest complex. Complex II lies on the south portion of the mapped area. The approximate coordinates of its centre are (-40", -50"). Clumps 14 (-40", -35") and 15 (-50", -50") appear clearly at 14 km/s in the southwest and from this region clump 16 (-75", -10") is an offspring towards the northwest. In the velocity interval between 15 and 16 km/s, clumps 10 (-20", -65") and 11 (-10", -35") become apparent.

The shape of complex III changes significantly from an oval with a northeast-southwest to a northwest-southeast orientation. We estimate that it is approximately 60" x 80" centered on (-20", 60"). More distinct peaks (**Figures 11 b and d**) are clumps 13 (-75", 25"), 17 (-5", 65") and 18 (-20", 50"). Complex III is visible in the 12 km/s map in **Figure 11 d**, and is the only complex that is still seen at velocities as high as 30 km/s.

The receding complexes coincide fairly well spatially with the complexes in the approaching gas: I with A, II with B, III with C. Complex D

does not correspond to a peak in the maps of receding gas, representing instead a minimum of emission from receding gas. This minimum intensity seen towards the northwest in the receding gas (see Figure 11 b, c and d) is diametrically opposed to the minimum seen in the southeast in the maps of approaching gas with respect to the "hole".

Since all of the intensity peaks have been identified, a more thorough description of each one is appropriate. We have already seen cases where, for example, a receding clump has a corresponding approaching counterpart at the same position. If the clump is absent only in the problematic velocity ranges within 1 km/s of the two common absorption features (7.6 km/s and 11.3 km/s), then it will be assumed that the clump is present throughout the line centre. The properties (velocity range and position) of the distinct persistent clumps will be discussed in what follows. During this process, an attempt is made to justify the identification of the clumps. As will become obvious, it is to some degree a subjective matter. It is difficult to identify the clumps in a unique way. The main reason is that the peaks have complicated velocity structure.

Clump 1 (0", -10") is in complexes A and I. It covers velocities from -40 km/s to 7 km/s and from 11 km/s to 35 km/s, the largest velocity range of all the clumps. After 16 km/s, the peak becomes less distinct in the maps. However, the  $^{12}\text{CO } J=3\rightarrow 2$  spectral line shows that at this position there is gas with velocity as high as 35 km/s.

Clump 2 (-50", -20") is in complexes B and II, and appears at -20 km/s. Its orientation changes drastically: in the velocity interval from -20 to 9 km/s

it is directed along a southwest-northeast axis and for velocities larger than 9 km/s it is oriented northwest-southeast. There is some faint emission from the receding gas of this clump at 12 km/s, although it is very faint; clump 2 becomes gradually the brightest peak at a velocity of 14 km/s and vanishes when the velocity reaches 16 km/s.

Clump 3 (-50", -50") belongs to complexes B and II. It appears at a velocity of 1 km/s but most of the gas has a velocity of 6.5 km/s (**Figure 11 a**). It is probable that clump 3 is present at velocities close to the line centre, but it is not distinct due to the dominance of the quiescent gas. When clump 3 appears again at 13 km/s (**Figure 11 b**), it is not as prominent as clump 2, but by 15 km/s it is the most prominent clump in complex II (**Figure 11 c**). Clump 3 is still clearly visible in **Figure 11 d** and persists until 29 km/s.

Clump 4 (-15", 20") belongs to complex A and consists only of approaching gas with a velocity range of -15 to 9 km/s. In the receding maps it coincides with a local minimum of intensity (**Figure 11 b**).

Clump 5 (-80", 0") appears in both maps of receding (complex II) and approaching gas (complex B). In the former maps it ranges from 3 to 6.5 km/s and in the latter it spans from 14 to 20 km/s. It appears weakly on the 2 to 3 km/s map (**Figure 11 a**) but is unambiguously present in the 3 km/s channel map. The cut-off velocity for the approaching gas is considered to be 6.5 km/s, because the general intensity level is high around the clump, so the individual feature does not stand out. The receding gas in clump 5 is first seen at 14 km/s (**Figure 11 b and 2c**) and it vanishes for velocities of 20 km/s or more (**Figure 11 c**).

Clump 6 (-5", 55") belongs to complexes C and III. It first appears at 3 km/s (Figure 11 a). Although it is not very prominent between 6 and 7 km/s, at 9 km/s it appears to be the strongest peak (Figure 11 b). Therefore, it is believed that the approaching gas in this clump has velocities throughout the whole velocity range (3 to 10 km/s), since it has already been noted that the maps for the range of velocities between 6.5 and 8 km/s are contaminated by absorption. Clump 6 has receding gas which shows a complex velocity structure (Figure 11 c and d). It appears at 12 km/s and it can be seen until 29 km/s; after that velocity the signal is comparable to the noise.

Clump 7 (-55", 30") is in complex D. It is difficult to decide its velocity extent from individual maps; the signal is low. Hence, it is very useful to have integrated maps for large velocity ranges, which indicate that the clump spans from velocities from -25 to 6 km/s. Another approach is to check the spectrum at this position to see if there is any signal at these high velocities. A quick inspection reveals that there is emission at least to -20 km/s. The signal due to clump 7 seems insignificant in comparison with clump 1, especially in the vicinity of 0 km/s; therefore, it is not visible in all panels in Figure 11 a. It is, however, very prominent at 5 km/s (Figure 11 b). In the maps of receding gas clump 7 does not appear; at this position close to 10.3 km/s there is an intensity minimum. For larger velocities there is a corresponding clump, clump 13, but it is separated by 20" from clump 3.

Clump 8 (-30", 65") belongs to complex C. It appears at -5 km/s; its intensity is not much above the noise level, but is consistent in size and shape over a sizable velocity range. After 4.75 km/s, it becomes more

noticeable (**Figure 11 a and b**) until it vanishes after 9 km/s (**Figure 11 b**). For very high receding velocities, there is another peak due southwest, which is approximately at the same position (clump 12), but we consider them separately based on their appearance and evolution with velocity.

Clump 9 (15", -35") is seen over a very short velocity span from 4 to 7 km/s (**Figure 11 a and b**), so it is possible that this clump is relatively unimportant. It is considered an offspring of clump 1, so it belongs to complex A. The only likely corresponding emission peak in the receding gas maps is displaced by at least 20" to the west (**Figure 11 c**), so it is considered as a separate clump (11).

Clump 10 (-20", -65") is a receding clump: 16 to 23 km/s in complex II. At 17 km/s it is prominent (**Figure 11 c**). Clump 11 (-10", -35") is relatively close to 10, although it is not as bright, and its velocity ranges from 15 to 24 km/s.

Clump 12 (-55", 50") is a westward extension of complex III (**Figure 11 d**). Its velocity ranges between 18 and 27 km/s. There is another strong peak in the west part of complex III (**Figure 11 d**) which is referred to as clump 13 (-75", 25"). Its velocity range is 22 to 30 km/s and for channel maps with velocities larger than 26 km/s, it is the strongest peak.

Clumps 14 (-40", -35"), 15 (-50", -50"), and 16 (-75", -10") belong to complex II (**Figure 11 a and c**). They are considered to be receding gas from clump 2, clump 3, and clump 5, respectively.

Clump 17 (-5", 65") is in complex III and has a small velocity range; only 12 to 15 km/s (**Figure 11 b**). Also, it is closely related to clump 18, so it is not considered a separate clump. Clump 18 (-20", 50") belongs to complex III too. Its velocity ranges seen in the maps of receding gas (12 to 17 km/s) implies that clump 18 is the receding part of clump 6 (**Figure 11 b and c**). Therefore, it is also not thought to be a separate clump.

We will summarize the clumps that are considered real in **Table II**. The table includes the complex in which the clump belongs, the velocity range in the approaching and/or the receding gas, the position in the map, and, finally, the position of the closest point to the clump, where there are available observations of all three transitions of  $^{12}\text{CO}$  and  $^{13}\text{CO}$ . We should note that the position of the clump is the average position of the centre of the clump. With this information we can proceed to find physical characteristics of these clumps.

TABLE II  
 CHARACTERISTICS OF THE HIGH-VELOCITY CLUMPS  
 SEEN IN THE  $^{12}\text{CO } J=3 \rightarrow 2$  MAP

Clump Number	Complex	Velocity range of approaching gas (km/s)	Velocity range of receding gas (km/s)	Position on map	Closest position with $^{13}\text{CO}$ spectra
1	A, I	-40 to 7	11 to 35	0", -10"	2 (0",0")
2	B, II	-20 to 9	13 to 16	-50", -20"	8 (-40",-40")
3	B, II	1 to 6.5	13 to 29	-50", -50"	10 (-50",-60")
4	A	-15 to 9	-	-15", 20"	1 (10", 20")
5	B, II	3 to 6.5	14 to 20	-80", 0"	11 (-60",-10")
6	C, III	3 to 10	12 to 29	-5", 55"	7 (-20",40")
7	D	-25 to 6	-	-55", 30"	12 (-80",30")
8	C	-5 to 9	-	-30", 65"	9 (-40", 60")
9	A	4 to 7	-	15", -35"	3 (-10",-20")
10	II	-	16 to 23	-20", -65"	5 (-20",-70")
11	II	-	15 to 24	-10", -35"	3 (-10",-20")
12	III	-	18 to 27	-55", 50"	9 (-40", 60")
13	III	-	22 to 30	-75", 25"	12 (-80",30")

## IV. DERIVATION OF PHYSICAL PARAMETERS

The mass of the high velocity gas is a key parameter in understanding its energetics. In order to find the mass, it is necessary to determine the optical depth and the column density of the gas. A brief summary is given below explaining how these quantities are obtained.

### a. Optical depth

The optical depth can be calculated from the ratio of radiation temperatures for two isotopes of CO. The radiation temperature,  $T_R$ , is directly related to the observable quantity  $T_A^*$  (antenna temperature) and is defined by

$$I_\nu d\nu = \frac{2\nu^2}{c^2} k T_R d\nu, \quad (1a)$$

where  $I_\nu$  is the observed intensity of the source at frequency  $\nu$ ,  $c$  is the speed of light, and  $k$  is the Boltzmann constant.

The solution for the transfer equation is approximated by the solution for a uniform medium

$$I_\nu = (1 - e^{-\tau_\nu}) B_\nu(T_m), \quad (1b)$$

where  $B_\nu$  is the Planck function for gas at excitation temperature,  $T_{ex}$ . The excitation temperature is equal to the kinetic temperature,  $T_{kin}$ , if local thermodynamical equilibrium (LTE) holds. From equation (1a), (1b) and the relation between the observed antenna temperature and the radiation temperature we obtain the following

$$T_R = \frac{T_A^*}{\eta_B f} = (1 - e^{-\tau_\nu}) \frac{h\nu/k}{e^{h\nu/kT_{ex}} - 1}, \quad (2)$$

where  $T_A^*$  is the antenna temperature corrected for atmospheric and telescope losses,  $\eta_B$  is the beam efficiency which takes the side-lobe losses of the telescope beam into account,  $\tau_\nu$  is the optical depth at frequency  $\nu$ ,  $h$  is the Planck constant, and  $f$ , is the beam filling factor, i.e. the fraction of the beam filled by the source.

We apply equation (2) to the data for each of the two species, e.g.,  $^{12}\text{CO}$   $J=3 \rightarrow 2$  and  $^{13}\text{CO}$   $J=3 \rightarrow 2$ , under the assumption that they share a common excitation temperature (the two isotopes have very similar energy levels and transition probabilities). If we ignore the small difference in emitting frequencies of the two isotopes (345 GHz vs. 330 GHz), the ratio of radiation temperatures is

$$\frac{T_R^{12}}{T_R^{13}} = \frac{T_A^{*12}}{T_A^{*13}} \cong \frac{1 - e^{-\tau_\nu^{12}}}{1 - e^{-\tau_\nu^{13}}}, \quad (3)$$

in which  $f$  (which is unknown) and  $\eta_B$  are eliminated. If we further assume an abundance ratio for the two isotopes of  $\frac{^{12}\text{C}}{^{13}\text{C}} \cong 60$  (Langer and Penzias, 1990), then

$$\frac{\tau_\nu^{12}}{\tau_\nu^{13}} \cong 60. \quad (4)$$

From equation (4) one can solve for both  $\tau_\nu^{12}$  and  $\tau_\nu^{13}$  using equation (3) with the known ratio of antenna temperatures.

### b. Excitation temperature

Once the optical depths are known, the excitation temperature can be determined from equation (2) if the value for the filling factor  $f$  is known. We assume  $f = 1$ , which will be justified later. Thus, the excitation temperature is given by

$$T_{ex} = \frac{h\nu}{k} \left\{ \ln \left[ 1 + \frac{h\nu}{kT_R(\nu)} (1 - e^{-\tau_\nu(\nu)}) \right] \right\}^{-1}. \quad (5)$$

### c. Column density

If the optical depth and the excitation temperature are known, the column density can be calculated. The optical depth is defined as

$$\tau_v = \int_0^l k_v dz, \quad (6)$$

where  $z$  is the distance light travels through the gas. The absorption coefficient,  $k_v$ , is given by

$$k_v = \frac{h\nu}{4\pi} (n_l B_{lu} - n_u B_{ul}), \quad (7)$$

where  $n_l$  and  $n_u$  are number densities for the upper and lower molecular populations, respectively,  $l$  and  $u$  are the rotational quantum numbers of the lower and upper states,  $B_{lu}$  is the Einstein absorption probability, and  $B_{ul}$  is the Einstein probability for stimulated emission.

The absorption probability depends linearly upon the rate of spontaneous de-excitation,  $A_{ul}$ , which is given by

$$A_{ul} = \frac{64\pi^4 \nu^3}{3hc^3} \mu^2 \frac{u}{g_u}, \quad (8)$$

where  $\mu$  is the electric dipole moment of the molecule and  $g_u$  is the statistical weight of the upper level. If  $k_v$  is substituted in equation (6) and the medium is assumed to be in LTE, which allows us to use the Boltzmann equation  $\left( \frac{n_l g_u}{n_u g_l} = e^{h\nu/kT_r} \right)$ , the optical depth is given by

$$\tau_v = \frac{c^2}{8\pi\nu^2} A_{ul} \frac{g_u}{g_l} N_l(\nu) \left( 1 - e^{-h\nu/kT_r} \right), \quad (9)$$

where  $N_l$  is the column density of molecules in the lower rotational level. [For a detailed derivation of equation (9) see Lee 1992.]

For a linear molecule  $g_u = 2u + 1$ . Equation (9) yields the lower state column density for some frequency interval, but it is often more practical to integrate over velocity intervals. Furthermore, the total column density is necessary to calculate the mass of the gas, so all rotational levels have to be taken into account. By using the Boltzmann equation with equation (9), we find for a linear molecule that the total column density integrated over all velocities is

$$N_{tot} = \int \frac{3k}{8\pi^3 B \mu^2} \frac{1}{u} \left( T_{ex} + \frac{hB}{3k} \right) e^{hB(u+1)/kT_{ex}} \left( 1 - e^{-hv/kT_{ex}} \right)^{-1} \tau_v dv, \quad (10)$$

where  $B$  is the rotational constant of the molecule in question,  $v$  is velocity measured in km/s and  $N_{tot}$  is calculated in  $\text{cm}^{-2}$ . In the case of CO,  $B = 5.764 \times 10^{10}$  Hz and  $\mu = 1.12 \times 10^{-19}$  esu cm (Chantry 1979). Thus, for the  $^{12}\text{C} \text{O}$   $J=3 \rightarrow 2$  transition the total column density (in  $\text{cm}^{-2}$ ) is:

$$N_{tot} = \int 0.80 \times 10^{14} (T_{ex} + 0.92) e^{16.592/T_{ex}} \left[ 1 - e^{-16.592/T_{ex}} \right]^{-1} \tau_v^3 dv. \quad (11)$$

Since the main constituent of the cloud is molecular hydrogen, one needs to relate the column density of CO obtained above to the column density of  $\text{H}_2$  in order to estimate its mass. Here we use the abundance ratios of  $\frac{N(^{12}\text{C})}{N(^{13}\text{C})} = 60$  and  $\frac{N(^{12}\text{CO})}{N(\text{H}_2)} = 1 \times 10^{-4}$ . These relative abundances are actually

uncertain, but the assumed ratios will probably introduce uncertainties of less than a factor of 2 in the determination of the mass of the CO clumps.

#### d. Mass

The mass of the H<sub>2</sub> gas in the clump is found by multiplying the total column density by the assumed area of the clump, A, and the mass of a hydrogen molecule m<sub>H<sub>2</sub></sub>. The mass (in M<sub>⊙</sub>) is given by

$$M(\text{H}_2) = (10^4 \times N(^{12}\text{CO}) \times m_{\text{H}_2} \times A) / 2 \times 10^{33}. \quad (12)$$

The diameters of the high-velocity gas clumps are approximately equal to the size of the beam; therefore, the  $A = \pi r^2 = 2.732 \times 10^{34} \text{ cm}^{-2}$ , where  $r = 0.03 \text{ pc}$ . The accuracy of this calculation depends quite strongly on the uncertainty in the distance. Specifically, the value of the mass obtained for an assumed distance to Mon R2 of 830 pc will be only 76% of the value calculated for a distance of 950 pc.

Finally, in order to obtain the total mass of a clump, we must take into account the fractional helium abundance (10% by number). Thus, the total mass of a clump in solar units is

$$\begin{aligned} M &= 1.4 \times M(\text{H}_2) \\ &= 9.25 \times 10^{-19} \times N(^{12}\text{CO}) \quad M_{\odot}. \end{aligned} \quad (13)$$

### e. Excitation temperature and mass in the optically thin limit

In our previous discussion, it was assumed for the calculation of the total column density that the optical depth was known. This is not necessary, however, if the optically thin approximation is valid (i.e.  $\tau_v \ll 1$ ). Then, equation (2) becomes

$$T_R = \frac{T_A^*}{\eta_B f} \cong \tau_v \frac{h\nu/k}{e^{h\nu/kT_{ex}} - 1}. \quad (14)$$

The filling factor is again assumed to be unity. The optical depth can be eliminated from equation (14) if we use equation (9). Then, the expression for the ratio of  $T_R$  evaluated for two different transitions ( $J_1 \rightarrow J_1 - 1$  and  $J_2 \rightarrow J_2 - 1$ ) depends only on  $T_{ex}$  and the molecular constants. In the case of CO

$$\frac{T_R(J_1 \rightarrow J_1 - 1)}{T_R(J_2 \rightarrow J_2 - 1)} = \frac{J_1^2}{J_2^2} \exp\left\{-\frac{2.77}{T_{ex}} [J_1(J_1 + 1) - J_2(J_2 + 1)]\right\}. \quad (15)$$

Note that for the calculation of the column density in the optically thin limit we do not assume a value for the filling factor; we just assume that  $^{12}\text{CO}$  and  $^{13}\text{CO}$  gas share the same filling factor. In this case we are interested in the  $J=3 \rightarrow 2$  and  $J=2 \rightarrow 1$  transitions of  $^{12}\text{CO}$ , for which we obtain:

$$T_{ex} = \frac{16.59}{\ln\left[\frac{4 T_R^{3 \rightarrow 2}}{9 T_R^{2 \rightarrow 1}}\right]}, \quad (16)$$

where  $T_R^{3 \rightarrow 2}$  and  $T_R^{2 \rightarrow 1}$  are the radiation temperatures for the  $J=3 \rightarrow 2$  and  $J=2 \rightarrow 1$  transitions of CO, respectively. It has already been noted that the two

transitions have different beam efficiencies. Thus, from equation (14) the ratio of radiation temperatures is equal to the ratio of the antenna temperatures multiplied by  $\frac{\eta_B^{(2 \rightarrow 1)}}{\eta_B^{(3 \rightarrow 2)}} = \frac{0.63}{0.50} = 1.26$ .

We can calculate the total column density by substituting the results of equation (9) in equation (14), by using  $\frac{dv}{v} = \frac{dv}{c}$ , i.e.

$$N_l = \int \frac{3k}{8\pi^3 v \mu^2} \frac{2l+1}{u} e^{hv/kT_a(v)} T_R(v) dv. \quad (17)$$

Therefore, the general equation for the total column density in the optically thin limit is

$$N_{tot} = \int \frac{3k^2 T_{ex}(v)}{8\pi^3 h B v \mu^2} \frac{1}{u} e^{(u+1)hv/kT_a(v)} T_R(v) dv. \quad (18)$$

For the  $^{12}\text{CO } J=3 \rightarrow 2$  transition (when  $\tau_v \ll 1$ ),

$$N_{tot} = \int 4.64 \times 10^{12} T_{ex}(v) e^{33.18/T_a(v)} T_R^{3 \rightarrow 2}(v) dv. \quad (19)$$

For the  $^{12}\text{CO } J=2 \rightarrow 1$  transition (when  $\tau_v \ll 1$ ),

$$N_{tot} = \int 1.05 \times 10^{13} T_{ex}(v) e^{16.59/T_a(v)} T_R^{2 \rightarrow 1}(v) dv. \quad (20)$$

In summary, the excitation temperature (in K) is calculated from equation (5) for the velocity range where  $^{13}\text{CO}$  is detectable. Hence, the optical

depth can be determined. Equation (16) is used to calculate the temperature when the optical depth is relatively small. For velocity intervals that the optical depth is known, the total column density (in  $\text{cm}^{-2}$ ) is calculated from equation (11). For the velocities where the gas is optically thin,  $N_{\text{tot}}$  is given by equation (19). We will present these calculations based upon our data in the next Chapter (V).

## V. ANALYSIS OF OBSERVATIONS

### a. Optical depth versus velocity

Equation (3) relates the optical depth for  $^{12}\text{CO}$  and  $^{13}\text{CO}$  emission ( $\tau^{12}$  and  $\tau^{13}$ ) to the ratio of the radiation temperatures of the two isotopes. The radiation temperature is directly associated with the antenna temperature,  $T_A^*$ , the observed quantity. The principal assumptions are that each species has the same excitation temperature and the same filling factor. In this case, observations of the rotational transition  $J=3\rightarrow 2$  of  $^{12}\text{CO}$  and  $^{13}\text{CO}$  are used.

From equation (3) the optical depth for  $^{13}\text{CO } J=3\rightarrow 2$  and  $^{12}\text{CO } J=3\rightarrow 2$  emission is calculated for the range of velocities where  $^{13}\text{CO}$  can be detected. Since the values of  $\tau^{12}$  and  $\tau^{13}$  will behave in exactly the same way, we will discuss the variation of the optical depth of  $^{13}\text{CO}$  with velocity. The optical depth versus velocity is plotted for all 12 positions where  $^{13}\text{CO}$  was detected in **Figure 12** (i and ii). The error bars of the optical depth are included. Identical trends are apparent at all positions, namely the optical depth is small for velocities large relative to the line centre and it peaks close to the line centre, i.e. at 10.3 km/s.

It must be emphasized that the CO emission is saturated within 1 km/s from the line centre. This is evident from the value of  $T_A^*(^{12}\text{CO})/T_A^*(^{13}\text{CO})$  in the vicinity of 10.3 km/s, which is close to unity and can be less than unity.

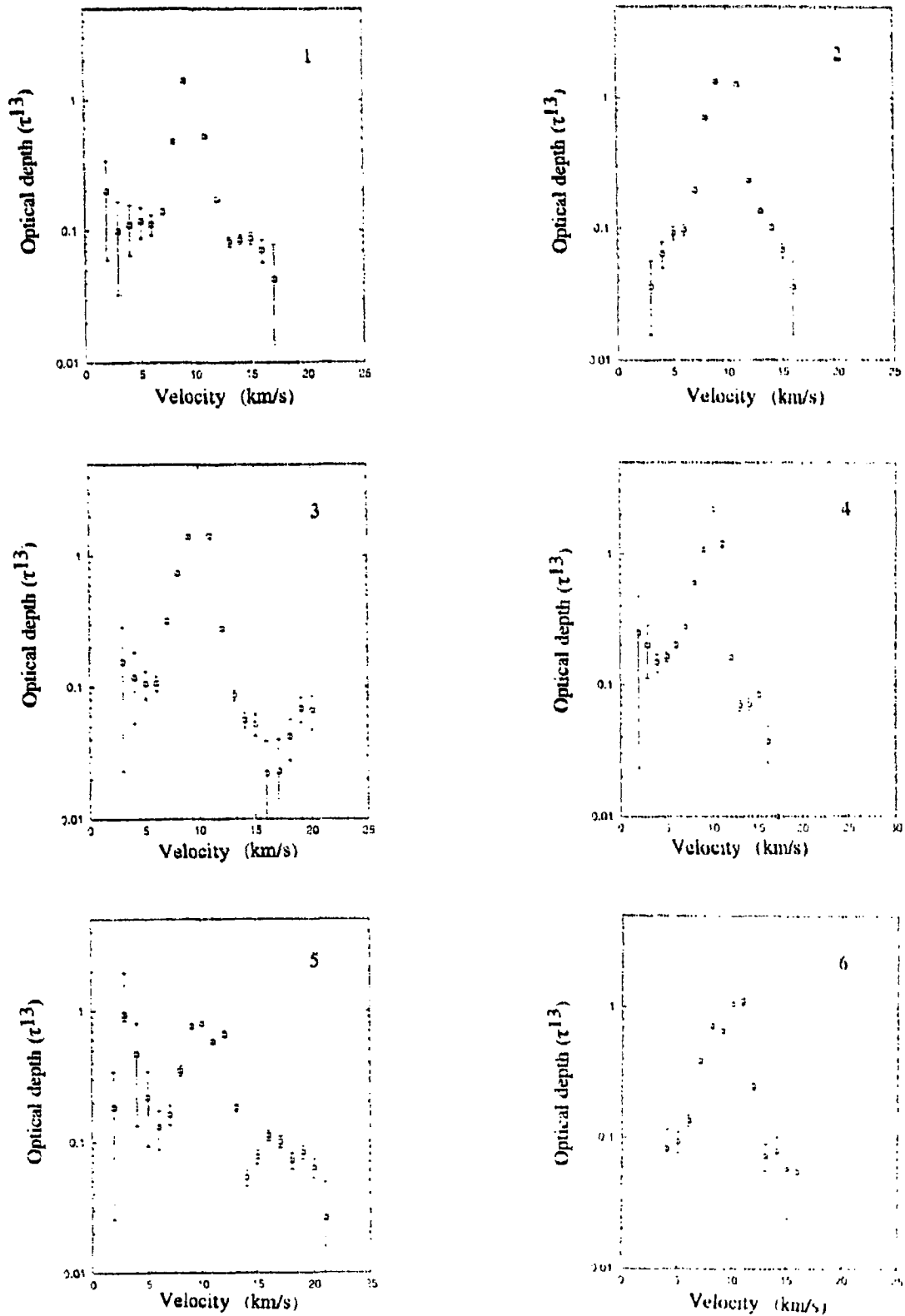


**Fig. 12 i** The optical depth for  $^{13}\text{CO}$  ( $\tau^{13}$ ) versus velocity is plotted for positions 1 to 6 where  $^{13}\text{CO}$  observations were made. The position number is indicated within each diagram. The error bars of the optical depth are included. In most cases the optical depth increases towards the line centre (10.3 km/s).

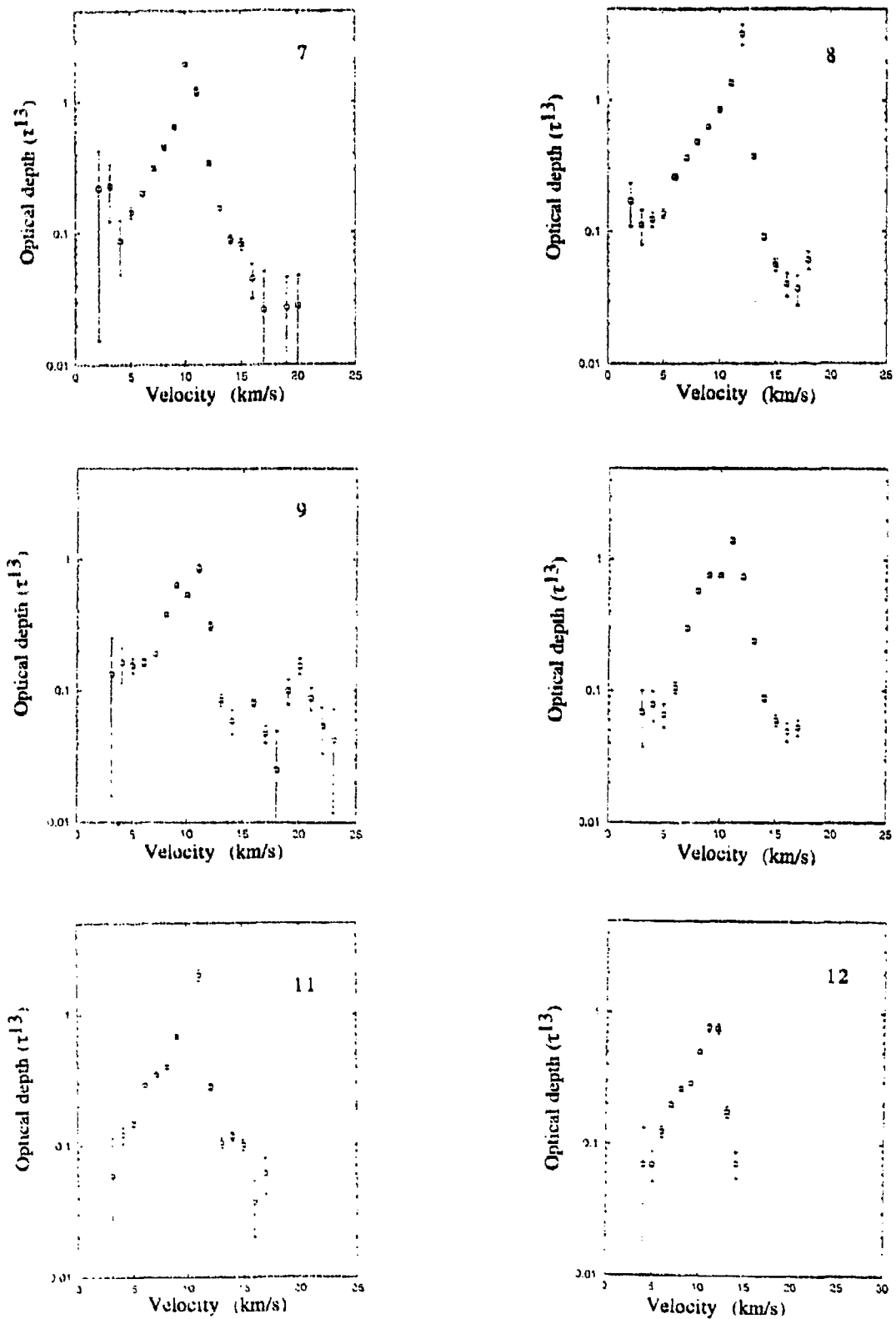


**Fig. 12 ii** The optical depth for  $^{13}\text{CO}$  ( $\tau^{13}$ ) versus velocity is plotted for positions 7 to 12 where  $^{13}\text{CO}$  observations were made. The position number is indicated within each diagram. The error bars of the optical depth are included. In most cases the optical depth increases towards the line centre (10.3 km/s).

A ratio smaller than unity implies  $\tau^{13} > \tau^{12}$ , which is not plausible since  $^{12}\text{CO}$  is typically two orders of magnitude more abundant than  $^{13}\text{CO}$ . The most likely explanation for such small values for the ratio of antenna temperatures is that  $^{12}\text{CO}$  is optically thick and has a self-absorption dip, while  $^{13}\text{CO}$  being more optically thin, suffers less self-absorption. Whenever  $T_{\text{A}}^*(^{12}\text{CO})/T_{\text{A}}^*(^{13}\text{CO})$  is near unity, we cannot find a reliable value for the optical depth.

The optical depth tends to decrease away from the line centre. In most cases, the decrease is by at least one order of magnitude from a maximum value of  $\tau^{13}$  between 1 and 3 to a minimum value between 0.008 and 0.18. The minimum value is set by the detection limit of the  $^{13}\text{CO}$  emission. Although for most positions there is a smooth variation of the optical depth with velocity, the optical depth at positions 5 and 9 exhibit significant variations with velocity. This may be due to the complicated structure of the lines at these positions (see **Figure 8**).

In the analysis that follows it is assumed that the main source of error is the noise in the data, i.e. the finite value for the signal-to-noise ratio of the spectra. The root-mean-square (rms) uncertainty of the antenna temperature,  $T_{\text{A}}^*_{\text{rms}}$ , for the various transitions is slightly different since the quality of the spectra is not identical. We estimate the standard deviation of the antenna temperature by using a function of the SPECX package that does this automatically. We find that the standard deviations for the three transitions are:  $\sigma T_{\text{A}}^*(^{12}\text{CO } 3 \rightarrow 2) = 0.13 \text{ K}$ ,  $\sigma T_{\text{A}}^*(^{13}\text{CO } 3 \rightarrow 2) = 0.10 \text{ K}$ , and  $\sigma T_{\text{A}}^*(^{12}\text{CO } 2 \rightarrow 1) = 0.13 \text{ K}$ . Following Bevington (1969), we calculate the error in the value of the optical depth due to the propagation of the uncertainties in the antenna

temperatures. Our conclusion from this analysis is that the uncertainties involved in evaluating the optical depth relatively close to the centre of the line are small (typically less than 8%). It is not very useful to estimate the statistical error of the optical depth at the line centre since it is not well determined. For high-velocity gas the error increases dramatically to more than 20%. **Figure 13** demonstrates for position 1 (10", 20") as an example, that the uncertainty in the excitation temperature is fairly constant, even if the error in the optical depth is high. Thus, the large uncertainties in the calculation of the optical depth do not introduce severe problems in the estimate of the excitation temperature.

For the calculations that follow it is assumed for velocities where  $^{13}\text{CO}$  emission cannot be detected that  $^{12}\text{CO}$  gas is optically thin, or equivalently,  $\tau_v \cong (1 - e^{-\tau_v})$ . Is this statement valid? We find that the optical depth for  $^{13}\text{CO}$  gas has to be less than 0.003 (or  $< 0.15$  for  $^{12}\text{CO}$ ) for the uncertainty of the optically thin approximation to be acceptably small (less than 8%). If  $\tau^{13} > 0.008$ , the error introduced by the approximation is more than 25% and rises steeply with increasing optical depth. However, the average value for the minimum measurable optical depth for all positions is much higher,  $\tau^{13} = 0.08$  ( $\tau^{12} = 60 \times 0.08 = 4.8$ ). Thus, we conclude that the  $^{12}\text{CO}$  gas is, in general, not necessarily optically thin when  $^{13}\text{CO}$  cannot be detected because of the significant difference in their abundance. The portion of the spectral line that has an observable counterpart in  $^{13}\text{CO}$  emission is referred to as the "optically thick region" while the rest of the line is referred to as the "optically thin region", even though these labels may not always be completely justified. For velocities where  $^{13}\text{CO}$  is not detectable, the optically thin approximation must be made.

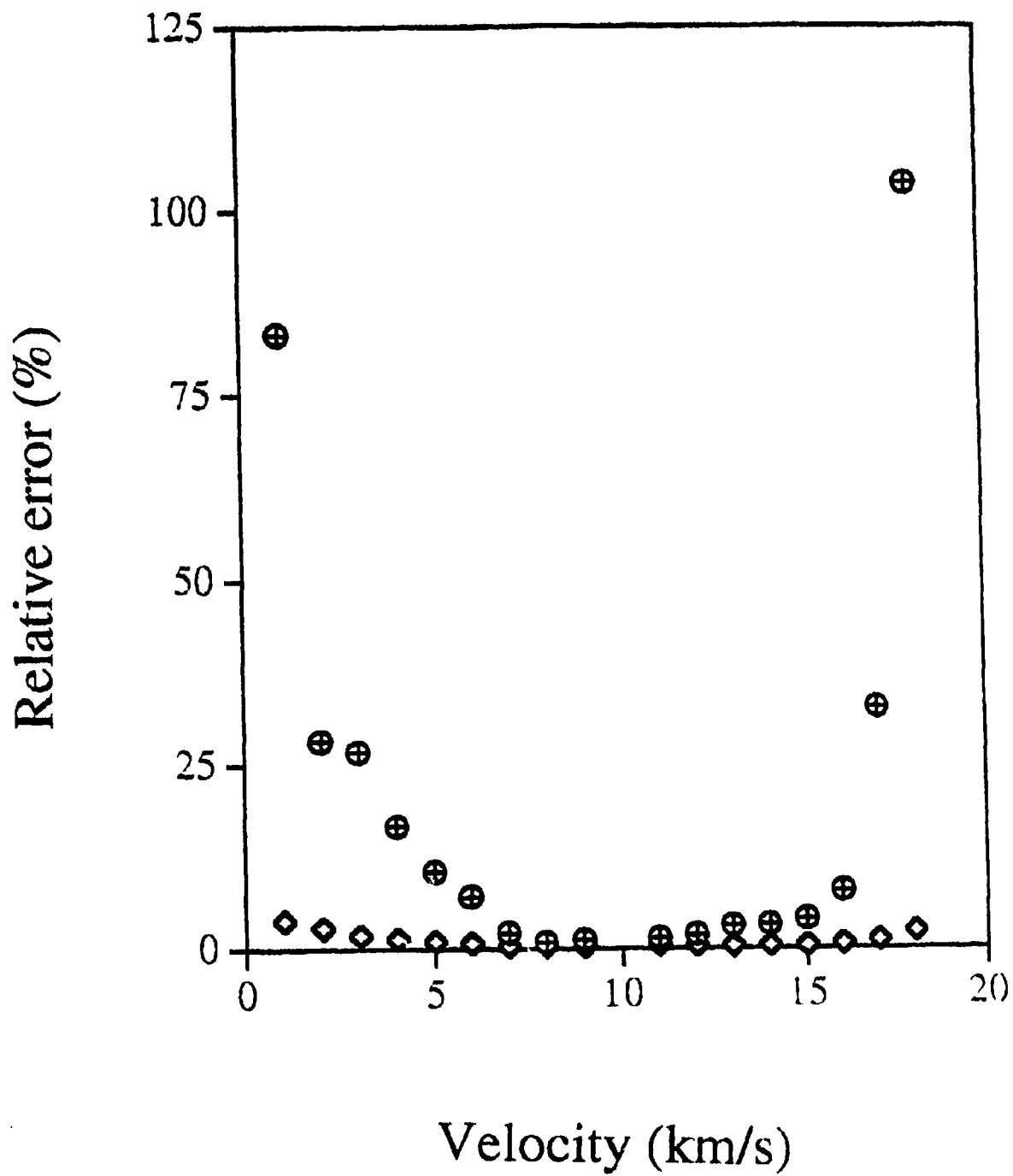


**Fig. 13** The uncertainties (%) in the optical depth (⊕) and in the excitation temperature (◇) versus velocity for position 1 (10", 20"). The large uncertainties in the optical depth do not introduce large uncertainties in the excitation temperature.

## b. Excitation temperature versus velocity

It has been illustrated that the excitation temperature,  $T_{\text{ex}}$ , can be estimated once the optical depth is known. This is done using equation (5), which involves the radiation temperature of a transition for two isotopes of the same species (in this case  $^{12}\text{CO}$  and  $^{13}\text{CO}$   $J=3\rightarrow 2$ ). Thus, we can compute the excitation temperature,  $T_{\text{thick}}$ , for the velocity range over which the radiation temperature of  $^{13}\text{CO}$  can be found from the measured antenna temperature. Outside that velocity range, in the "optically thin" region, since we cannot directly determine the optical depth we must assume that the optical depth is small, or that  $\tau_{\nu} \cong (1 - e^{-\tau_{\nu}})$ . Then, if we have observations of two transitions of the same isotope (here  $^{12}\text{CO}$   $J=3\rightarrow 2$  and  $J=2\rightarrow 1$ ), we can use equation (16) to calculate the excitation temperature,  $T_{\text{thin}}$ . In our previous discussion we concluded that this approximation is often poor.

In **Figure 14**, we present a plot of the excitation temperature versus velocity for the twelve positions, as derived from both methods; this figure includes the error bars for  $T_{\text{thin}}$  and  $T_{\text{thick}}$  when they are larger than the symbol that represents the value of the excitation temperature. In two positions, 4 and 11, we present both  $T_{\text{thin}}$  and  $T_{\text{thick}}$  for high velocities to compare their trends and to check if they are consistent with each other.

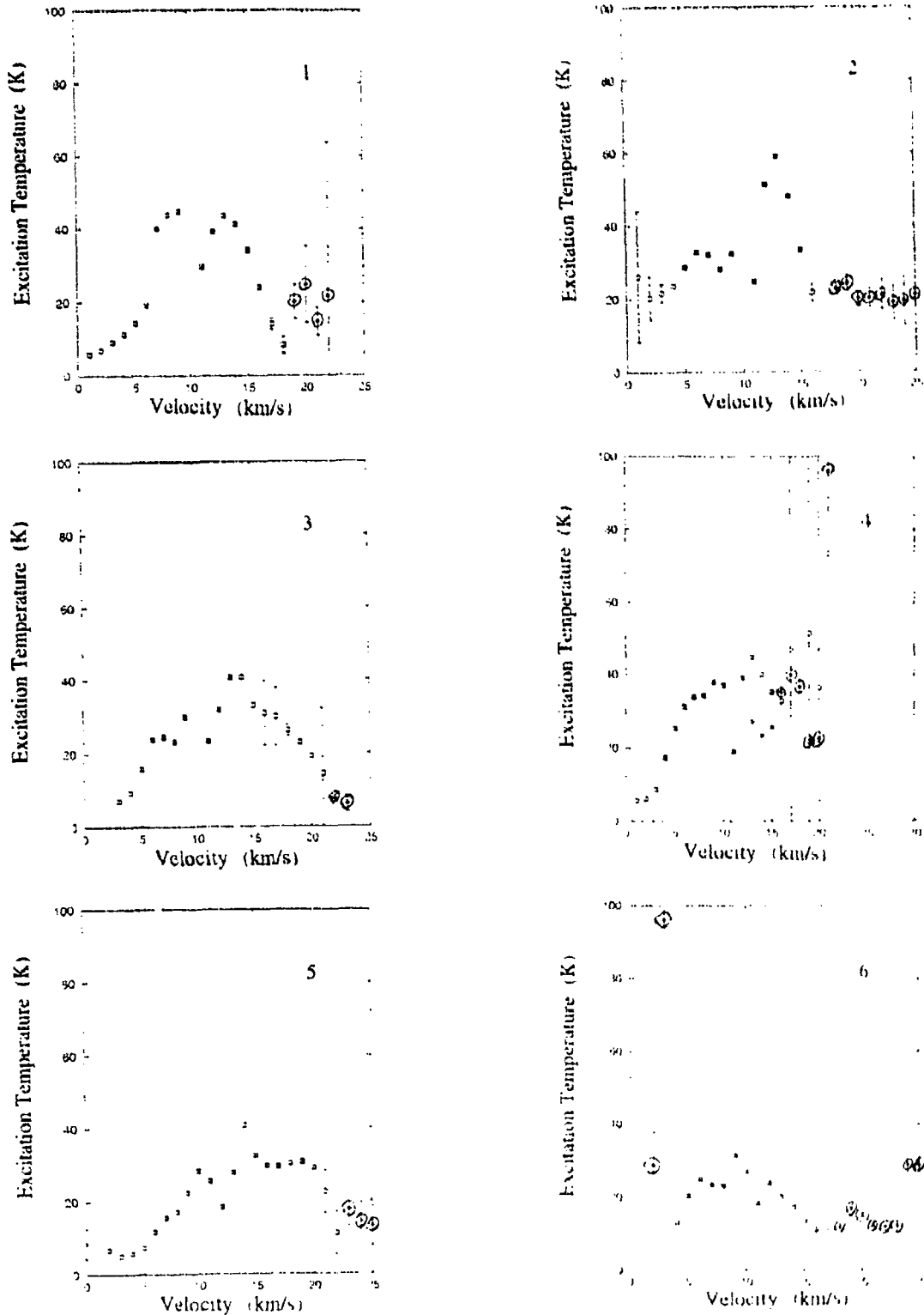


**Fig. 14 i** Excitation temperature,  $T_{\text{ex}}$ , versus velocity for positions 1 to 6 from both methods, including the error bars of  $T_{\text{thick}}$  ( $\square$ ) and  $T_{\text{thin}}$  ( $\odot$ ). The position number is indicated within each diagram. Whenever the error bar does not appear, it is smaller than the symbol that represents the point. The drop of the excitation temperature very near the  $^{13}\text{CO}$  peak is due to the self-absorption of  $^{12}\text{CO}$ . The excitation temperatures from the two methods are consistent:  $T_{\text{thin}}$  generally follows the extrapolated curve from the  $T_{\text{thick}}$  values.

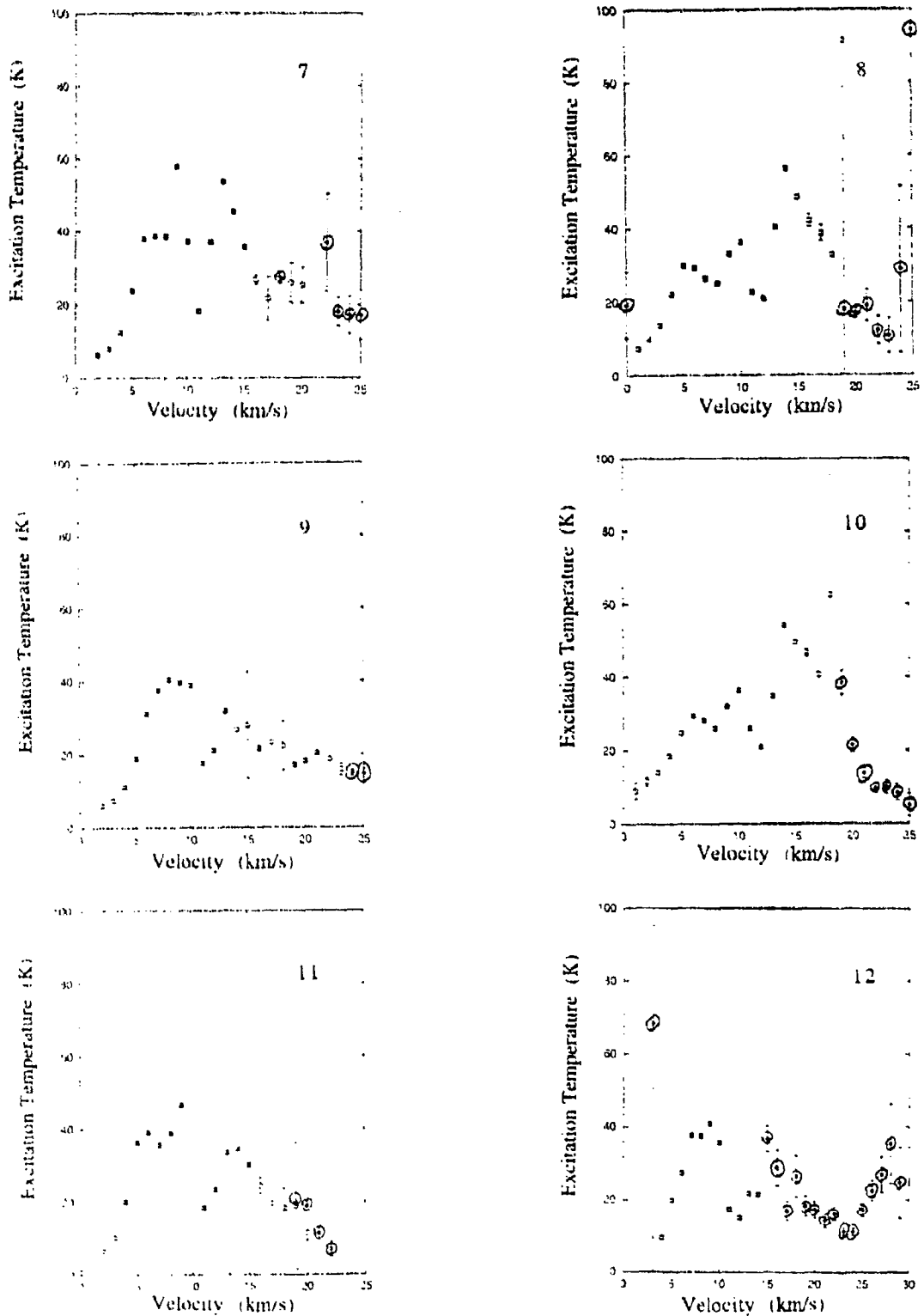


**Fig. 14 ii** Excitation temperature,  $T_{\text{ex}}$ , versus velocity for positions 7 to 12 from both methods, including the error bars of  $T_{\text{thick}}$  ( $\square$ ) and  $T_{\text{thin}}$  ( $\odot$ ). The position number is indicated within each diagram. Whenever the error bar does not appear, it is smaller than the symbol that represents the point. The drop of the excitation temperature very near the  $^{13}\text{CO}$  peak is due to the self-absorption of  $^{12}\text{CO}$ . The excitation temperatures from the two methods are consistent:  $T_{\text{thin}}$  generally follows the extrapolated curve from the  $T_{\text{thick}}$  values.

The data of **Figure 14 (i and ii)** indicate that the variation of temperature with velocity interval follows the same trend for all positions. It generally decreases as the velocity relative to the line centre increases. Very near the  $^{13}\text{CO}$  emission peak the calculated temperature drops. This is an artifact due to self-absorption of  $^{12}\text{CO}$  gas.

We also provide a table (**Table III**) that includes all of the values of  $T_{\text{thick}}$ , since, in general,  $T_{\text{thick}}$  is more reliable than  $T_{\text{thin}}$ . In **Figure 15** we overlay all of the temperature versus velocity plots in one diagram, in order to display the range of the excitation temperatures values. The derived values for the excitation temperature vary between 5 and 60 K. The values of  $T_{\text{thin}}$  generally follow the extrapolated curve from the values of  $T_{\text{thick}}$  (see **Figure 14 i and ii**).

Error analysis indicates that the uncertainty in the excitation temperature obtained in the "optically thick" region,  $\Delta T_{\text{thick}}$ , is small (typically less than 5%). This may seem surprising since the temperature depends upon the optical depth, which has large uncertainties at high velocities (see **Figure 13**).  $T_{\text{thick}}$ , however, depends more strongly on radiation temperature than it does on optical depth. Thus, the error in the excitation temperature is not determined by the large uncertainties in the optical depth. The situation is quite different for  $T_{\text{thin}}$ . Here the errors due to the limited signal-to-noise ratio can be in excess of 100% (see **Figure 14 i and ii**), the tendency being that they increase as the signal becomes comparable to the noise in the spectrum.

TABLE III EXCITATION TEMPERATURES FOR THE 12 POSITIONS

$v$	$T_{ex}$ (K)											
km/s	1	2	3	4	5	6	7	8	9	10	11	12
1	6	26		6				7		13		
2	7	20		6	7			6	10	6	12	7
3	9	22	7	9	5		8	14	7	14	11	
4	11	24	9	17	6	13	13	22	11	19	20	10
5	14	29	16	25	7	20	24	30	19	25	36	20
6	19	33	24	31	12	25	38	29	31	29	39	27
7	40	32	25	34	16	23	29	26	38	28	36	38
8	44	28	23	34	17	23	39	25	41	26	39	38
9	45	32	30	38	22	32	58	33	40	32	47	41
10				37	28	27		36	39	36		36
11	30	25	24	19	26	18	18	23	18	26	19	17
12	39	51	32	39	19	24	37	21	21	21	24	15
13	44	39	41	45	28	20	54	40	32	35	34	22
14	41	48	41	40	41	17	45	56	27	54	35	22
15	34	33	33	35	33	14	36	49	28	50	30	
16	24	22	31	33	30	11	27	42	22	45	24	
17	14		30	47	30	11	22	39	23	41	20	
18	8	26			30			33	22		18	
19		23	51	31			26		17		19	
20		19	36	29			25		18		12	
21		14		23					20			
22				11					19			
23									16			

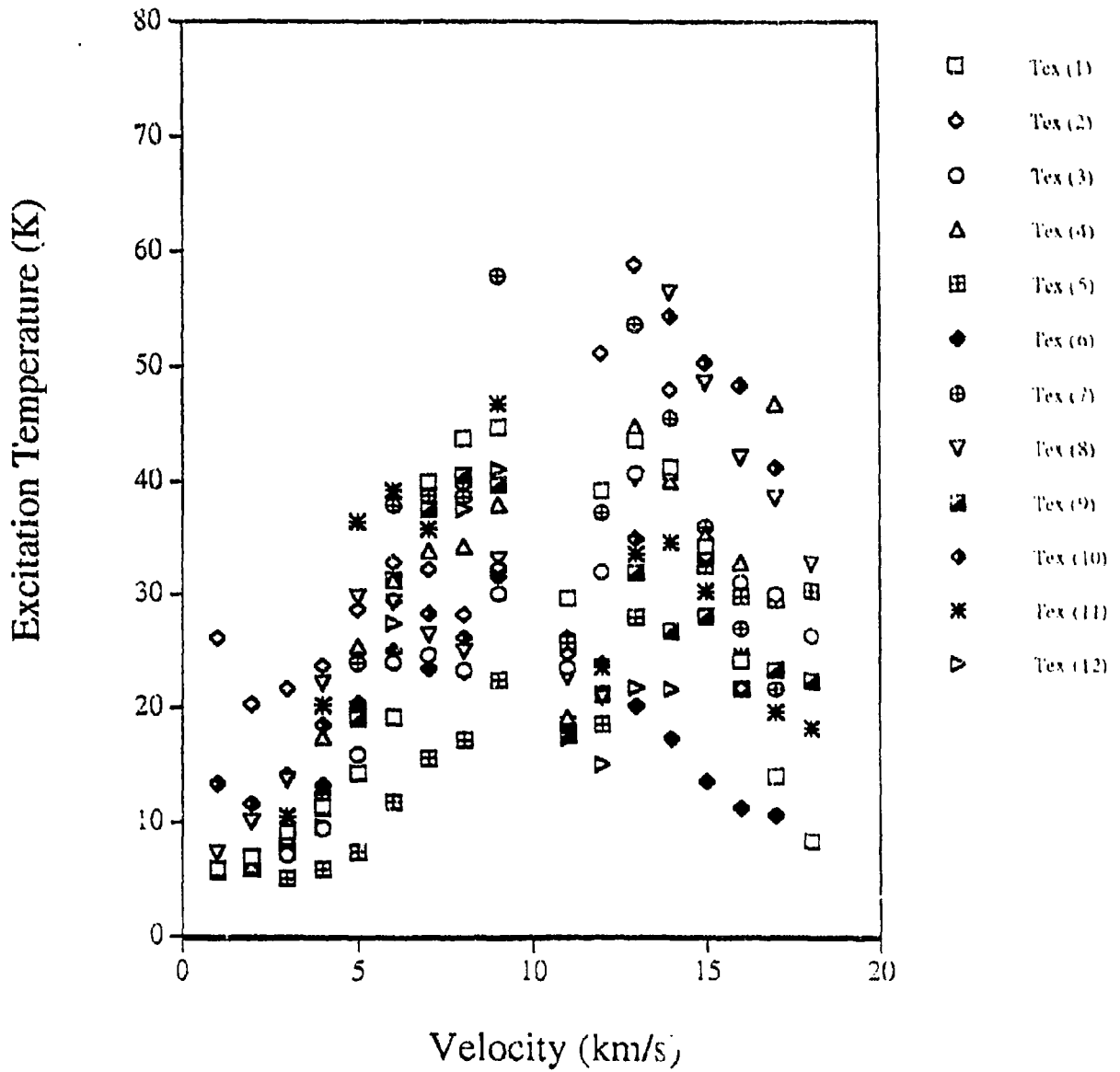


**Fig. 15** Excitation temperature,  $T_{ex}$ , versus velocity plots of all positions superimposed in one diagram. The excitation temperature varies between 5 K and 60 K. The numbers in parentheses indicated the position number.

We will examine in more detail the behaviour of the excitation temperature obtained from the two methods. It has already been pointed out that, overall, the temperatures obtained from the two methods are in very good agreement within their error bars. There are, however, two difficulties. One of the problems is that there are two positions (1 and 6) where  $T_{\text{thin}}$  does not agree with  $T_{\text{thick}}$  within the uncertainties. The second problem is the excitation temperature can have negative values. We are not concerned about this issue when the negative values can be explained by the limited signal-to-noise ratio, as is usually the case. The only exception is position at 4 (-10", 60"), where the negative values for the excitation temperature persist while the signal is not comparable to the noise (**Figure 16**).

The discrepancy seen at some velocities in position 1 and 6 can be explained by the fact that in our error analysis for the excitation temperature in the optically thin approximation we only take into account the error due to the stochastic noise in the antenna temperature. The fact that the approximation can be poor has been neglected. How does the value for the temperature change if the optical depth is larger than the optically thin approximation requires? Equation (5) indicates that there is a complicated dependence of excitation temperature with radiation temperature and optical depth. We calculate the temperature for the two positions of interest (namely 1 and 6) from equation (5) under the assumption that the lowest value of the optical depth is that from the optically thick region.

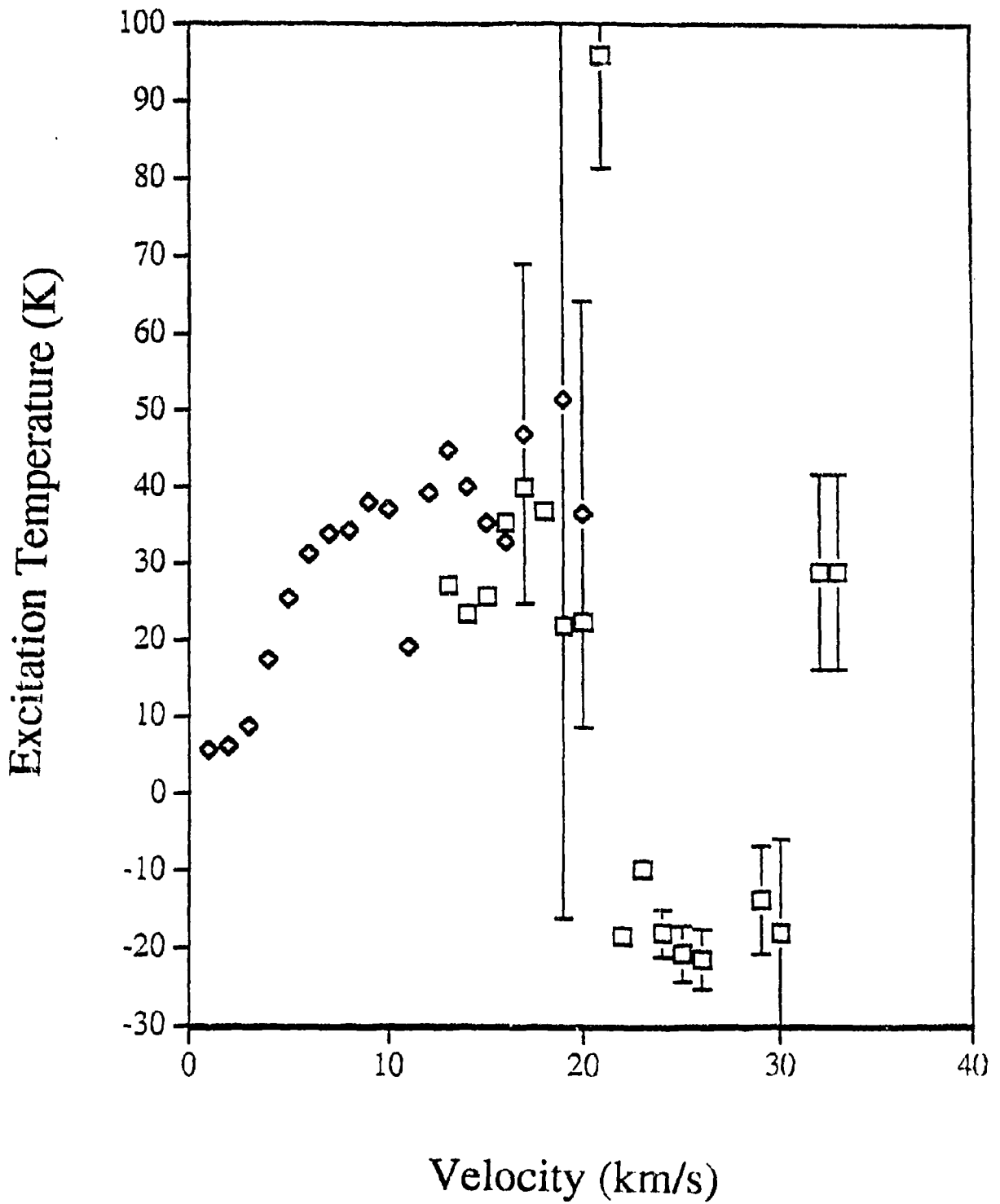


**Fig. 16** Excitation temperature from both methods at position 4 ( $-10''$ ,  $60''$ ). This is the only position where the excitation temperature has negative values that can not be explained by the limited signal-to-noise ratio.

The receding gas in the optically thin region at position 1 (10", 20") has an excitation temperature that is too high (**Figure 14 i**). In order to avoid the assumption that  $^{12}\text{CO}$  is optically thin, we recalculate the excitation temperature at  $v = 19$  km/s, using  $\tau^{12} = 6.3$  as found at  $v = 18$  km/s from equation (3). From equation (14) we find that the radiation temperature for  $v = 19$  km/s is 1.6 K. The new value of the excitation temperature obtained from the general expression (5) is  $T_{\text{new thin}}(v = 19 \text{ km/s}) = 6.8$  K and not  $T_{\text{thin}}(v = 19 \text{ km/s}) = 20.1$  K. The new value (6.8 K) is in much better agreement with the temperature calculated for  $v=18$  km/s from the optically thick region (8.4 K) than is the old  $T_{\text{thin}}$ .

Position 6 (-20", -10") has approaching gas at 2 km/s and 3 km/s in the optically thin domain with temperatures that are not in agreement with  $T_{\text{thick}}$  at  $v = 5$  km/s (see **Figure 14 i**). The excitation temperature  $T_{\text{thin}}$  at the velocities in question (2 and 3 km/s) is calculated by assuming that the gas is optically thin. If the optical depth for 3 km/s is assumed to be equal to the optical depth found at 4 km/s (i.e.  $\tau_v = 5$ ), then the new value of the excitation temperature is  $T_{\text{new thin}}(3 \text{ km/s}) = 6$  K, and not  $T_{\text{thin}}(3 \text{ km/s}) = 96$  K, as determined from the optically thin approximation. The new value agrees quite well with the value from the optically thick limit, since  $T_{\text{new thin}} < T_{\text{thick}}(4 \text{ km/s}) = 13$  K. We have just shown that the two cases of discrepancy between the excitation temperature derived from the two different methods can be explained if the optically thin approximation is not accurate.

Finally, the other problematic position is 4 (-10", 60"), because some of the receding velocities correspond to negative excitation temperatures (**Figure 16**) that cannot be explained by the limited signal-to-noise ratio (they do not

appear in **Figure 14 i**). This problem can be explained when we consider that the filling factor for the  $^{12}\text{CO } J=2 \rightarrow 1$  transition is at most  $(15/21)^2$  if the angular size of the source is equal to or less than  $15''$  (the beam width for this transition is  $21''$ ). We find that in all cases where the ratio of radiation temperatures is larger than the theoretical limit  $(9/4)$  imposed by equation (16), the filling factor consideration is adequate to explain the discrepancy. Therefore, this is an indication that clump 6 (at position 4) is at most  $0.06$  pc across.

### c. Column density of CO versus velocity

The column density can be found in the "optically thick" region from equation (10) and in the "optically thin" region from equation (18). For our  $^{12}\text{CO } J=3 \rightarrow 2$ ,  $J=2 \rightarrow 1$  and  $^{13}\text{CO } J=3 \rightarrow 2$  observations we use equations (11) and (19). In **Figure 17 (i and ii)** we present the computed column density and its error versus velocity from both methods; wherever a bar does not appear, the corresponding error is smaller than the symbol that represents the point. The CO column density (calculated for all rotational states) are noted as  $N_{\text{thick}}$  and  $N_{\text{thin}}$ , respectively. The term total column density will be used later for the sum of column densities over the entire velocity range. It is important to emphasize that the  $N_{\text{thick}}$  values are more reliable than the  $N_{\text{thin}}$ , since the former are based on known values of the optical depth.

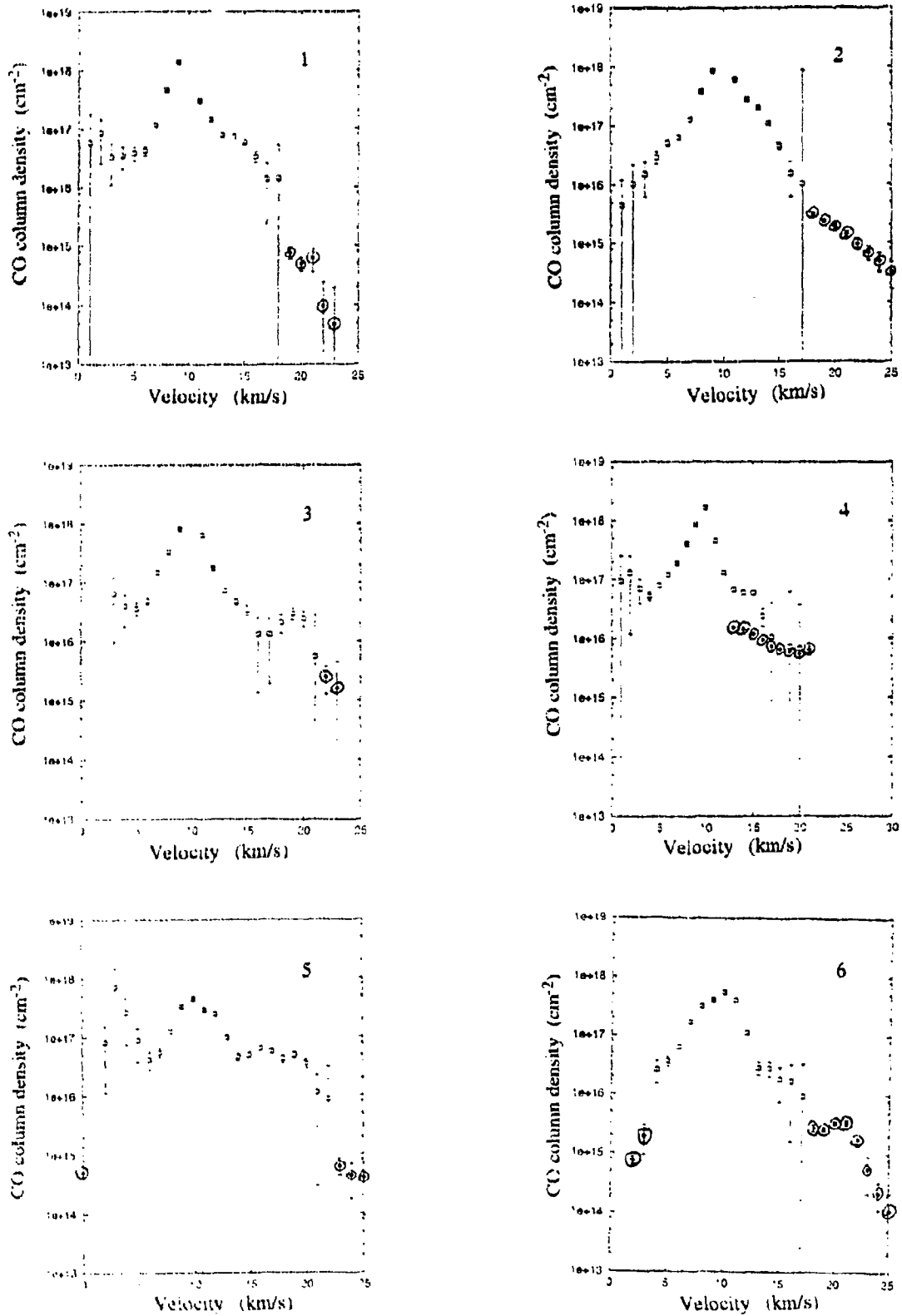


**Fig. 17 i** The column density from both methods,  $N_{\text{thick}}$  ( $\square$ ) and  $N_{\text{thin}}$  ( $\odot$ ) versus velocity for positions 1 to 6. The position number is indicated within each diagram. Whenever the error bar does not appear, it is smaller than the symbol that represents the point. For transitional velocities between the optically thin and the optically thick region, the calculated column densities from both methods agree within their error bars.

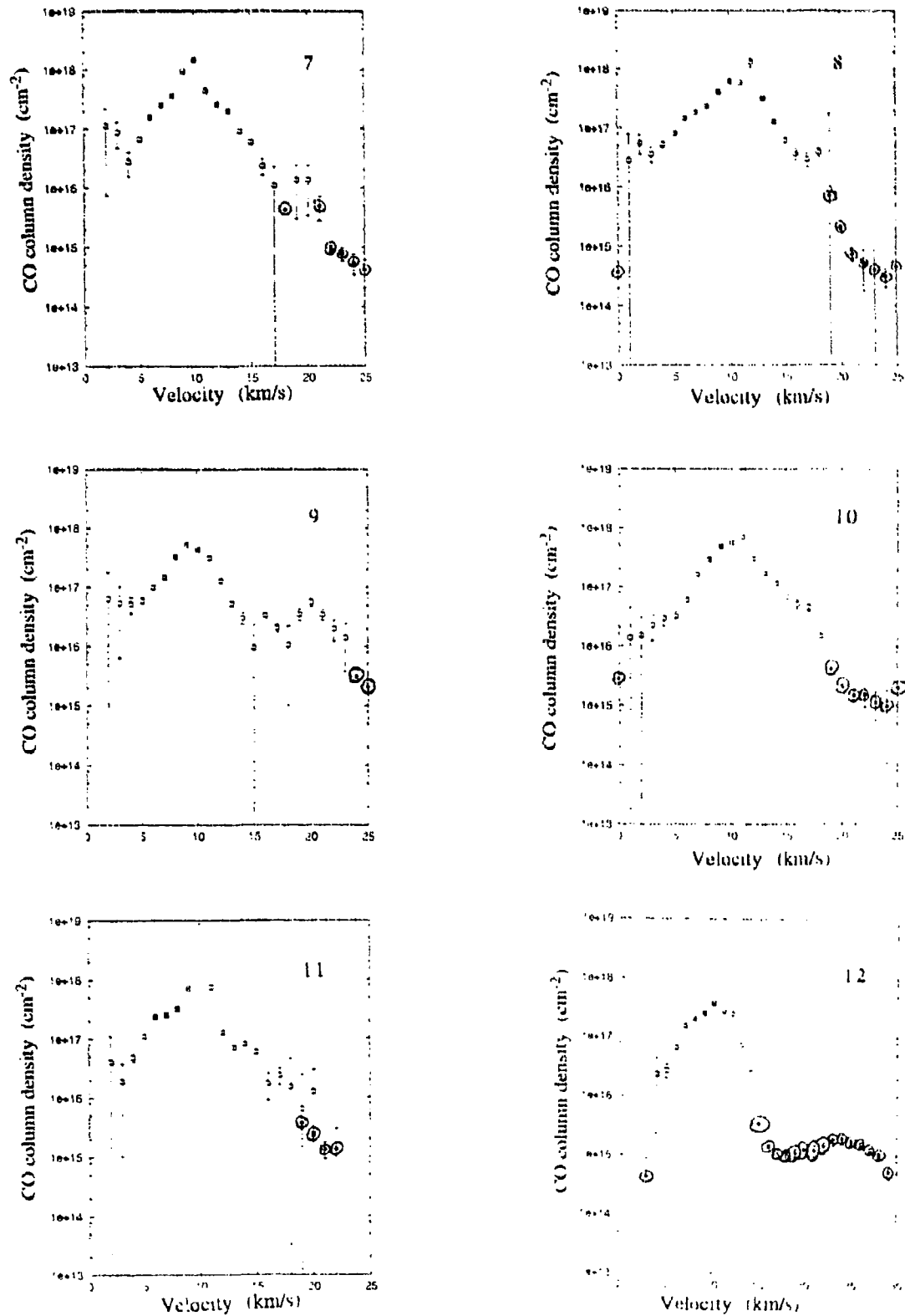


**Fig. 17 ii** The column density from both methods,  $N_{\text{thick}}$  ( $\square$ ) and  $N_{\text{thin}}$  ( $\odot$ ) versus velocity for positions 7 to 12. The position number is indicated within each diagram. Whenever the error bar does not appear, it is smaller than the symbol that represents the point. For transitional velocities between the optically thin and the optically thick region, the calculated column densities from both methods agree within their error bars.

The values of the CO column density have a large range for various velocities. They span from  $10^{16} \text{ cm}^{-2}$  to over  $10^{18} \text{ cm}^{-2}$  in the "optically thick" region and they cover from less than  $10^{14} \text{ cm}^{-2}$  up to  $10^{16} \text{ cm}^{-2}$  in the "optically thin". Although the values of  $T_{\text{thick}}$  have very small uncertainties,  $N_{\text{thick}}$  can have large errors, due to its dependence on optical depth. **Figure 18** illustrates this quite clearly for position 1 ( $10'', 20''$ ). The CO column density and the optical depth errors behave similarly; so much so that the two sets of data points are almost indistinguishable. After performing rigorous error analysis, we find that the errors associated with  $N_{\text{thin}}$  are large; they often exceed 100%, as is evident from **Figure 17**. It should be emphasized that where the relative errors for the column density are large, the values of the CO column densities are small (typically two orders of magnitude smaller than the maximum value) and therefore, these errors are not a major concern.

The agreement between the value of the CO column density derived from the two different methods in the vast majority of cases is excellent (**Figure 17**). There are a few cases, however, where  $N_{\text{thin}}$  is smaller than an extrapolation of  $N_{\text{thick}}$  values would suggest. An extreme example is the situation at position ( $0'', 0''$ ):  $N_{\text{thick}}$  evaluated at 17 km/s is  $1.0 \times 10^{16} \text{ cm}^{-2}$  and  $N_{\text{thin}}$  at 17 km/s is  $1.9 \times 10^{14} \text{ cm}^{-2}$ . This difference, however, is actually within the large uncertainty of the column density for  $N_{\text{thick}}$  ( $v=17 \text{ km/s}$ ), which is due to the low signal to noise ratio.

Although the column density in the optically thick limit depends on the filling factor, it does not in the optically thin limit (equation 1), if we assume that the filling factor is the same for both transitions  $J=3 \rightarrow 2$  and  $2 \rightarrow 1$ .

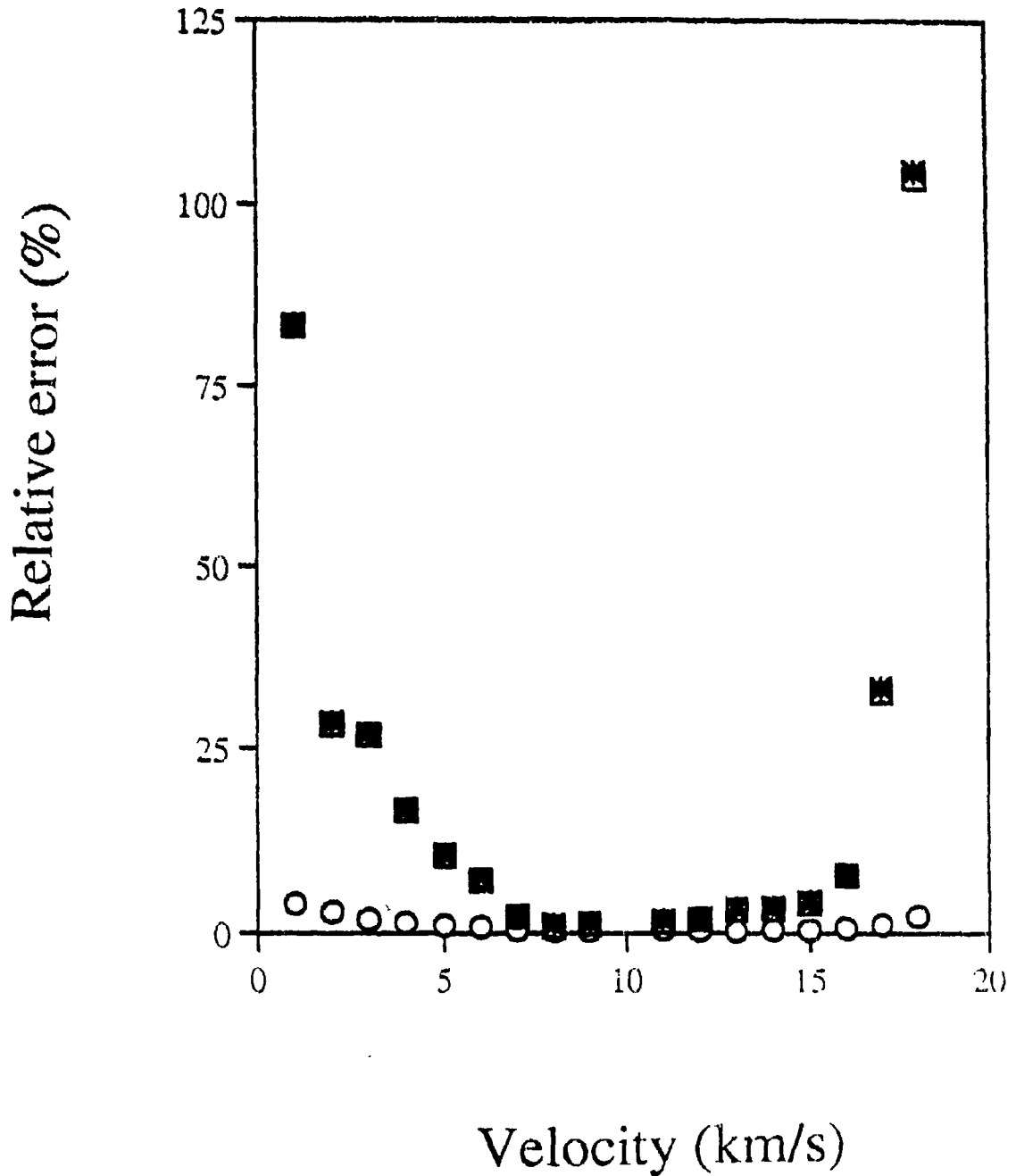


**Fig. 18** Variation with velocity of the errors (%) in the column density of  $^{12}\text{CO}$  (\*), the optical depth (□) and the excitation temperature (○), respectively, for position 1 (10",20"). The  $^{12}\text{CO}$  column density and the optical depth errors behave so similarly that the two sets of data points are almost indistinguishable.

The fact that in most cases the column densities from the two methods are in good agreement indicates that the assumption that the filling factor is one is fairly accurate.

If we exclude cases like this, where the discrepancy is ultimately caused by the limited signal-to-noise ratio, there is only one isolated case where  $N_{\text{thin}}$  does not agree with  $N_{\text{thick}}$  within their error bars. For position 6 (-20", -10") we obtain  $N_{\text{thin}}(3 \text{ km/s}) = (2.0 \pm 0.6) \times 10^{15} \text{ cm}^{-2}$  and  $N_{\text{thick}}(4 \text{ km/s}) = (26.6 \pm 4.5) \times 10^{15} \text{ cm}^{-2}$ . In order to explain this inconsistency, we consider the dependency of the column density on the excitation temperature.  $N_{\text{thin}}$  depends on the factor  $T_{\text{ex}} \exp(33.18/T_{\text{ex}})$  [see equation (19)]. Based on the graph of this quantity versus excitation temperature (Figure 19), we find that this factor is almost constant for temperatures between 20 and 100 K, but that it dramatically increases with decreasing temperature when  $T_{\text{ex}} < 20 \text{ K}$ . For example, the difference between the two terms calculated for 5 and 10 K is more than an order of magnitude. We have already demonstrated, however, that for  $v = 3 \text{ km/s}$  at position 6, the value of the excitation temperature is 6.4 K (instead of 96.2 K), when the optically thin approximation is relaxed. The ratio of the term evaluated for the two different temperatures is 11, which means that  $N_{\text{thin}}(3 \text{ km/s})$  is  $(2.2 \pm 0.7) \times 10^{16} \text{ cm}^{-2}$ , if we take into account that the gas is not optically thin. The value of  $N_{\text{thick}}$  is  $(2.7 \pm 0.5) \times 10^{16} \text{ cm}^{-2}$ , which is in good agreement with  $N_{\text{thin}}$ . Therefore, we have shown that the discrepancy between  $N_{\text{thin}}$  and  $N_{\text{thick}}$  for position 6 (-20", -10") can be removed, when the optical thin approximation is relaxed.

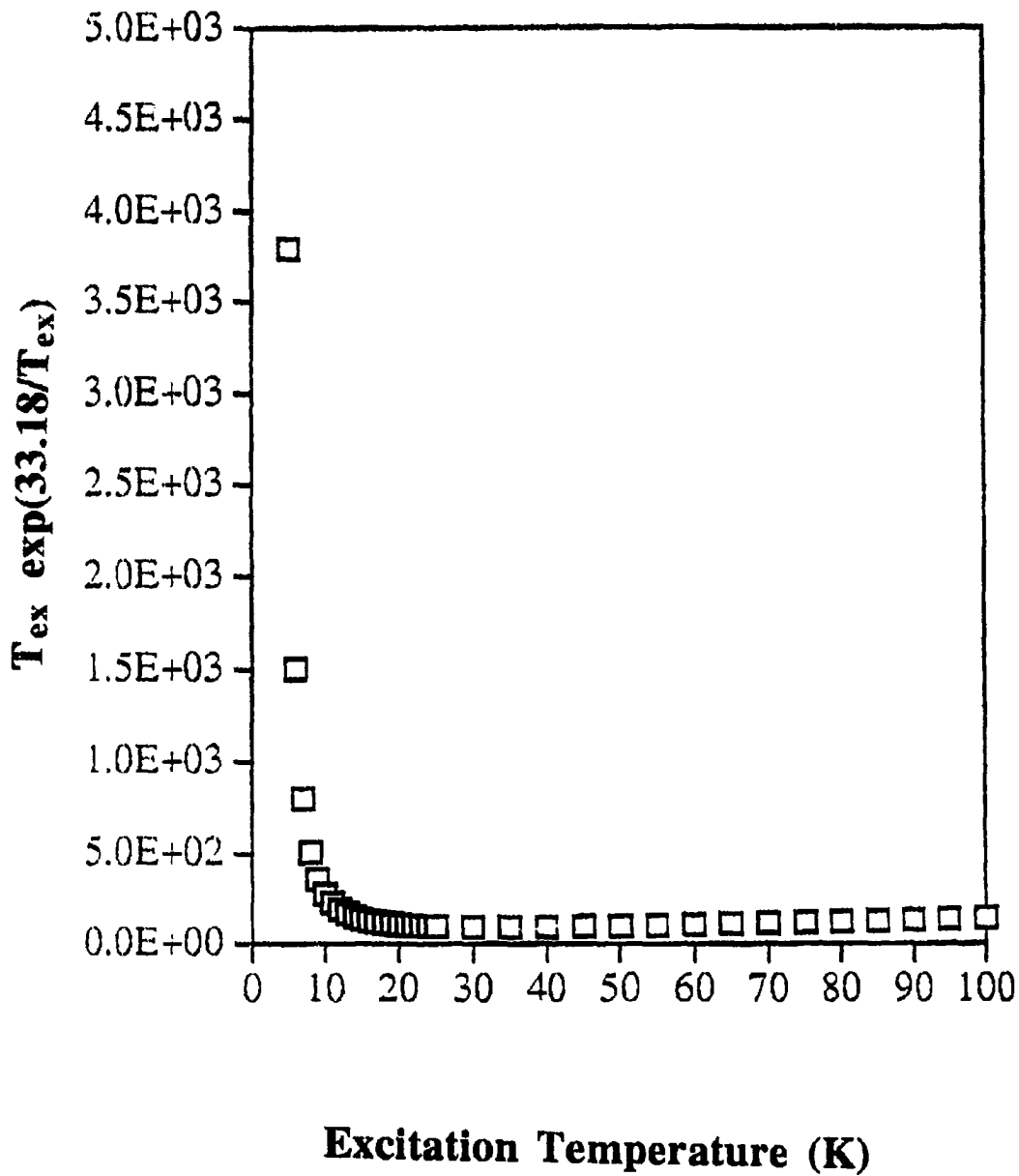


**Fig. 19**  $T_{ex} \exp(33.18/T_{ex})$ —which is directly proportional to  $N_{thin}$ —versus excitation temperature. This demonstrates that  $N_{thin}$  is almost constant for temperatures between 20 and 100 K, but is very sensitive to changes in the excitation temperature when  $T_{ex} < 20$  K.

From the previous discussion we conclude that the CO column density obtained by using  $^{12}\text{CO}$  and  $^{13}\text{CO}$   $J=3\rightarrow 2$  observations is in excellent agreement with the column density obtained by using  $^{12}\text{CO}$   $J=3\rightarrow 2$  and  $J=2\rightarrow 1$  observations in the transition regions. The few difficulties that arise can be explained by stochastic errors and by the fact that our assumption of optical "thinness" in the second method is not always appropriate.

As we have mentioned in the beginning of this section, we calculated  $N_{\text{thin}}$  from equation (19) for  $^{12}\text{CO}$   $J=3\rightarrow 2$ . The CO column density for the optically thin region must not be different if we calculated  $N_{\text{thin}}$  from equation (20) for  $^{12}\text{CO}$   $J=2\rightarrow 1$ . As an example, at the position  $1(10'', 20'')$ , the two values agree to within 5%.

#### d. Mass and other properties of the high-velocity clumps

It has been shown in Chapter IV that, in order to calculate the mass of the clumps, it is necessary to determine the size and the total column density for the velocity range of each clump. Since the shapes of the clumps change continuously with velocity interval, we assume that they are spheres with a diameter of  $15''$ . This hypothesis is fair, since most clumps have dimensions between  $10''$  and  $20''$ , although it is possible that some clumps may not be resolved.

Obtaining reliable total column densities is complicated by the fact that some of the clumps have both receding and approaching gas, and that most are not visible between 6.5 km/s and 12 km/s. We believe that those clumps which are seen on maps of both receding and approaching gas are present in the intermediate velocities as well. This is based on the following observations: two main absorption features occur on average at  $(7.6 \pm 0.5)$  km/s and  $(11.3 \pm 1.0)$  km/s. Thus, between 7.1 km/s and 8.1 km/s, as well as 10.3 km/s and 12.3 km/s, the intensity is not a very accurate measure of column density. For the intervening velocity range, namely between 8.1 km/s and 10.3 km/s, the features are not seen readily, probably due to the presence of smoothly distributed gas in that velocity range. This quiescent gas prevents the clumps from appearing distinctly in the maps. Another argument to justify our conclusion that the clumps have gas with a continuous range of velocities is that the velocity structure implied otherwise would be very strange. However, since the previous discussion is not proof that the clumps have velocities that include the line centre, two approaches are used to calculate the total column density of each clump.

Using the first approach, we calculate the total column density based on the hypothesis that the velocity range of the clump includes the centre of the line. With this method, we have to assume some value for the column density near 10.3 km/s in positions 1, 2, 3, 9 and 11, where the column density cannot be found directly because of absorption. There is no quantitative way to treat this problem, so simple reasoning is followed. Five positions have column densities calculated at  $v = 10$  km/s. Three of them have their highest measured column density for  $v = 10$  km/s; the other two positions have their highest measured column density at  $v = 9$  km/s and 12 km/s. Therefore, we

adopt the highest value for the column density among the values calculated for 9 km/s and 12 km/s as the value of the column density for  $v = 10$  km/s. For all other velocities we use the calculated values of the column density.

The second approach consists of calculating the total column density and the mass based exclusively on the velocity range where the clump is clearly seen. If we compare the two results we can investigate the importance of the mass near the centre of the line (10.3 km/s). To summarize: the total column density is calculated by assuming the clumps are present throughout the line, wherever they are seen in the maps of both receding and approaching gas; it is also deduced by omitting the velocity intervals where the clumps are not seen.

Our results are presented in **Table IV**. This table includes the running number of the clump, its receding mass, its approaching mass, the sum of the receding and approaching mass (i.e. the results from the second approach), and finally, the total mass for the whole clump including the line centre (i.e. the results from the first approach). In most cases where there is approaching and receding gas, the approaching gas is approximately two times more massive. Furthermore, the overall average mass of the gas that is approaching is larger than that of the receding gas.

We compare the masses of the clumps seen in the Mon R2 core with other clumpy outflow sources. The clumps in GL 490 discussed by Mitchell et al. (1993) have masses between 0.5 and  $0.01 M_{\odot}$ . These values are large compared to the masses of clumps in other outflow sources, for example: clumps in L1448 IRS 3 have a few  $\times 10^{-3} M_{\odot}$  (Bachiller et al. 1990), IRAS

TABLE IVMASSES OF THE CO CLUMPS ( $M_{\odot}$ )

Clump #	Mass of approaching gas	Mass of receding gas	Combined mass of receding and approaching gas	Total mass of clump (including centre)
1	0.19	0.81	1.00	2.34
2	0.78	0.35	1.13	2.73
3	0.56	0.31	0.87	2.37
4	1.66	0	1.66	1.66
5	0.43	0.14	0.57	2.31
6	1.20	0.44	1.64	2.51
7	0.08	0	0.08	0.08
8	0.85	0	0.85	0.85
9	0.18	0	0.18	0.18
10	0	0.17	0.17	0.17
11	0	0.09	0.09	0.09
12	0	0.12	0.12	0.12
13	0	0.007	0.007	0.007

03282+3035 has clumps with a few  $\times 10^{-4} M_{\odot}$  (Bachiller et al. 1991), and clumps in  $\rho$  Oph A have masses equal to  $\approx 10^{-3} M_{\odot}$  (André et al. 1990). Comparing the previous masses with the values we deduced for Mon R2, it is clear that all the clumps in Mon R2 (with one exception) are more massive than clumps in other clumpy outflows.

We can estimate the fraction of the total mass in the line of sight that is included in each clump by dividing the clump mass (from the last column of **Table V**) by the total mass (integrating overall detected velocities). The average value of this ratio is  $(27 \pm 22)\%$ . It should be noted that there is a large scatter in this mean value. For clumps that have only approaching or receding gas, the ratio is generally below 10% (the only exception is clump 5, with a ratio of 25%). Clumps, however, that are present in both maps, even if the central part is ignored, represent 35% to 65% of the total mass. From these results, it is fair to say that the masses of the clumps are not negligible in comparison with the mass associated with the centre of the line. We must emphasize, though, that these percentages are upper limits, since the total column density is actually higher than is implied by our CO observations due to self-absorption in CO. We will investigate this in more detail in the next Chapter.

In order to find the number density of molecular hydrogen in each clump we use that the diameter of each clump is approximately 0.06 pc and  $^{12}\text{CO}/\text{H}_2 = 10^4$ . The molecular hydrogen densities calculated with these assumptions are summarized in **Table V**. From this table we conclude that the typical value of the number density obtained from our data is between  $10^4$  and  $10^5$  hydrogen molecules  $\text{cm}^{-3}$ . It is possible that these are upper limits,

TABLE V

## MOLECULAR HYDROGEN NUMBER DENSITY OF THE CO CLUMPS

Clump Number	n(H <sub>2</sub> ) from first approach (through the centre) (Number of H <sub>2</sub> per cm <sup>3</sup> )	n(H <sub>2</sub> ) from second approach (sum of red and blue) (Number of H <sub>2</sub> per cm <sup>3</sup> )
1	2.9 e5	1.3 e5
2	3.4 e5	1.4 e5
3	3.0 e5	1.1 e5
4	2.1 e5	2.1 e5
5	2.9 e5	7.1 e4
6	3.2 e5	2.1 e5
7	9.4 e3	9.4 e3
8	1.1 e5	1.1 e5
9	2.2 e4	2.2 e4
10	2.2 e4	2.2 e4
11	1.2 e4	1.2 e4
12	1.4 e4	1.4 e4
13	9.2 e2	9.2 e2

since in the beam there may be some contribution to the column density from gas along the line of sight. If, for example, the column density originates from material that extends in the line-of-sight 8 times the clump's assumed diameter, then the molecular hydrogen density is overestimated by an order of magnitude. We do not expect this to be an important effect, however, because there is evidence that the clumps are centrally condensed and that the contribution of gas that is far from the centre of the clump is not very significant.

Note that the values from the two approaches we used to calculate the mass of the clumps differ at most by a factor of three. However, the value for the mass of the combined receding and approaching gas should be considered a lower limit, since there is a considerable amount of mass with velocity around 10.3 km/s. This is evident from the high overall intensity of the  $^{12}\text{CO}$  gas at that velocity. Therefore, we conclude that the values for the density which result from the approach that includes the line core are more appropriate. The alternate approach will not be considered any further.

The spatial distribution of the clumps is presented in **Figure 20**. The larger square box is used for the clumps that have both approaching and receding gas, because they are usually more massive. The figure indicates that the various clumps do not exhibit any obvious symmetry or bipolarity, which may suggest that the clumps are not involved in a systematic movement as a whole, but that they have their own independent directions. More about the kinematics of the clumps will be discussed in the following subsection.

---

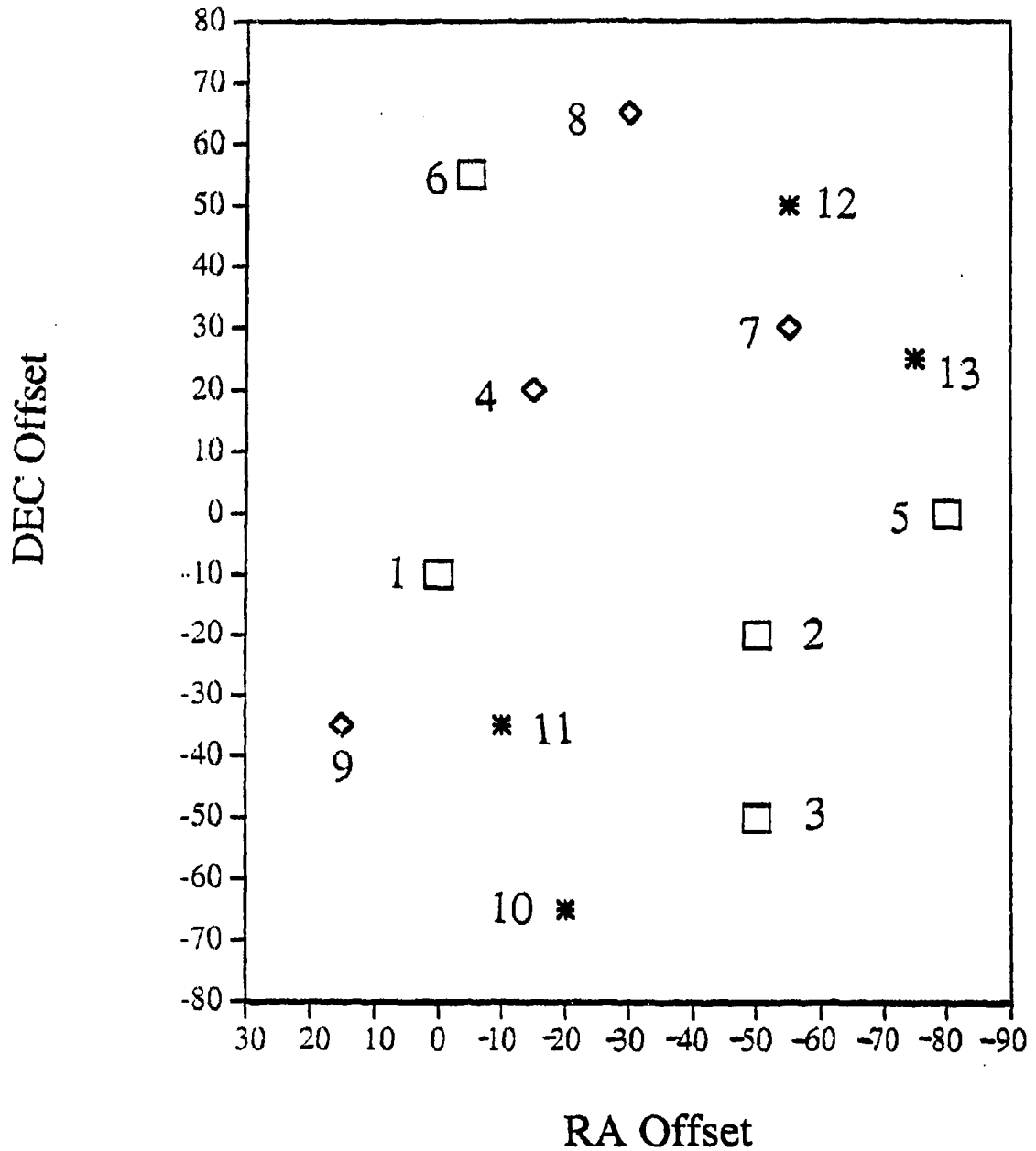


**Fig. 20** Spatial distribution of the clumps on a RA-DEC map. RA and DEC increase to the left and the north respectively. The square box (□) is used for the clumps that have both blue and red-shifted gas, which are usually more massive. The clumps with only blue (◇) and only red-shifted gas (\*) have usually smaller masses. The CO clump distribution does not show any obvious pattern or bipolarity.

### e. Energetics of the clumps and implications for the cloud core

Since the mass of each clump has been determined, it is possible to examine their energetics in some detail. We can easily calculate the total kinetic energy of each clump relative to the cloud core velocity,  $E_{k\ tot}$ , by integrating over the appropriate velocity range. For this purpose, we must take into account that the observed radial velocities include the motion of the cloud in the line of sight. Therefore, we subtract from the observed velocity the radial velocity of the cloud core,  $v_0$ , namely 10.3 km/s. The total kinetic energy is given by the following expression:

$$E_{k\ tot} = \frac{1}{2} \sum_j m_j \cdot (v_j - v_0)^2, \quad (21)$$

where  $m_j$  are the masses at the various velocities  $v_j$ , and  $v_j$  are the observed LSR velocities.

The total kinetic energy of each clump has two components, which are due to two different types of motion: the bulk motion of a clump as a separate entity, and the internal motion of the gas within the clump. Clearly, it is not possible to determine the three dimensional direction of the bulk motion of a clump, since only radial velocities are available. With this limitation in mind, we define the bulk velocity of each clump as its mass-weighted average

radial velocity or, equivalently, as the total linear momentum of the clump over its mass:

$$V_b = \frac{P_{clump}}{M_{clump}} = \frac{\sum_j m_j(v_j) \cdot (v_j - v_o)}{\sum_j m_j(v_j)} \quad (22)$$

where  $v_j$  are the observed LSR velocities and  $v_o$  is the radial velocity of the cloud (10.3 km/s). By making use of the calculated mass for each clump,  $M_{clump}$ , it is straightforward to compute the bulk kinetic energy:

$$E_{k-b} = \frac{1}{2} M_{clump} \cdot V_b^2 \quad (23)$$

The internal motion of the gas within the clump is defined with respect to the standard of rest of each clump. Therefore, in order to calculate the internal velocity of the gas, the velocity of the cloud and the bulk velocity of the clump are subtracted from the observed velocities  $v_j$  of each clump. Thus, the internal kinetic energy of each clump,  $E_{k-in}$ , is calculated by summing over all internal velocities according to the following equation:

$$E_{k-in} = \sum_j \left\{ \frac{1}{2} m_j(v_j) \cdot [(v_j - v_o - V_b)^2] \right\} \quad (24)$$

Our results are presented in **Table VI**. They include for each clump the mass  $M$  (in  $M_\odot$ ), bulk velocity  $V_b$  (km/s), total kinetic energy  $E_{k-tot}$  (erg), bulk kinetic energy  $E_{k-in}$  (erg) and, finally, the gravitational binding energy  $E_{grav}$  (erg), which we will discuss in more detail. It is encouraging that the sum of the two types of kinetic energy is equal to the total kinetic energy (within 5%), because it indicates that our calculations are self-consistent.

TABLE VI  
ENERGETICS OF CLUMPS

Clump	Mass M ( $M_{\odot}$ )	$V_b$ (km/s)	$E_{k-tot}$ (erg)	$E_{k-b}$ (erg)	$E_{k-in}$ (erg)	$E_{grav}$ (erg)
1	2.3	-0.39	1.1 e44	3.5 e42	1.0 e44	9.4 e42
2	2.7	0.05	1.9 e44	6.8 e40	1.9 e44	1.3 e43
3	2.4	-0.62	2.1 e44	9.1 e42	2.0 e44	9.6 e42
4	1.7	-2.78	2.0 e44	1.3 e44	7.7 e43	4.7 e42
5	2.3	-0.76	1.6 e44	1.3 e43	1.4 e44	9.2 e42
6	2.5	-0.63	1.7 e44	1.0 e43	1.6 e44	1.1 e43
7	0.08	-4.94	1.8 e43	1.8 e43	4.9 e41	9.7 e39
8	0.85	-2.94	1.1 e44	7.4 e43	3.5 e43	1.3 e42
9	0.18	-4.17	3.3 e43	3.1 e43	2.2 e42	5.3 e40
10	0.17	7.72	1.1 e44	1.0 e44	4.9 e42	5.1 e40
11	0.09	7.51	5.7 e43	5.3 e43	4.0 e42	1.5 e40
12	0.12	10.25	1.2 e44	1.2 e44	3.0 e42	2.3 e40
13	0.007	14.62	1.6 e43	1.6 e43	3.0 e41	9.2 e37

From Table VI it is evident that the bulk velocity of the clumps,  $V_b$ , is usually much less than the internal dispersion of the gas within each clump (see columns 3 and 4 in Table II). The reason for this difference (a few km/s versus a few tens of a km/s) is not understood.

We have discussed only the kinetic energy of the clumps. It is interesting to address the question of whether or not the clumps are gravitationally bound. Therefore, we compare the internal kinetic energy with the gravitational energy of each clump,  $E_{grav}$ , which is given by the following formula in the approximation of constant density:

$$E_{grav} = -\frac{3}{5} \frac{GM^2}{R} \quad (25)$$

where  $G$  is the gravitational constant,  $M$  and  $R$  are the mass and the radius of the clump, respectively. The value of the gravitational energy of each clump is given in Table VI. From this table, we find that the internal kinetic energy is larger than the gravitational energy by at least one order of magnitude. Therefore, it is clear that the clumps are not gravitationally bound. However, this does not preclude the possibility that the clumps are confined by other mechanisms. For example, ram pressure caused by a fast neutral wind could, in principle, confine a clump (Garden et al. 1991). We will not pursue this argument further because, presently, there is no evidence of a directed wind.

We calculate the mean lifetime of a clump against dissipation due to expansion. The speed of sound is the velocity with which a disturbance will propagate. If we assume that the density  $\rho_0$  and the pressure  $P_0$  are constant throughout the clump then the isothermal sound speed,  $v_s$ , is given by

$$v_s^2 = \frac{P}{\rho_0}. \quad (26)$$

Torrelles et al. (1990) find that the gas temperature is between 30 and 45 K, so we assume that the temperature is on average 38 K. Using these results, we calculate the speed of sound to be  $v_s = 0.3$  km/s. Thus, the time for a pressure wave to move through a 0.06 pc diameter clump is approximately  $2 \times 10^5$  years. This time,  $2 \times 10^5$  years, is a measure of the lifetime of the clumps in the absence of any external confining pressure.

In general the bulk velocities are underestimated, because the direction of the motion of the clumps in space is unknown, as we have mentioned before. Therefore, if the clump is moving along the line of sight, the velocity we obtain is equal to its true velocity, but if the clump is moving close to the plane of the sky, then the radial velocity we obtain is a small fraction of velocity of the clump. We assume that on average the space velocities will be  $1.4, (\sin 45^\circ)^{-1}$ , times larger than the calculated values.

Finally, we investigate the possibility that the cloud core is dissipating due to the kinetic energy of these clumps. We must assume that the positions we have analyzed in detail are representative. The total kinetic energy must be scaled up, in order to estimate the total internal kinetic energy of the cloud core. Our calculations indicate that the CO clumps occupy 20% of the mapped area, which is approximately a circle of 1' radius. We find that the total internal kinetic energy of the cloud core is  $7.4 \times 10^{45}$  erg. If we consider that the bulk velocities have been underestimated by a factor of 1.4 on average, then the total kinetic energy is  $\approx 1.5 \times 10^{46}$  erg.

The binding energy of the cloud core is calculated using Henning et al.'s (1992) estimate of the mass,  $200 M_{\odot}$ , for a radius of  $1'$  ( $0.24$  pc). Thus, equation (25) yields that the gravitational energy is  $9.2 \times 10^{45}$  ergs. From this crude calculation we find that the gravitational binding energy ( $9.2 \times 10^{45}$  erg) is somewhat smaller than the total kinetic energy ( $1.5 \times 10^{46}$  ergs), which suggests that the cloud core may be expanding.

Another consideration is the effect of the core's magnetic field. Knapp and Brown (1976) estimate that the strength of the magnetic field ranges between  $3 \mu\text{Gauss}$  to  $0.3 \text{ mGauss}$ ; this is based on a low resolution study ( $20'$  beam width, which is equivalent to  $10^{19}$  cm). However, the area that we are examining has a diameter of approximately  $10^{18}$  cm. According to Myers (1985) the expected magnetic field for such scales is on the order of one mGauss.

The magnetic energy density is given by the following formula:

$$E_M = \frac{B^2}{2\mu}, \quad (27)$$

where  $B$  is the strength of the magnetic field and  $\mu$  is the permeability of the material; here we assume that  $\mu = \mu_0 = 4\pi \times 10^{-7}$  H/m in SI units. If we assume that the magnetic field in the core with a radius of  $8 \times 10^{17}$  cm is  $B = 1$  mG, then the magnetic energy density is  $E_M = 3 \times 10^{45}$  erg. This value is almost an order of magnitude smaller than the gravitational binding energy. The sum of the magnetic and the gravitational energy ( $12 \times 10^{45}$  erg) is somewhat smaller than the total kinetic energy of the inner core of the Mon R2 cloud ( $15 \times 10^{45}$  ergs). The inequality suggests that the injection of kinetic energy into

the core gas by the star formation process (via winds, outflows, H II region expansion) may have initiated the disruption of the core. Since the difference is not large, we cannot exclude the possibility that the core is in dynamical equilibrium.

## VI. DISCUSSION

### a. Comparison of our CO map with other work

#### i) Comparison of a 2.2 $\mu\text{m}$ image with the CO clump distribution

Using IRCAM on UKIRT, Aspin and Walther (1990) obtained a 2.2  $\mu\text{m}$  image of the inner 90" x 90" core region of Mon R2. In **Figure 21** we have overlain it on the map of the CO clump distribution. Most of the clumps identified in the CO map, namely 5, 6, 7, 8, 12, 13, 9, and 10, are entirely (or mostly) outside the field of the image by Aspin and Walther. There is no CO peak within the shell of 15" radius centered on IRS2; this will be explained in more detail later. The pointing accuracy of the JCMT is 2" (Matthews, 1992), which is small compared to the size of the clumps.

Four CO clumps lie within the field of the 2.2  $\mu\text{m}$  image. Clump 1 coincides with IRS 3 and has approximately the same size. Clump 2 encompasses IRS 6. In the north, clump 4 includes the infrared sources a<sub>i</sub>, a<sub>ii</sub>, c and g. Finally, clump 11 is roughly centered on IRS 7.

In principle it is not possible from these observations alone to distinguish in each case if the correspondence of an infrared source to a CO clump is due to physical association or to spatial coincidence. Since there are 17 sources in the image, the probability for positional coincidence is high.

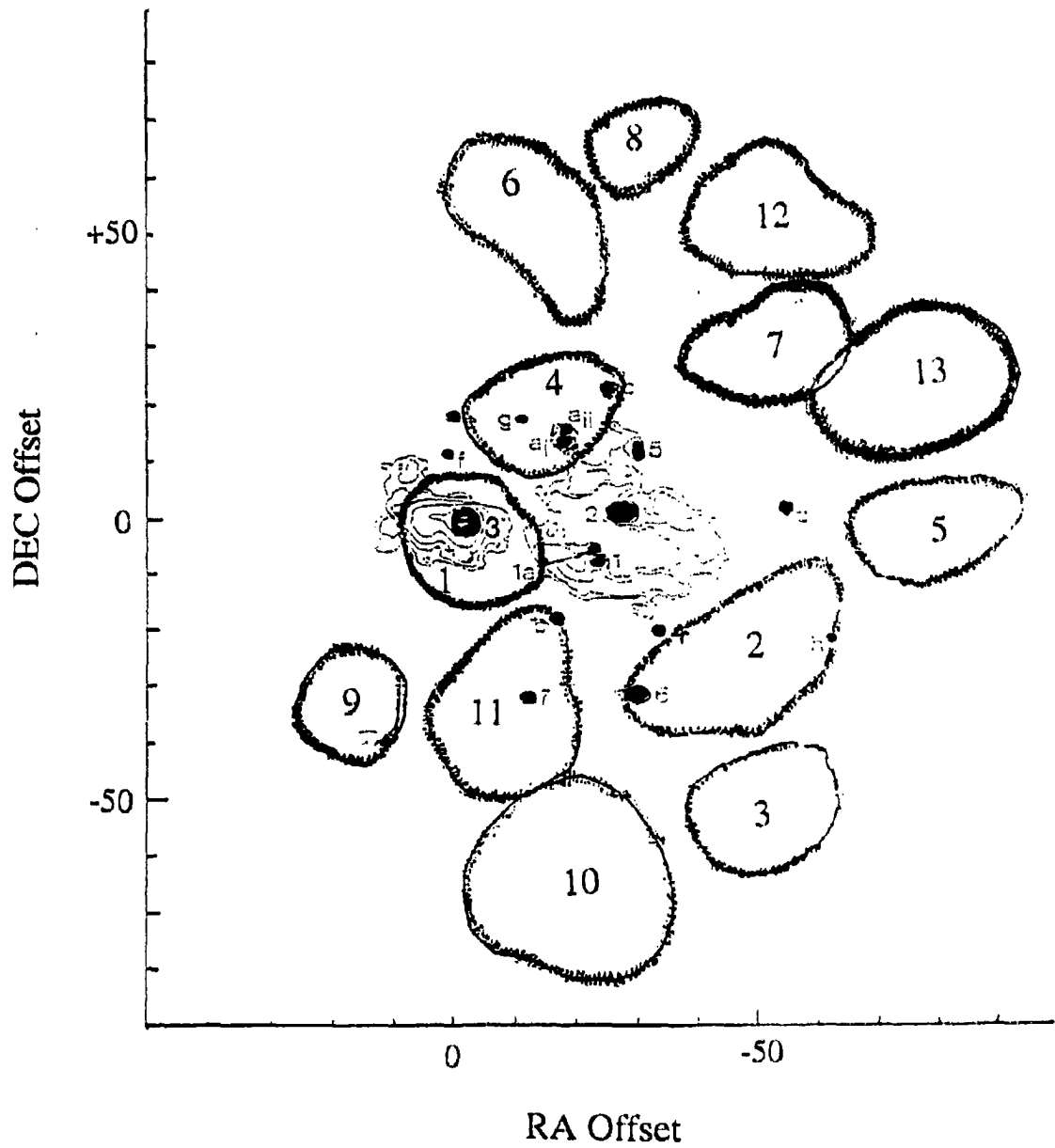


**Fig. 21** Our CO clump distribution is superimposed on Aspin and Walther's (1990) 2.2  $\mu\text{m}$  image of the inner 90'' x 90'' region of the Mon R2 core.

Also, the CO emission is a tracer of gas, while the 2.2  $\mu\text{m}$  image indicates the position of highly reddened objects or of scattered light due to dust. The geometry presented in **Figure 21** suggests, however, that IRS 7 and IRS 3 may be physically related to clumps 11 and 1, respectively. It has been noted that the CO clumps are in the process of dissipating; therefore they are not forming stars.

ii) The CO clump distribution compared with maps of other molecules

1) HCN

In **Figure 22** we present intensity maps of HCN  $J=4\rightarrow 3$  (354.5 GHz) emission. The HCN data were obtained at the JCMT in November 1992 by G. F. Mitchell and H. E. Matthews. The top left map is integrated intensity from all the approaching gas with velocities between 0 km/s and 10 km/s, and the top right map is integrated intensity from all the receding gas with velocities between 10 km/s and 20 km/s. The lower map in **Figure 22** is the integrated intensity for all the gas with observed velocities between 0 and 20 km/s. On this map we have superimposed the distribution of the CO clumps.

The approaching HCN gas shows two distinct structures: one in the east and one in the southwest. Within the east structure lies a southern concentration that has the highest intensity in the map (at the same position with CO clump 1). From this main peak extends an intensity enhancement towards the north (coincides with CO clumps 4 and 6). **Figure 22** indicates that an arc of emission links the east and the southwest intensity peaks.

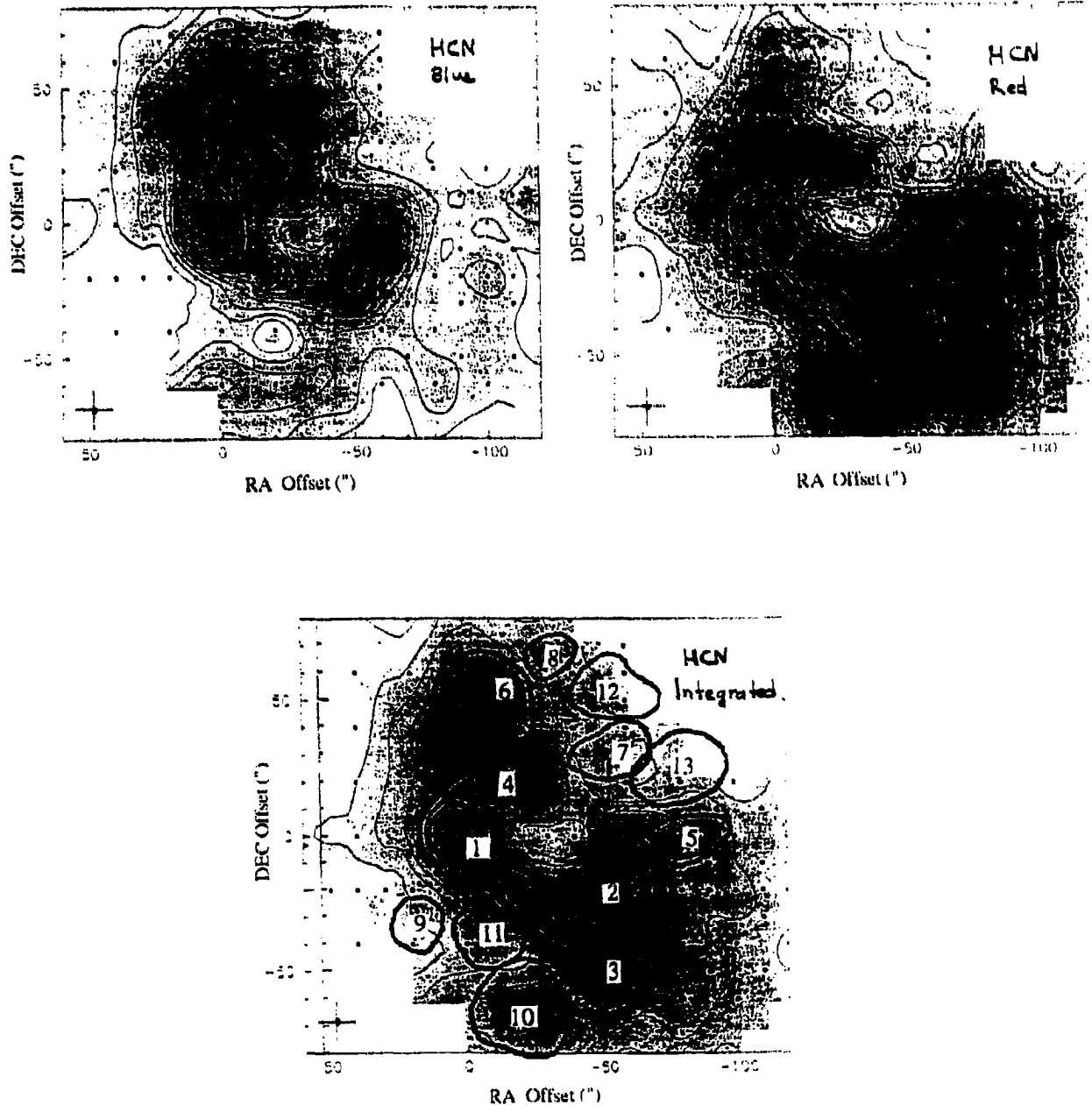


**Fig. 22** Integrated intensity maps of HCN  $J=4 \rightarrow 3$  (354.5 GHz) emission (15" beam). The top left map is integrated intensity for all approaching velocities (blue), i.e. between 0 km/s and 10 km/s. The top right map is integrated intensity for all receding (red) velocities between 10 km/s and 20 km/s. For both maps, the base level is 1 K km/s and the interval between contours is 1 K km/s. The lower map is the integrated intensity for all the observed velocities between 0 and 20 km/s. The integrated HCN contours have a base level at 2.50 K km/s and the interval between contours is 2.50 K km/s. On this map we have superimposed the distribution of our CO clumps.

The southwest feature has an oval shape and coincides with CO clump 2. Between the two intensity HCN emission peaks there is a minimum centered at (-30, -5). For the map of the receding gas the arc of emission just south of the intensity minimum becomes a prominent feature. The southern peak seen in the east structure is still clearly visible, but the northern extension is not very distinct. The arc encompasses the southwest feature.

The HCN emission, as seen in the integrated map, is distributed in an incomplete ring, in the center of which there is an intensity minimum. The strongest emission originates from the position of CO clump 1 (IRS 3). The large HCN feature on the southwest part of the arc coincides closely in position and shape with CO clump 2. Clumps 3, 4, 6 and 10 coincide with minor enhancements in the intensity of HCN emission. It should be noted that the HCN  $J=4 \rightarrow 3$  transition has a very high critical density ( $10^7 \text{ cm}^{-3}$ ) for excitation in the optically thin limit. HCN is unlikely to be optically thin, so the density of the gas probed is probably lower, perhaps closer to  $10^6 \text{ cm}^{-3}$ . The fact that the positions of CO clumps match fairly well with the location of HCN peaks is further evidence that the CO traces dense gas. Since the two molecules probe different densities, it is reasonable to conclude that the cloud core has an average density of  $\approx 10^5 \text{ cm}^{-3}$  (as indicated by our CO observations), but can exceed  $10^6 \text{ cm}^{-3}$  in the clumps.

It has already been mentioned that Richardson et al. (1988) mapped HCN in a  $3' \times 3'$  region centered on the core of Mon R2. The overall agreement with our HCN map is satisfactory considering that they used a lower transition ( $J=1 \rightarrow 0$ ) and their beam width was slightly larger (20" versus 15"). Both maps have two peaks with the same separation. However, our

map has higher resolution and the  $J=4\rightarrow 3$  transition has a much higher critical density. Also, the fact that emission from other molecules (especially  $\text{H}_2\text{CO}$ ) shows very similar structure to our HCN ( $J=4\rightarrow 3$ ) map gives us confidence in our results.

## 2) $\text{H}_2\text{CO}$

Figure 23 presents  $\text{H}_2\text{CO } J_{K_1, K_2} = 5_{1,5} \rightarrow 4_{1,4}$  (351.7 GHz) emission maps based on data obtained at the JCMT in November 1992. The beam width is again 15". In the upper left of the figure the integrated map for the approaching gas with velocities between 5.8 km/s and 10.3 km/s is presented; in the upper right the integrated map gas with velocities between 10.3 km/s and 15.3 km/s appears. The morphology of the integrated map for the approaching  $\text{H}_2\text{CO}$  gas has an east feature that includes CO clumps 1, 4 and 6. The southwest feature seen in the map of the approaching HCN gas is not obvious in the  $\text{H}_2\text{CO}$  map. The red half of the  $\text{H}_2\text{CO}$  line indicates that the south arc is very similar to the one seen in the red map of HCN. The south arc has two oppositely directed extensions. Enhanced intensity can be seen at the positions of clumps 5, 6 and 8. A common feature for all three of these molecules (CO, HCN,  $\text{H}_2\text{CO}$ ) is that they exhibit minimum emission at approximately the centre of the map.

In the lower portion of Figure 23 the integrated intensity of  $\text{H}_2\text{CO}$  emission for all velocities between 5.8 km/s and 15.3 km/s is presented. The emission peaks of  $\text{H}_2\text{CO}$  coincide with CO clumps 1, 2, 3, 4, 6 and 8. Thus, the distribution of the denser CO clumps is very similar to that of  $\text{H}_2\text{CO}$  gas.

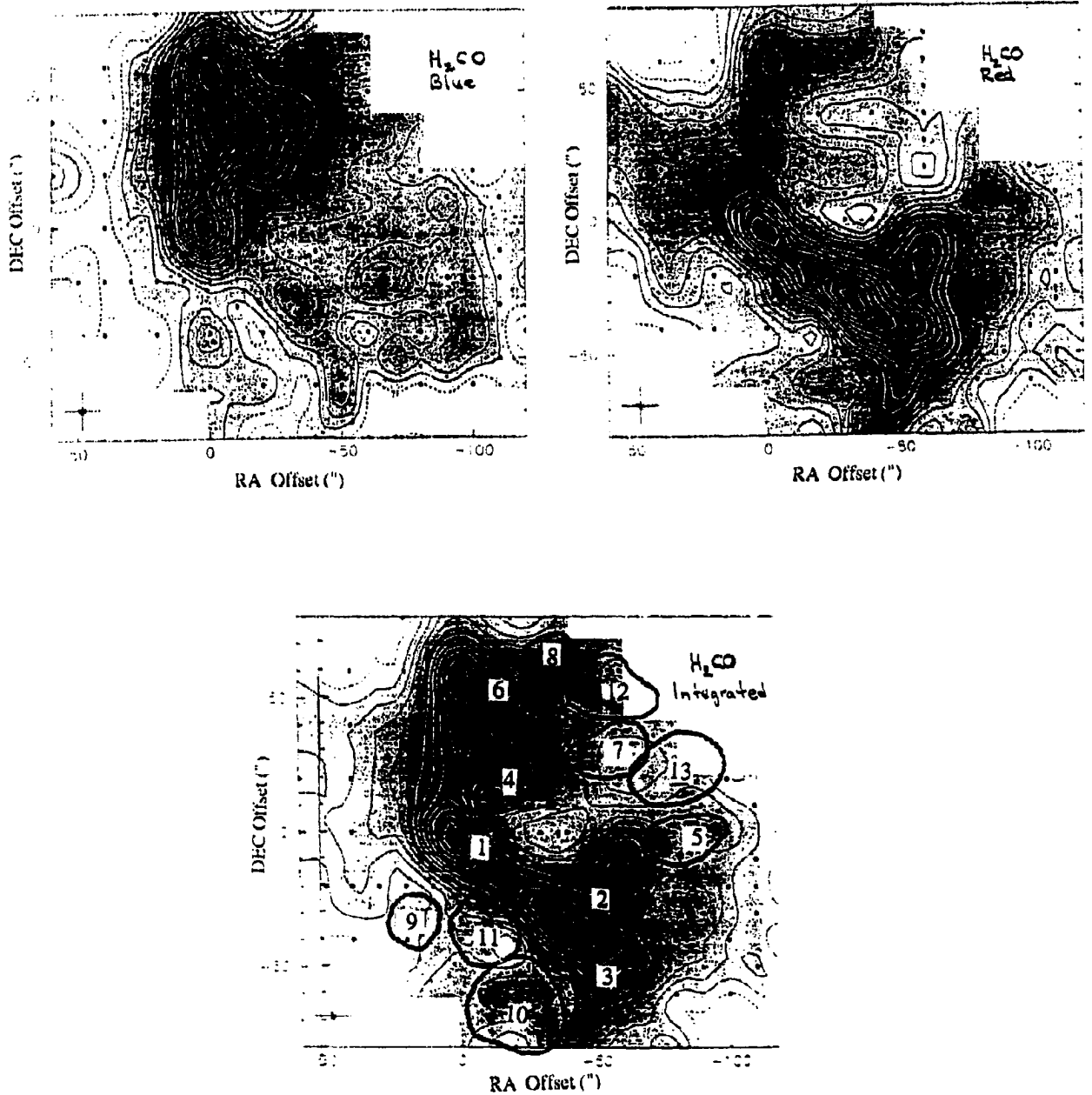


**Fig. 23** Integrated intensity maps of  $\text{H}_2\text{CO } J_{K_1K_2} = 5_{1,5} \rightarrow 4_{1,4}$  (351.7 GHz) (15" beam). The top left map is integrated intensity for all approaching (blue) velocities, i.e. between 5.8 km/s and 10.3 km/s. The top right map is integrated intensity for all receding (red) velocities between 10.3 km/s and 15.3 km/s. For both maps, the base level is -0.25 K km/s and the interval between contours is 0.25 K km/s. The lower map is the integrated intensity for all the observed velocities between 5.8 km/s and 15.3 km/s. The integrated  $\text{H}_2\text{CO}$  contours have a base level at -0.50 K km/s and the interval between contours is 0.50 K km/s. On this map we have superimposed the distribution of our CO clumps.

Since the H<sub>2</sub>CO transition is excited for densities in excess of 10<sup>6</sup> cm<sup>-3</sup> (Sasselov and Rucinski 1990), this similarity indicates again that the CO emission traces the dense gas. Also, we conclude from the low intensity near the centre of the H<sub>2</sub>CO map that very few molecules are present in this location. We will discuss this further when we analyze observations that are associated with the H II region.

It is interesting that the intensity from the northern extension is higher in the integrated H<sub>2</sub>CO map than in the HCN map. This feature is prominent in **Figure 23**. Also, the southwest structure is brighter in the H<sub>2</sub>CO map; this extension coincides with clump 3. It is possible that the differences seen in the structure of the integrated intensity of the HCN and H<sub>2</sub>CO emission could be due to abundance differences.

We summarize our conclusions deduced from comparing our CO maps with the maps of HCN J=4→3 and H<sub>2</sub>CO  $J_{K_1K_2} = 5_{1,5} \rightarrow 4_{1,4}$ . The integrated intensity maps of HCN and H<sub>2</sub>CO indicate the presence of three main intensity peaks that form a large emission arc which surrounds a circular region of minimum emission. The strongest peak coincides with IRS 3 and CO clump 1, the second enhancement is an extension towards the north (CO clumps 4 and 6), and the third peak (CO clump 2) is an extension to the southwest from the central peak. By comparing the CO map with the HCN and H<sub>2</sub>CO maps, we conclude that the CO J=3→2 transition is a fairly good tracer of dense gas. This is important, because it implies that the transition J=3→2 of CO is tracing the densest parts of the Mon R2 cloud core, even though the column densities are inaccurate near the line centre.

Although most of the CO clumps are detectable in HCN and H<sub>2</sub>CO emission, four clumps (7, 12, 13 in the northwest and clump 9 in the southeast) are present only in the CO maps. Their absence from the HCN and H<sub>2</sub>CO maps should be expected since their densities are between  $9.2 \times 10^2 \text{ cm}^{-3}$  and  $2.2 \times 10^4 \text{ cm}^{-3}$  (Table V), much less than the critical density needed to excite the high density tracers, typically over  $10^5 \text{ cm}^{-3}$ .

### 3) CS and HCO<sup>+</sup>

Both HCO<sup>+</sup> and CS are tracers of high-density gas. In what follows we discuss only the most recent high-resolution observations in CS and HCO<sup>+</sup> of the cloud core of Mon R2. Wolf et al. (1990) present a map of CS J=5→4 emission with a beam width of 23". Gonatas et al. (1992) obtained a high-resolution (9".8) interferometric map of HCO<sup>+</sup> gas in the J=1→0 transition. The two maps have northeast and southwest peaks that coincide well in position and size, separated by an intensity minimum. The overall extent of the CS emission is larger than that of HCO<sup>+</sup>. Gonatas et al. point out that lower resolution observations of a 4' x 4' field indicate that the true extent of HCO<sup>+</sup> emission is larger than suggested by their high-resolution map.

In Figure 24 we overlay our CO clump distribution on the HCO<sup>+</sup> (J=1→0) emission map. The two shades of grey in the HCO<sup>+</sup> map correspond to two intensity levels. Since HCO<sup>+</sup> is a tracer of high density gas, we expect the highest values of intensity to coincide with the clumps of highest density, which in Figure 24 are clumps 1, 2, 3, 4 and 6. These CO concentrations have densities in excess of  $10^5 \text{ cm}^{-3}$ . The only clump of large density ( $10^5 \text{ cm}^{-3}$ ) that does not appear in the darker regions of the HCO<sup>+</sup> (or HCN) map is clump 8.

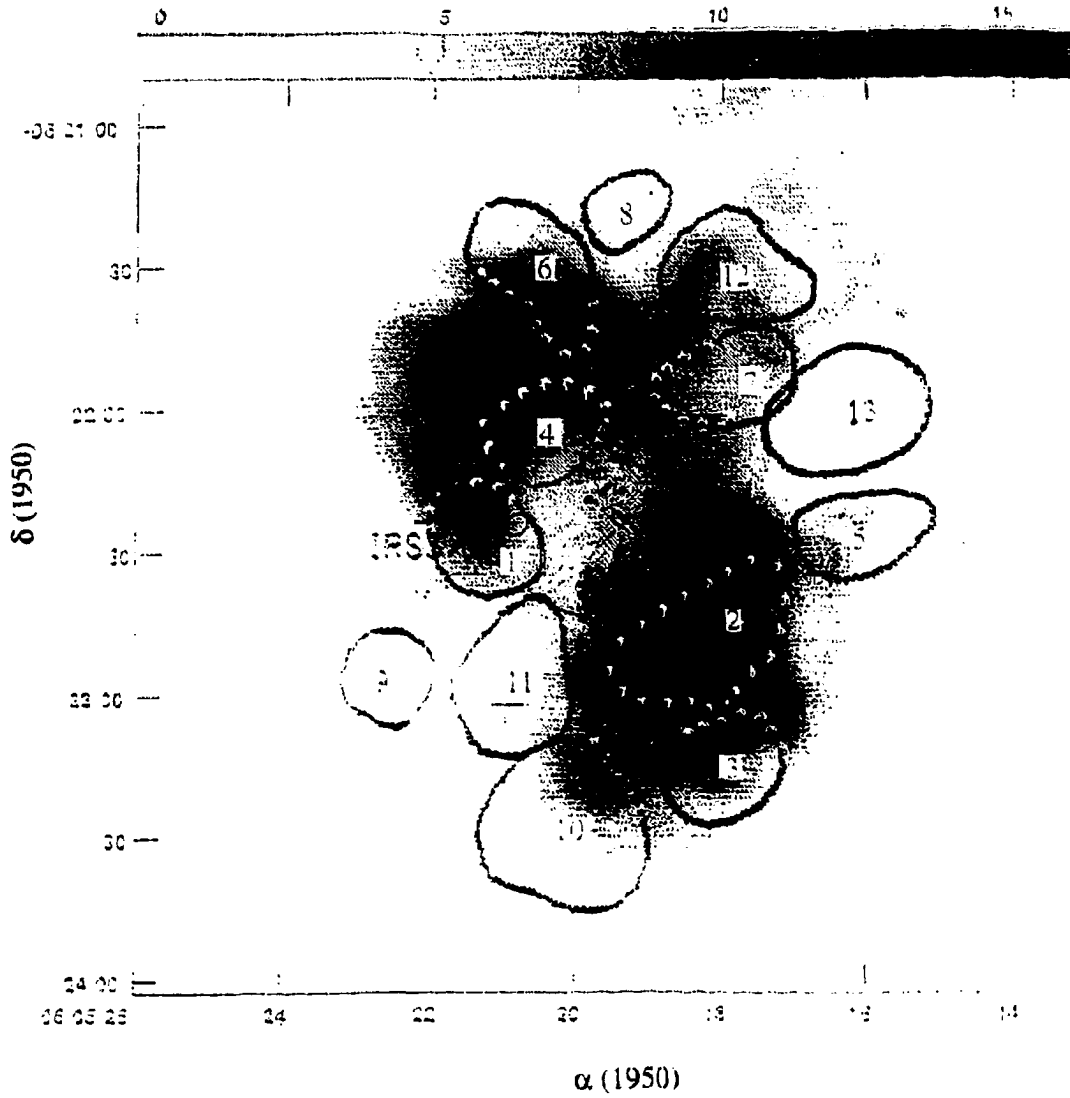


**Fig. 24** Our CO clump distribution is superimposed on the  $\text{HCO}^+$  ( $J=1 \rightarrow 0$ ) grey-scale map. The darkest regions of  $\text{HCO}^+$  are associated with CO clumps 1, 2, 3, 4 and 6.

This clump lies in a region of low  $\text{HCO}^+$  intensity, as do the clumps that have densities between  $10^3$  and  $7 \times 10^4 \text{ cm}^{-3}$ .

We compare the maps of HCN,  $\text{H}_2\text{CO}$  and  $\text{HCO}^+$  (Figure 22, 23 and 24). There is an intensity minimum in the centre of each map, surrounded by two arc-like structures (northeast and southwest). There are, however, some significant differences. Both HCN and  $\text{H}_2\text{CO}$  maps have their most prominent peak around IRS 3 (centered on  $0'', 0''$ ). IRS 3 is not prominent in the  $\text{HCO}^+$  map. Also, the south arc evident in HCN and  $\text{H}_2\text{CO}$  emission corresponds to a local minimum in  $\text{HCO}^+$  emission. Another difference among the dense gas tracers is that the intensity of the northwest link between the two features is relatively high in the  $\text{HCO}^+$  map, in contrast to the other two molecules, which show local minima. These differences in morphology are intriguing. Gonatas et al. (1992) attribute the difference in the apparent distribution of  $\text{HCO}^+$  compared to other tracers to a different chemistry for  $\text{HCO}^+$ . They invoke shock chemistry in the molecular outflow. Although shock chemistry cannot be ruled out, it seems unnecessary in view of the clear self-absorption in the  $\text{HCO}^+$   $J=1 \rightarrow 0$  transition. The  $\text{HCO}^+$  spectra exhibit throughout their map strong absorption at  $11.75 \text{ km/s}$ , very similar to the main absorption in CO, which occurs on average at  $11.3 \text{ km/s}$ . It indicates that the  $\text{HCO}^+$   $J=1 \rightarrow 0$  transition is optically thick. Such an absorption feature is not present in the HCN or  $\text{H}_2\text{CO}$  spectra. Therefore, we conclude that the morphology of the HCN and  $\text{H}_2\text{CO}$  maps is more representative of the location of the dense gas.

#### 4) $\text{NH}_3$

We have already mentioned the various low resolution studies of the  $\text{NH}_3$  (1,1) and  $\text{NH}_3$  (2,2) transitions (at 23.69 GHz and 23.72 GHz) in the Mon R2 region. In this discussion we focus only on high-resolution observations of the cloud core, as presented by Montalban et al. (1990) and Torrelles et al. (1990), with beam widths of 42" and 11", respectively.

The  $\text{NH}_3$  (1,1) emission map of Montalban et al. shows peaks that are displaced relative to the peaks in CO or HCN. More specifically, the peak in  $\text{NH}_3$  is about 1' east of the peak near IRS 3 seen in all molecules studied previously. Unfortunately, the maps of HCN and CO do not extend far enough to include the  $\text{NH}_3$  intensity peak south of the southwest peak seen in CO, HCN,  $\text{H}_2\text{CO}$  and  $\text{HCO}^+$ . However, we should note that all molecules share one common feature—their intensity drops quite dramatically in the region between the two peaks. The presence of this local minimum indicates that the molecules have been destroyed, which is not surprising since the area corresponds to the H II region. The interior of an H II region contains too much ultraviolet radiation for molecules to survive.

Torrelles et. al (1990) used the VLA with a resolution of  $\sim 3''$  for  $\text{NH}_3$  (1,1) and (2,2) observations of a  $2' \times 2'$  area. **Figure 25** shows our CO clump distribution superimposed on the  $\text{NH}_3$  maps. The contour map represents the integrated intensity of the (1,1) ammonia line and the grey-scale (although the contrast is not evident in these figures) corresponds to the integrated intensity of the (2,2) ammonia line. The superposition of the CO clumps on

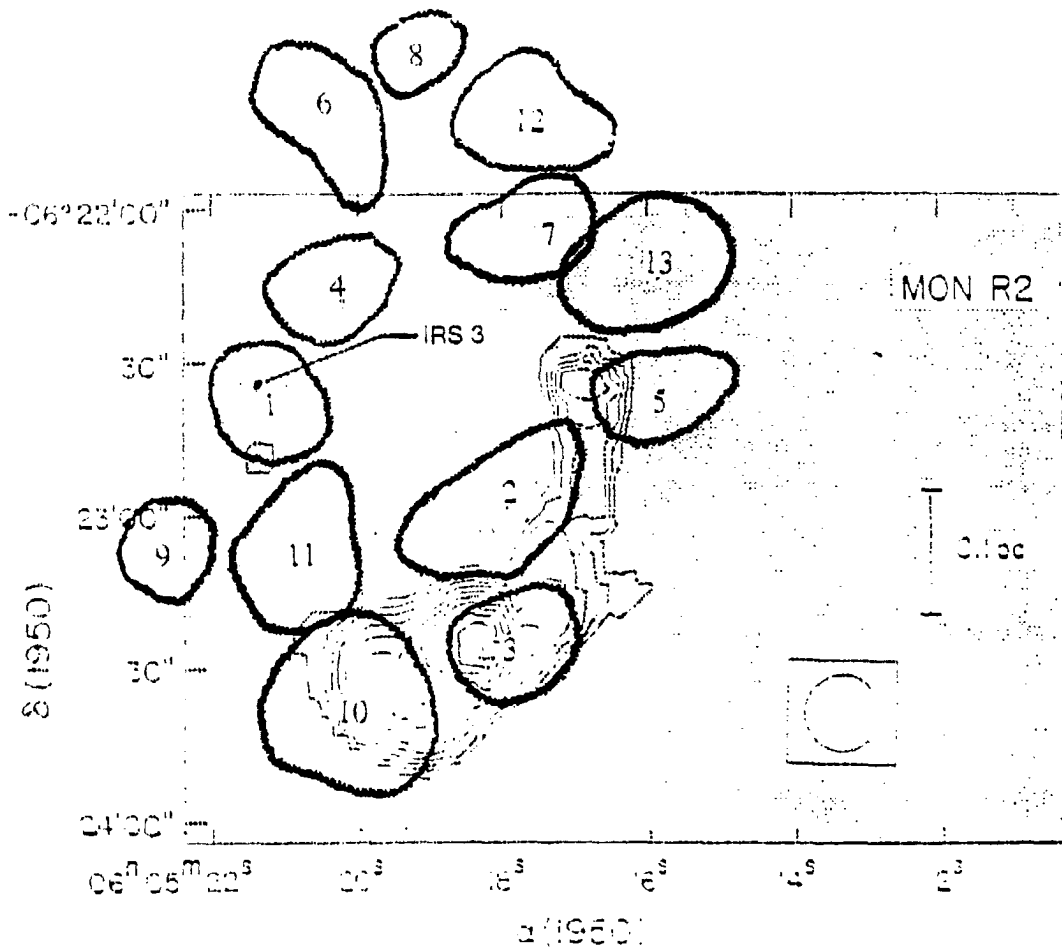


**Fig. 25** Our CO clump distribution superimposed on the VLA  $\text{NH}_3$  map (3"). The arc-like structure seen in the  $\text{NH}_3$  map, which is 40" to the southwest of the HII region, coincides with clumps 2, 3 and 10. The absence of  $\text{NH}_3$  from other parts of the map is surprising, since all other molecules show an intensity peak at IRS 3 (including  $\text{NH}_3$  from single-antenna work). The circle in the box represents the width of the VLA beam.

the ammonia maps shows that the  $\text{NH}_3$  structure is  $40''$  to the southwest of the H II region and coincides with clumps 2, 3 and 10. It is difficult to understand the absence of  $\text{NH}_3$  emission from other CO clumps. In particular, all other molecules peak in intensity at IRS 3 (including  $\text{NH}_3$  from single-antenna work).

In summary, the arc seen in high-resolution ammonia maps is south of the infrared cluster and the H II region; furthermore, these maps show no emission peaks where all the other studied molecules concentrate. Although the reason is not obvious, it should be noted that observations have indicated previously that ammonia maps can be very different from maps of other molecules. One example is L1551, which was observed by Wamsley and Wilson (1985). They found that the main ammonia peak is parallel to the outflow (which is true for Mon R2, too) and perpendicular to the intensity peak of CS. These differences might be due to real molecular abundance variations across the clouds.

*iii) Comparison of CO clump distribution with sub-millimeter and millimeter continuum maps*

There are two recently published studies of the cloud core of Mon R2 at sub-millimeter and millimeter continuum wavelengths by Walker et al. (1990) and by Henning et al. (1992). In the following discussion we include only the results of the latter, since the resolution is higher ( $18''$  and  $11''$ ) than in the former study (only  $30''$ ). **Figure 26** shows the  $870 \mu\text{m}$  continuum map ( $18''$  resolution) and the  $1300 \mu\text{m}$  high-resolution map ( $11''$ ) by Henning et al.

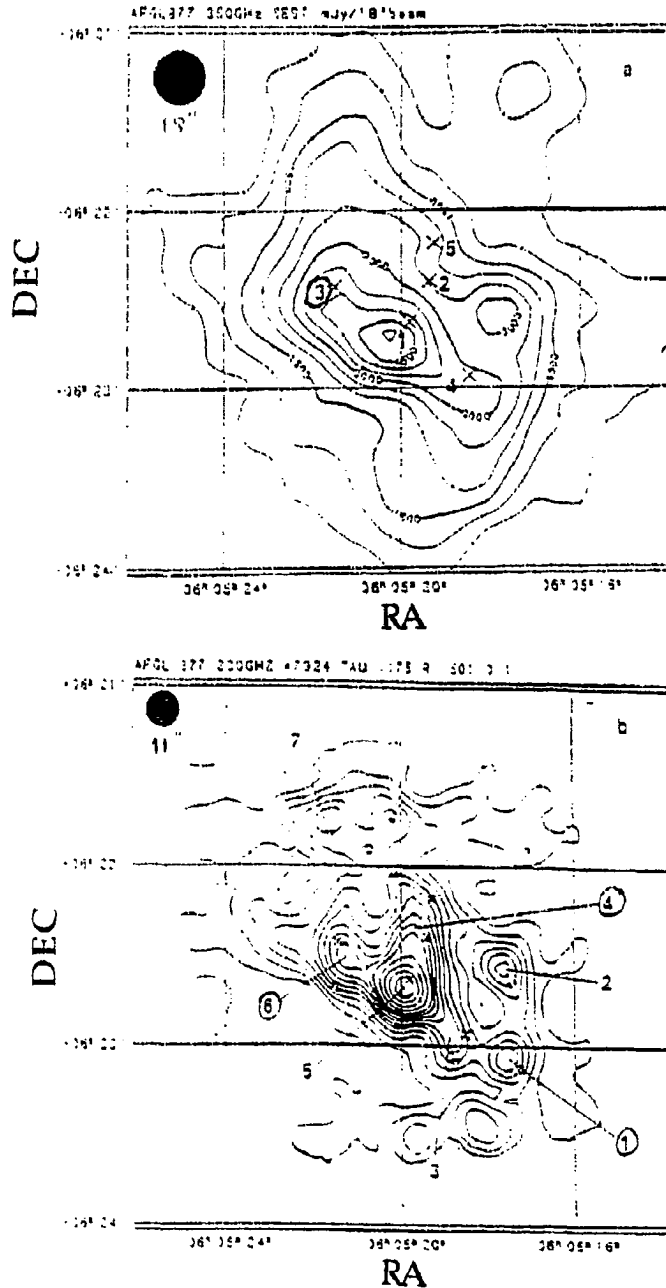


**Fig. 26** Sub-millimeter and millimeter continuum maps of the core of the Mon R2 cloud (adapted from Henning et al. 1992): (a) 870  $\mu\text{m}$  map with 18'' resolution and (b) a 1300  $\mu\text{m}$  map (11''). The contours in map (a) are scaled in units of Jy/beam. The crosses indicate the position of the infrared sources following Hackwell et al. (1982). Map (b) indicates the location of the clumps seen at this wavelength. The continuum clumps that are associated with our CO clumps are circled. The filled circles on the upper left corner represent the width of each beam used.

The crosses indicate the position of the infrared sources following Hackwell et al. (1982). In map (b), the location of the clumps seen at this wavelength are labeled. To avoid confusion with our CO clumps we will refer to the continuum clumps with italics.

In Figure 27 we also present four new sub-millimeter-millimeter maps: 450  $\mu\text{m}$  (14" resolution), 800  $\mu\text{m}$  (14"), 1100  $\mu\text{m}$  (20"), and 1300  $\mu\text{m}$  (25"). These were obtained at the JCMT by G. F. Mitchell and H. E. Matthews in November 1992. The 450  $\mu\text{m}$  and the 800  $\mu\text{m}$  maps agree very well with the 870  $\mu\text{m}$  of Henning et al. if the difference in resolution is considered. Our 1100  $\mu\text{m}$  map seems to agree better with the 1300  $\mu\text{m}$  map by Henning et al. than our 1300  $\mu\text{m}$  does. This is probably due to the fact that our 1300  $\mu\text{m}$  map has significantly lower resolution (25") than the Henning et al. map has (11"). All maps show emission that has a northeast-southwest direction. The central peak corresponds to the H II region.

The sub-millimeter maps show a considerably different intensity distribution from the millimeter maps. In the sub-millimeter maps there are three peaks: one is at the centre of the map and is on a common plateau of intensity with a second peak towards the east. The third peak is to the west. The shapes and relative intensities of these emission peaks, however, change with wavelength. At the millimeter wavelengths, the central peak is clearly the most intense one. Variation in the morphology of the maps with wavelength is evidence that the relative importance of the involved physical processes must be different. We will discuss this in further detail.

---

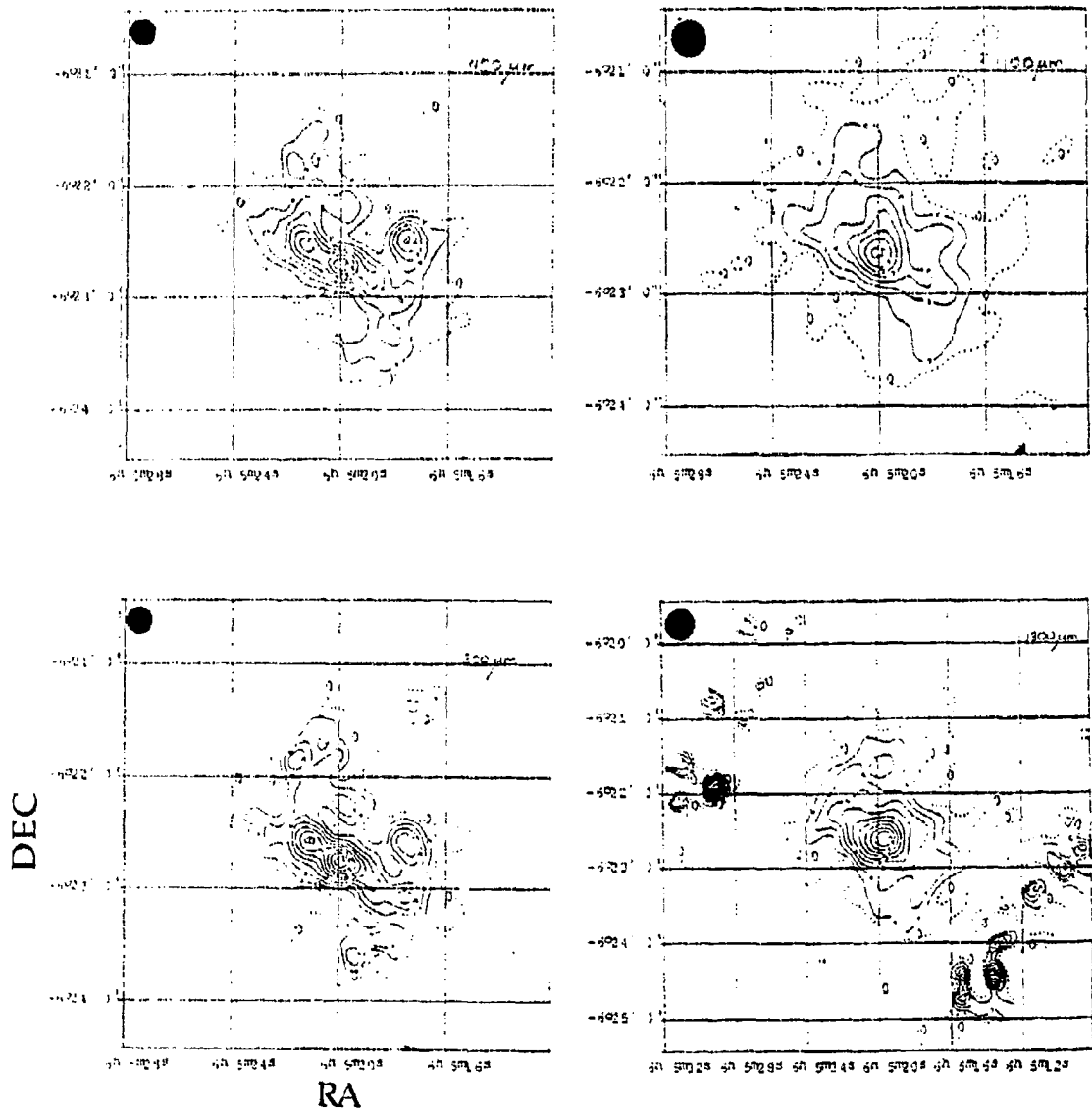


**Fig. 27** Our submm-mm maps: 450  $\mu\text{m}$  (14" resolution), 800  $\mu\text{m}$  (14"), 1100  $\mu\text{m}$  (20"), and 1300  $\mu\text{m}$  (25"). Note the different morphology seen in the submm and the mm maps. The central peak in the mm maps (1100  $\mu\text{m}$  and 1300  $\mu\text{m}$ ) corresponds in position and extent to the HII region. The filled circles on the upper left corner represent the width of each beam used.

**Figure 26** indicates that the central peak has a significant extension to the north. This extension is spatially close to the infrared source IRS 5. Aspin and Walther (1990) propose that IRS 5 is the outcome of the expansion of the H II region into a lower density medium than the rest of the ambient cloud. Therefore, this extension could be evidence for a blister model for the H II region.

Even if the north extension is due to the expanding H II region, how does that explain its absence from the sub-millimeter continuum maps? In order to address this issue, the various physical processes involved must be considered. Thermal dust emission is being traced in the sub-millimeter wavelengths; on the other hand, in the millimeter region, the free-free emission from the ionized gas becomes important. Walker et al. (1990) find that a 30" radius region (that includes IRS 5) has a significant contribution of free-free emission at 1300  $\mu\text{m}$  (5.3 Jy out of a total observed flux density of 22 Jy). Therefore, it is plausible that the extension coming from the H II region seen at 1300  $\mu\text{m}$  is due to the contribution of the free-free emission of the ionized gas, which is the reason it is not seen in the dust-tracing maps.

In order to compare the CO clump distribution with the continuum maps, we present in **Figure 28** our CO map overlain on the 800  $\mu\text{m}$  map. Our conclusions are the same for the 450  $\mu\text{m}$  map (our other two maps have too low resolution to be compared effectively). We see from the figure that a number of the CO clumps correspond to continuum clumps. Clump 1 corresponds to a distinct intensity peak in the continuum, which is slightly displaced towards the southwest from IRS 3 (its position is noted by a cross).

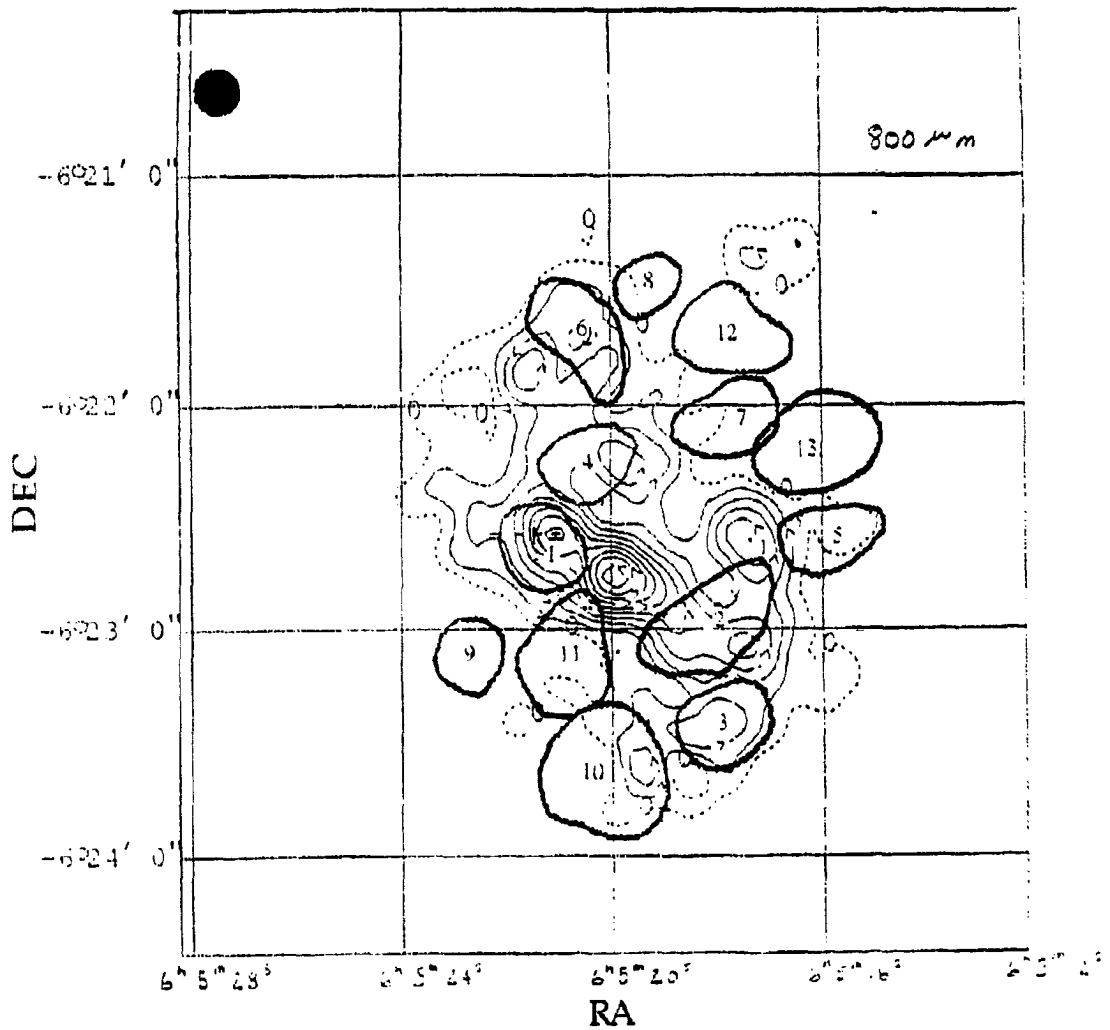


**Fig. 28** Our CO elump distribution superimposed on our 800  $\mu\text{m}$  contour map. A few CO elumps, namely 1, 2, 3, 4, 5 and 10, correspond fairly well to continuum clumps. The position of IRS 3 is noted by a cross. In the continuum map note a strong peak 1' west of the location of IRS 3, which is noted as elump 2 in the 1300  $\mu\text{m}$  map by Henning et al. The reason that this clump does not appear distinctly in the CO maps is not known. The filled circle on the upper left corner represents the width of the beam.

Clumps 2, 3 and 10 in CO roughly coincide with peaks in the southern extension of the continuum emission. CO clumps 4 and 6 correspond to continuum emission peaks to the north of IRS 3. Clumps 5, 7, 8, 9, 11, 12 and 13 do not coincide with the intensity peaks seen in the sub-millimeter and millimeter maps. The comparison between the CO and the continuum maps becomes more meaningful if we recall the CO clumps that are visible in the HCN and the H<sub>2</sub>CO maps. The high-density ( $n_{\text{H}_2} > 10^5 \text{ cm}^{-3}$ ) clumps 1, 2, 3, 4 and 6 are seen in all maps and clump 10 is seen in CO, and marginally in the HCN and the continuum maps. This reinforces our conclusion that the CO emission traces the location of most of the gas.

In our previous discussion we did not mention two intriguing features seen in **Figure 28**. Firstly, there is a strong feature in the continuum maps but not in the molecular line maps: a strong peak 1' west of the location of IRS 3 (the position of IRS 3 is indicated with a cross). This continuum peak is noted as clump 2 in the 1300  $\mu\text{m}$  map by Henning et al. (**Figure 26**). The continuum peak 1' west of IRS 3 is also present in the NH<sub>3</sub> and HCO<sup>+</sup> high resolution maps, but is at the edge of the HCN and H<sub>2</sub>CO distribution, without being a discrete "clump". The nature of the continuum clump is not obvious; it is different than IRS 3, because it does not appear in maps of all wavelengths. Although the CO maps show an enhancement close to its position (clump 5), there is no indication of a discrete clump. It is an open question why this clump does not appear distinctly in the CO maps.

Secondly, the major difference that emerges from the comparison of the continuum maps and the other molecular line maps is that the main central peak in the 800  $\mu\text{m}$  map is not detected in CO—or any other molecule

for that matter. The peak in the sub-millimeter and millimeter wavelengths at the position of IRS 1 corresponds to a local minimum in the molecular line maps. The presence of intense radiation at sub-millimeter and millimeter wavelengths from IRS 1 reinforces our interpretation that the position of the minimum seen in the molecular maps indicates a region where the molecules are photodissociated by ultraviolet radiation originating from the star that has created the H II region. Although there are no molecules in this region, the column density of dust is high, as shown from the intensity peak in the sub-millimeter and millimeter maps.

We superimpose the VLA continuum map at 1.3 cm by *Massi et al.* on our 450  $\mu\text{m}$  and 1100  $\mu\text{m}$  maps in **Figure 29** (i and ii). We believe that the displacement seen in the relative location of the two peaks in the 450  $\mu\text{m}$  map is real (**Figure 29 i**). The 450  $\mu\text{m}$  intensity peak is due south of the 1.3 cm peak. This displacement probably indicates that the dust column density is higher at the shell around the ionizing star than at the actual position of the star. The intensity peak seen at 1100  $\mu\text{m}$  corresponds exactly to the peak in the radio continuum map. This strongly suggests that the free-free emission is becoming increasingly important at millimeter wavelengths, and that dust emission is becoming less important. Therefore, radiation at 1100  $\mu\text{m}$  traces more closely free-free emission from ionized gas than the maps of shorter wavelengths. **Figure 29 ii** shows that there is a displacement between the position of IRS 3 as seen in the 2.2  $\mu\text{m}$  image (denoted with a cross) and the peak of the corresponding clump in the sub-millimeter continuum maps. This is also seen in the maps by *Henning et al. (1992)*. One interpretation could be that the dust associated sub-millimeter peak is displaced relative to the gas, because the dust is hotter closer to the H II region.

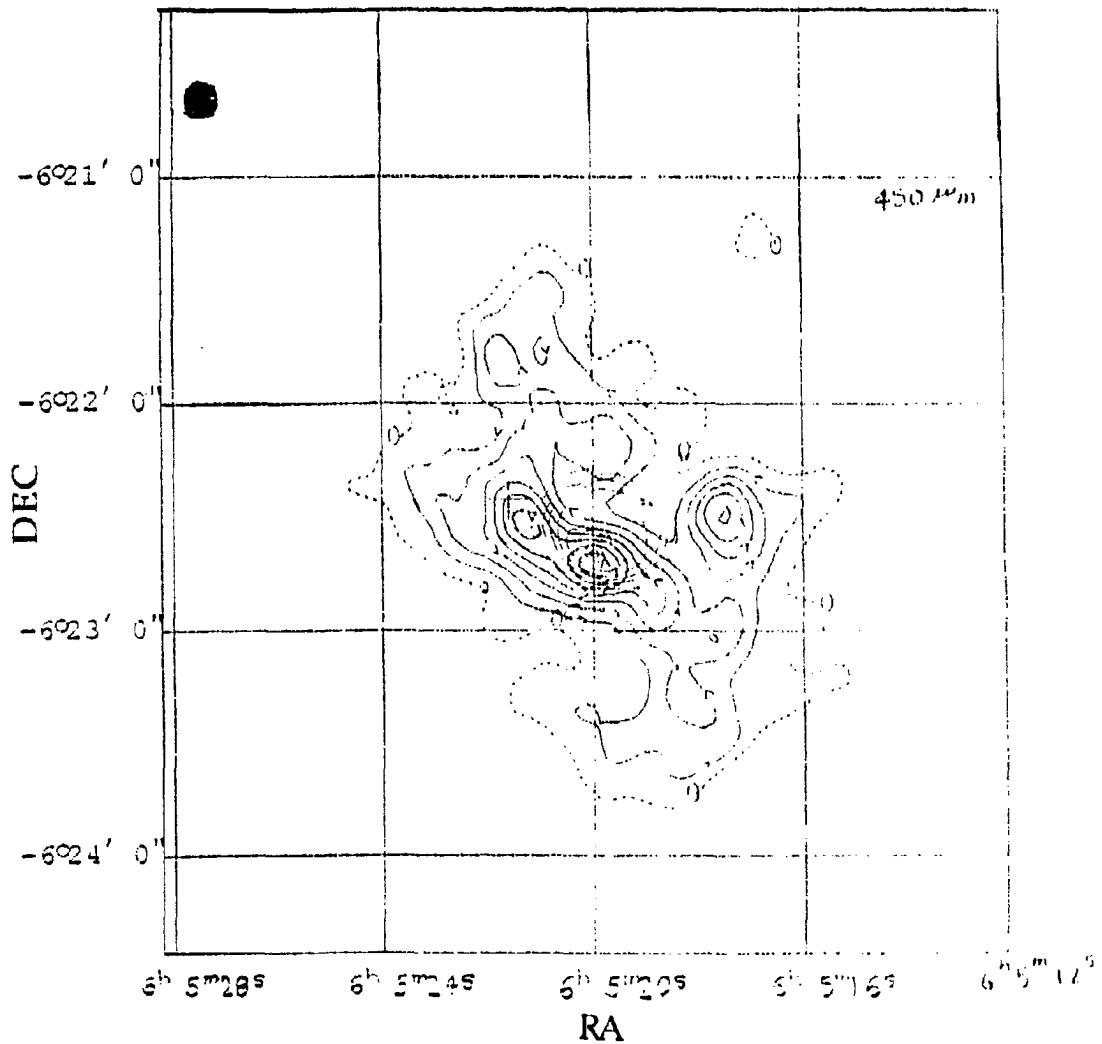


**Fig. 29 (i)** The VLA continuum map at 1.3 cm by Massi et al. superimposed on our 450  $\mu\text{m}$  map. The 450  $\mu\text{m}$  intensity peak is due south of the 1.3 cm peak, which indicates that the dust column density is higher at the shell around the ionizing star than at the actual position of the star. The position of IRS 3 as seen in the 2.2  $\mu\text{m}$  image (denoted with a cross) is displaced from the peak of the corresponding clump in the continuum maps seen in the 450  $\mu\text{m}$ . The displacement could be explained if the dust associated due to the heating of the dust close to the HII region. The filled circle on the upper left corner represents the width of our beam.

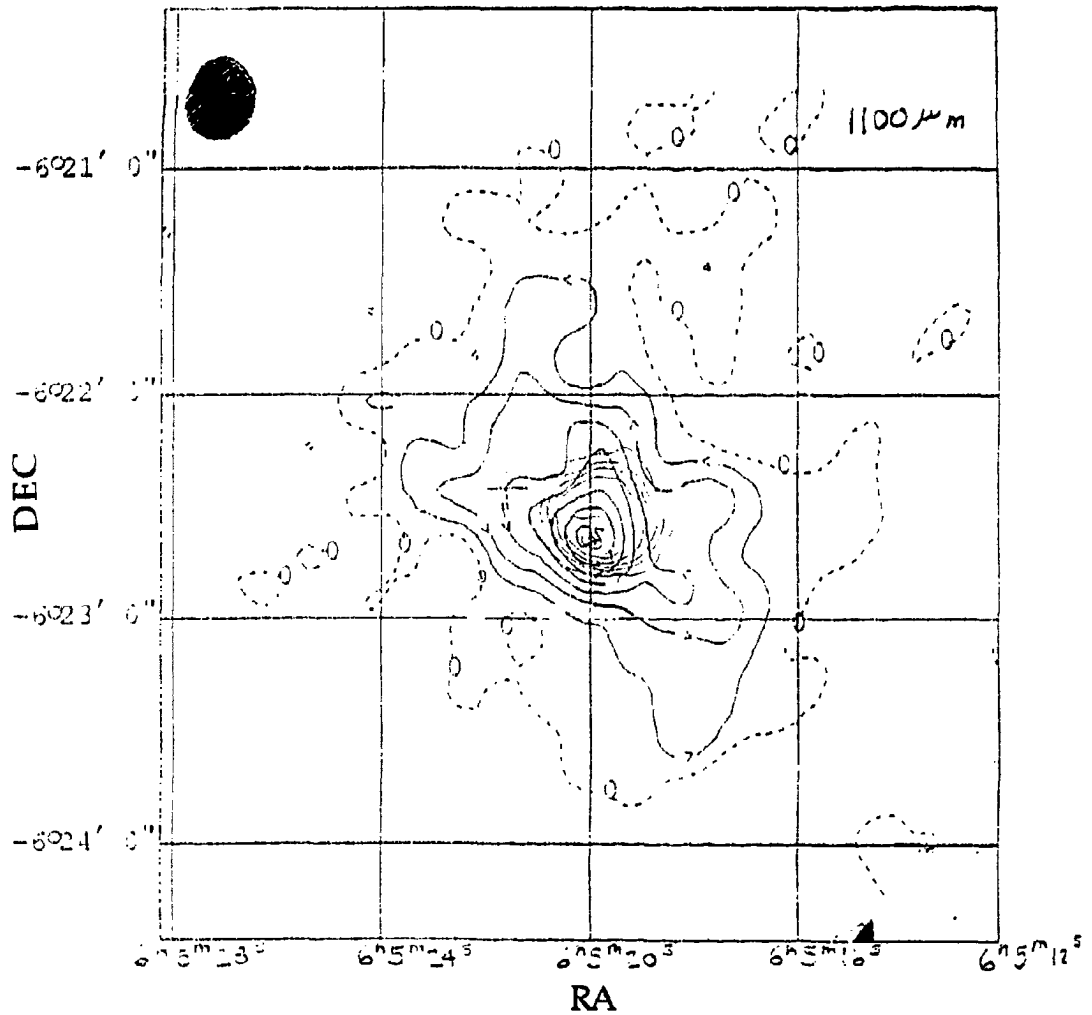


**Fig. 29 (ii)** The VLA continuum map at 1.3 cm by Massi et al. superimposed on our 1100  $\mu\text{m}$  map. The intensity peak seen at 1100  $\mu\text{m}$  corresponds exactly to the peak in the radio continuum map, which suggests that the radiation at 1100  $\mu\text{m}$  probes more closely free-free emission from the HII region than the maps of shorter wavelengths. The filled circles on the upper left corner represent the width of each beam used. The filled circle on the upper left corner represents the width of our beam.

The new sub-millimeter and millimeter maps presented here have not yet been calibrated, so they cannot be used quantitatively. Therefore, although we can compare our maps with the CO clump distribution and the other dense-gas tracers, we have to use the masses for the clumps seen at sub-millimeter and millimeter wavelengths calculated by Henning et al. These authors find seven clumps in their map, which we denote with italics so they can be distinguished from the CO clumps. They suggest that their clumps 2, 3, 4, 5, 6 are at the same position as the infrared sources *d*, IRS 4, IRS 2, IRS 1, and IRS 3. However, we find by carefully overlaying Aspin and Walther's 2.2  $\mu\text{m}$  image on the continuum map that, the coincidence between the infrared sources and the clumps on the continuum maps is not very good. We summarize in **Table VII** the CO clumps which are related to the continuum clumps and the infrared sources. The question mark signifies a case which is ambiguous in our opinion.

We compare the total CO column densities (i.e. the column density integrated over all velocities) for positions where both CO and continuum clumps are seen. Henning et al. calculate the total masses for the clumps for two dust temperatures: 20 K and 50 K, assuming a gas to dust ratio of 100. We use the masses for 50 K given by Henning et al. (to be justified later) and we measure the diameter of the continuum clumps to get a crude estimate of the total column density. Assuming that the abundance ratio of CO and H<sub>2</sub> is  $10^{-4}$ , we obtain the CO column density. These values of the column density have approximately 30% uncertainty, mainly due to the error in the measurement of each clump's diameter.

TABLE VII

POSSIBLE ASSOCIATIONS OF CO CLUMPS  
WITH CONTINUUM CLUMPS AND INFRARED SOURCES

Continuum clumps	CO clumps	Infrared sources
1	2	-
2	-	d?
3	-	IRS 4
4 ?	4	IRS 2? a <sub>i</sub> , a <sub>ij</sub>
5	-	IRS 1
6	1	IRS 3
7	-	-

We have already indicated that there are three clumps in the map of Henning et al. that coincide approximately with peaks seen in the CO emission map and with infrared sources in the 2.2  $\mu\text{m}$  image. We find that the total CO column density for clump 1 from CO is  $N_{\text{tot}}(\text{CO}) = 3.7 \times 10^{18} \text{ cm}^{-2}$  and at continuum clump 6,  $N_{\text{tot}}(\text{CO})$  is  $2.2 \times 10^{19} \text{ cm}^{-2}$ . At the position of clump 2,  $N_{\text{tot}}(\text{CO})$  is  $4.3 \times 10^{18} \text{ cm}^{-2}$  and at continuum clump 1,  $N_{\text{tot}}(\text{CO})$  is  $2.6 \times 10^{19} \text{ cm}^{-2}$ . Finally, at the position of clump 4,  $N_{\text{tot}}(\text{CO})$  is  $2.6 \times 10^{18} \text{ cm}^{-2}$  and at continuum clump 4,  $N_{\text{tot}}(\text{CO})$  is  $5.3 \times 10^{19} \text{ cm}^{-2}$ . For clumps 1 and 6, the column densities calculated from CO and continuum emission show a discrepancy of a factor of 6. Clump 4 has a column density that is 20 times smaller than that calculated for clump 4. Clump 4, however, is not very distinct in the continuum map and, furthermore, it is not as close to clump 4, as the other continuum clumps are close to their corresponding CO clumps. Therefore, we conclude that the ratio of the total column density calculated from the continuum and from CO is approximately 6. This indicates that although the CO can detect the position of the dense gas, it cannot reliably determine its total column density, because it is optically thick at the line core. It is almost certain that the column densities at the center of the CO line are underestimated due to the self-absorption of the gas.

*iv) Comparison of the column densities calculated from absorption lines in  $^{13}\text{CO}$  with those obtained from CO emission lines*

We briefly summarize another technique to calculate the total column density, which is based on  $^{13}\text{CO}$  fundamental band absorption lines at 4.7  $\mu\text{m}$

(transition from  $v = 0$  to  $v = 1$ ). Often the  $^{12}\text{CO}$  absorption lines are strongly saturated, and therefore they are not useful to obtain column densities. In such cases, fundamental band absorption lines of  $^{13}\text{CO}$  are unsaturated; thus, a curve-of-growth analysis can be used to obtain the total column densities of the absorbing gas. By definition, the equivalent width of the line is given by

$$W_\lambda = \int \left(1 - \frac{I_\nu}{I_c}\right) \cdot d\lambda, \quad (28)$$

where  $I_\nu$  is the intensity at frequency  $\nu$  and  $I_c$  is the intensity of the continuum.

Substituting  $d\lambda = \frac{\lambda^2}{c} d\nu$  and  $I_\nu = I_c e^{-\tau_\nu}$  in the previous expression (assuming no emission), we have

$$W_\lambda = \frac{\lambda^2}{c} \int (1 - e^{-\tau_\nu}) \cdot d\nu. \quad (29)$$

If the velocity distribution is Maxwellian, equation (29) can be written in the form (Spitzer, 1978)

$$\frac{W_\lambda}{\lambda} = \frac{2b}{c} F(\tau_0), \quad (30)$$

where  $b = \frac{\Delta\nu_{1/2}}{1.665}$  is the Doppler broadening parameter,  $\Delta\nu_{1/2}$  is the width measured at the half-intensity level, and by definition  $F(\tau_0)$  is:

$$F(\tau_0) \equiv \int_0^\infty [1 - \exp(-\tau_0 e^{-x^2})] \cdot dx. \quad (31)$$

The optical depth ( $\tau_0$ ) at the line centre is given by

$$\tau_0 = \frac{0.015}{b} N_j \cdot \lambda \cdot f_{jk}, \quad (32)$$

where  $N_j$  is the column density of the absorbing gas in the lower state and  $f_{jk}$  is the upward absorption oscillator strength from transition level  $j$  to level  $k$ .  $W_\lambda/\lambda$  and  $b$  can be measured from the spectra,  $I(\tau_0)$  is calculated using equation (30) and  $\tau_0$  is obtained using equation (31). Equation (32) can be used to derive the gas column density in the lower state.

In **Figure 30**, a portion of the spectrum of Mon R2 IRS 3 obtained by Mitchell and Maillard (1993) is presented. The analysis that follows was done by G. F. Mitchell. The mean  $^{13}\text{CO}$  line width is  $\Delta v_{1/2} = 3.5$  km/s, which corresponds to a Doppler broadening parameter of  $b = 2.1$  km/s. We present in **Table VIII** for each line the measured equivalent width,  $W_\lambda$ , the calculated line center optical depth,  $\tau_0$ , the ratio  $E_j/k$  (where  $k$  is the Boltzmann constant) and the column density at level  $J$ ,  $N_j$ . In order to calculate the total column density for all levels, it is necessary to determine the temperature of the gas. If the states are thermally populated then the Boltzmann equation applies. Thus, the plot of  $\ln[N_j/(2J+1)]$  versus  $E_j/k$  should yield a straight line with the gas temperature being the inverse of the slope. In **Figure 31** we present the excitation diagram, i.e. a plot of  $\ln[N_j/(2J+1)]$  versus  $E_j/k$ . This figure indicates that the gas has two components with different temperatures: 45 K and 310 K. The hotter component (310 K) is not detected by the CO  $J=3 \rightarrow 2$  transition. This is not surprising in view of **Figure 31**, which indicates that the emission from lower rotational states comes from the cool gas component. We will not discuss the hot component any further.

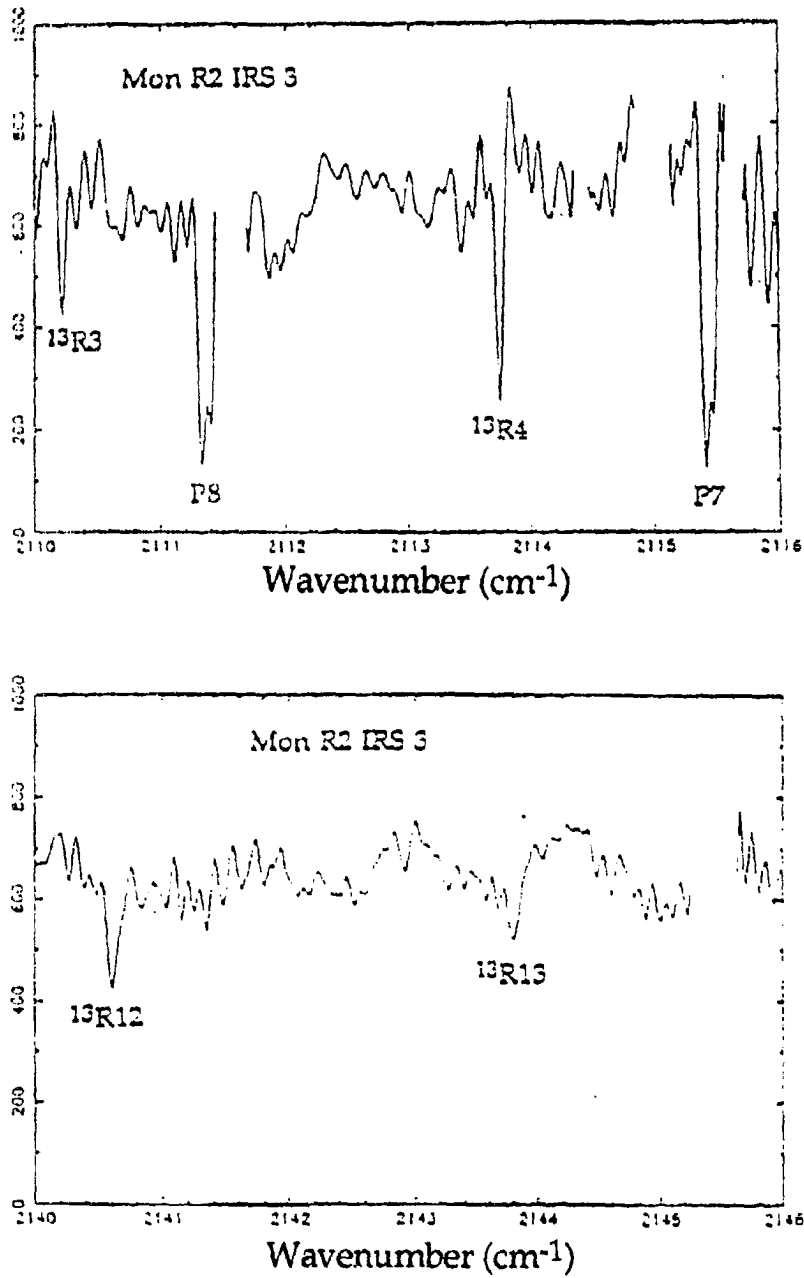


**Fig. 30** High-resolution (6.9 km/s) infrared M-band (4.7  $\mu\text{m}$ ) fundamental absorption spectrum in  $^{13}\text{CO}$  of IRS 3. This is used to calculate the column density towards IRS 3 and the temperature of the gas.

TABLE VIII

 $^{13}\text{CO } v=0 \rightarrow 1$  ABSORPTION LINES IN MON R2 IRS 3

Line	$W_\lambda(100 \text{ cm}^{-1})$	$t_0$	$E_j/k$	$N_j \text{ (cm}^{-2}\text{)}$
P4	31	1.26	52.9	$7.34 \times 10^{15}$
P3	40	4.4	31.7	$2.66 \times 10^{16}$
P2	39	4.1	15.9	$2.65 \times 10^{16}$
P1	27	1.76	5.3	$1.37 \times 10^{16}$
R2	37	3.4	15.9	$1.46 \times 10^{16}$
R4	28	1.86	52.9	$8.62 \times 10^{15}$
R5	35	3.0	79.3	$1.42 \times 10^{16}$
R6	23	1.33	111.0	$6.35 \times 10^{15}$
R9	22	1.22	237.8	$5.95 \times 10^{15}$
R10	21	1.15	290.6	$5.63 \times 10^{15}$
R11	19	0.98	348.7	$4.81 \times 10^{15}$
R12	16	0.77	412.1	$3.79 \times 10^{15}$
R13	14	0.65	480.8	$3.21 \times 10^{15}$
R15	14	0.65	633.9	$3.21 \times 10^{15}$

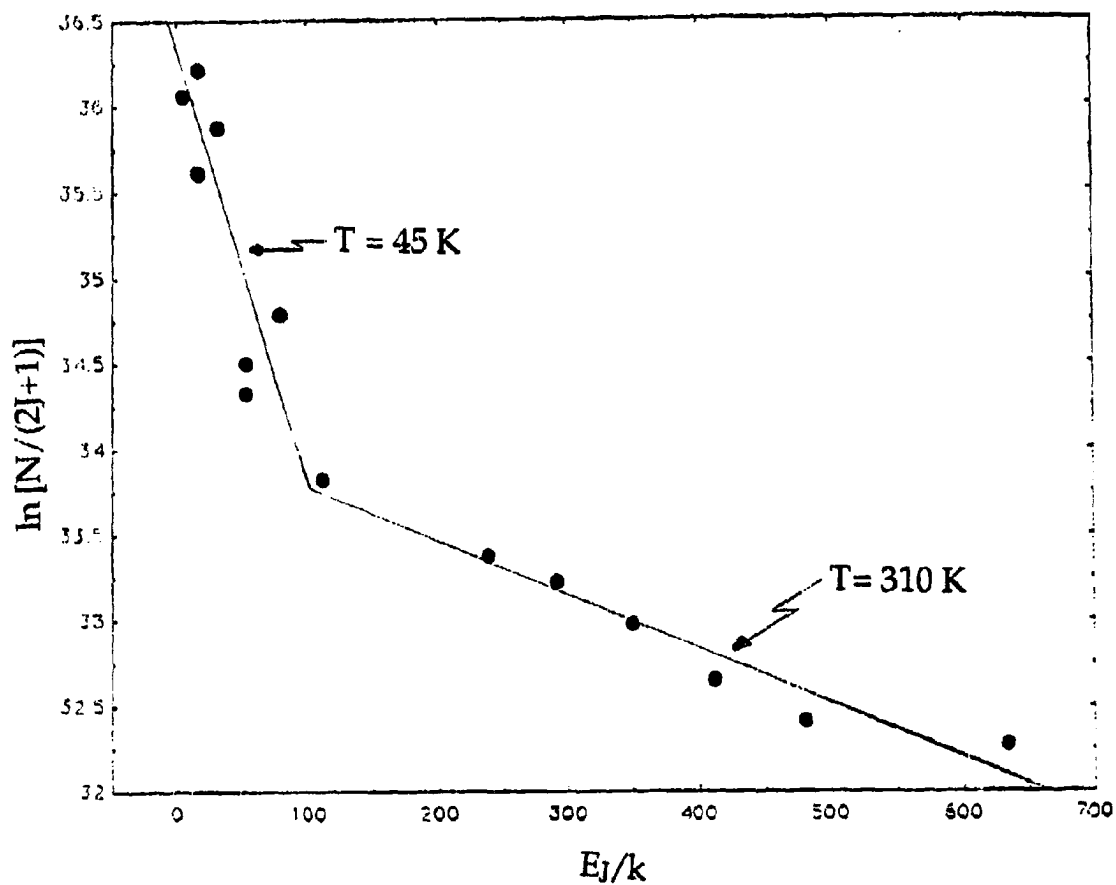


**Fig. 31** The excitation diagram for  $^{13}\text{CO}$  is a plot of  $\ln[N_j/(2j+1)]$  versus  $E_j/k$ . The two different slopes indicate that the gas has two components with different temperatures: 45 K and 310 K. The cooler component (45 K) is detected in  $^{12}\text{CO}$ , but the hotter component (310 K) is not detected by the  $\text{CO } J=3 \rightarrow 2$  transition.

The 45 K temperature of the cooler component from  $^{13}\text{CO}$  absorption agrees very well with other estimates of the gas temperature. It has been already mentioned that ammonia studies by Montalban et al. (1990) and Torrelles et al. (1990) find that the kinetic temperature in the cloud core is between 20 K and 30 K on average and it exceeds 45 K toward the position of the embedded infrared sources. Furthermore, far-infrared observations (30  $\mu\text{m}$ , 50  $\mu\text{m}$  and 100  $\mu\text{m}$ ) at the core of the Mon R2 cloud by Thronson et al. (1980) indicate that the size of the mapped region increases with increasing wavelengths. These authors interpret this trend as a natural result of the radial temperature gradient expected for a centrally heated dust cloud. According to their model, the hottest dust is found at the position of IRS 1, although a broad plateau extends to encompass IRS 3, IRS 2, and IRS 5. Beyond these sources, the grain temperature,  $T_g$ , drops rapidly. A mean value of  $T_g$  for the entire source estimated by Thronson et al. is 50 K. According to a more recent, 1 millimeter study of Chini et al. (1984) the dust temperature is 60 K. This value seems more appropriate than that of Thronson et al., if the gas ( $T_{\text{GAS}} \approx 45$  K) is warmed by the dust. This discussion indicates that our 45 K estimate of the gas temperature is very consistent with other observations.

Since we are confident about the deduced temperature, we can proceed with the  $^{13}\text{CO}$  absorption line analysis to calculate the average value of  $N(^{13}\text{CO})$ . Using that the gas temperature is 45 K, G. F. Mitchell finds that the total column density at the position of IRS 3 is  $N(^{13}\text{CO}) = 9.04 \times 10^{16} \text{ cm}^{-2}$ . This calculation, however, takes into account only the absorbing gas in front of IRS 3; if one assumes spherical symmetry then the column density should

be doubled. Furthermore, if the abundance ratio of  $^{13}\text{C}$  to  $^{12}\text{C}$  is equal to 60, then  $N_{\text{tot}}(^{12}\text{CO})$  is  $10.8 \times 10^{18} \text{ cm}^{-2}$ .

With the absorption technique one measures the column density of the quiescent gas in a narrow column with a subarcsecond diameter. With the sub-millimeter technique (continuum or line) one measures the column density of the quiescent gas in a sampling column with a large diameter. The continuum study yields for continuum clump 6 that  $N_{\text{tot}}(^{12}\text{CO})$  is  $2.2 \times 10^{19} \text{ cm}^{-2}$ . A discrepancy of a factor of 2 between them is not surprising given the different techniques. We believe that the absorption technique is the better one of the two, since there are fewer approximations needed than in the calculation of the column density from the continuum data.

The method of finding the column density from our CO emission observations has already been explained in detail. Thus, we calculate the total  $^{12}\text{CO}$  column density at the position of IRS 3, by summing the column densities for the whole range of velocities where CO is detectable at this position (0", 0"). We find that the total column density is  $N_{\text{tot}}(^{12}\text{CO}) = (3.7 \pm 0.5) \times 10^{18} \text{ cm}^{-2}$  at IRS 3. Note that the quoted error is the standard deviation of the calculated uncertainty of the column density due to the limited rms of the data. From the comparison of the total column density from CO with that from the other methods we conclude that the true uncertainty for our CO calculation of  $N_{\text{tot}}$  is considerably larger than the 15% error indicated from the error analysis.

A comparison of the total column density at the position of IRS 3 obtained from the CO emission clump,  $N_{\text{tot}}(^{12}\text{CO}) = 3.7 \times 10^{18} \text{ cm}^{-2}$ , with the

absorption line value,  $N_{\text{tot}}(^{12}\text{CO}) = 10.8 \times 10^{18} \text{ cm}^{-2}$ , indicates that the column density deduced from the CO observations is about 30% of the total mass in the line of sight. It has been suggested that CO locates the position of the dense gas because the CO clumps with deduced high density are also seen in the dense-gas tracers, such as HCN and H<sub>2</sub>CO. Therefore, although the CO emission does trace the location of the denser gas, it "sees" only ~30% of the total mass. This suggests that the masses of the clumps may be three times larger than what we find based on our CO emission observations (Table IV). However, this does not alter our conclusion that the clumps are dissipating.

#### b. CO high-velocity clumps and the large-scale CO outflow

It has been pointed out already that the CO clumps do not show any obvious bipolarity. They seem to be scattered in space, with no preference in any direction. These observations suggest that the moving clumps may presently not be directly related to the large outflow (28') seen in CO. On the other hand, the diffuse component seen in the CO channel maps (**Figure 32**) has a bipolar tendency, since the maps of approaching gas have a general enhancement to the northwest and some maps of receding gas show an enhancement to the southeast. The observed trend is consistent with the outflow mapped by Wolf et al. with a beam width of 90". This agreement is an indication that there is some connection between the present complex structure seen in the CO maps and the previously observed outflow.

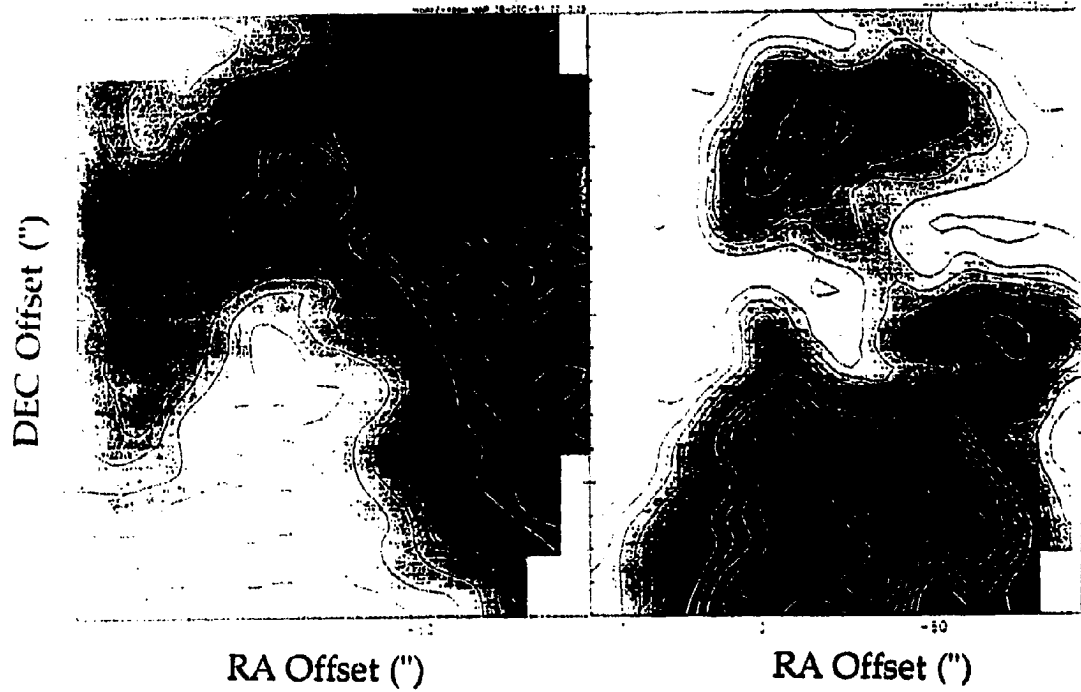


**Fig. 32** Integrated intensity maps for the velocity ranges of 9 to 10 km/s and 16.5 to 17 km/s. The approaching component of the diffuse gas is concentrated toward the northwest and the receding component is enhanced in the southeast.

The size and age of the outflow indicate that it must have injected large amounts of energy in the core region. We believe that the clumps formed from the interaction of the large outflow with the ambient gas due to hydrodynamical instabilities. Since the outflow is so old ( $10^5$  years) and extended, it is possible that the clumps are now free to move independently from the outflow.

The outflow probably originates from one of the infrared sources. None of the known infrared objects in the Mon R2 core, however, can be clearly labeled as the source. IRS 3 is surrounded by high-velocity gas. The motion of this gas shows no obvious preferred direction. It is possible that IRS 3 was responsible for the outflow but it consequently went through a quiescent phase; thus, in the vicinity of IRS 3 the motion of the gas can be determined by the characteristics (temperature and density) of the quiescent gas.

If the source of the outflow was IRS 3, we find that the time needed for the CO clumps to travel, with their bulk velocity, the distance to their current position is between  $2 \times 10^4$  years and  $4 \times 10^6$  years. The age of the outflow (see section c-ii in Chapter I) is estimated to be approximately  $10^5$  years. Therefore it is possible that the outflow is responsible for the motion of these clumps. Note that the time needed for the clumps to dissipate due their internal motions is  $2 \times 10^5$  years (see section e in Chapter V). Therefore, the clumps could have traveled to their present position without dissipating.

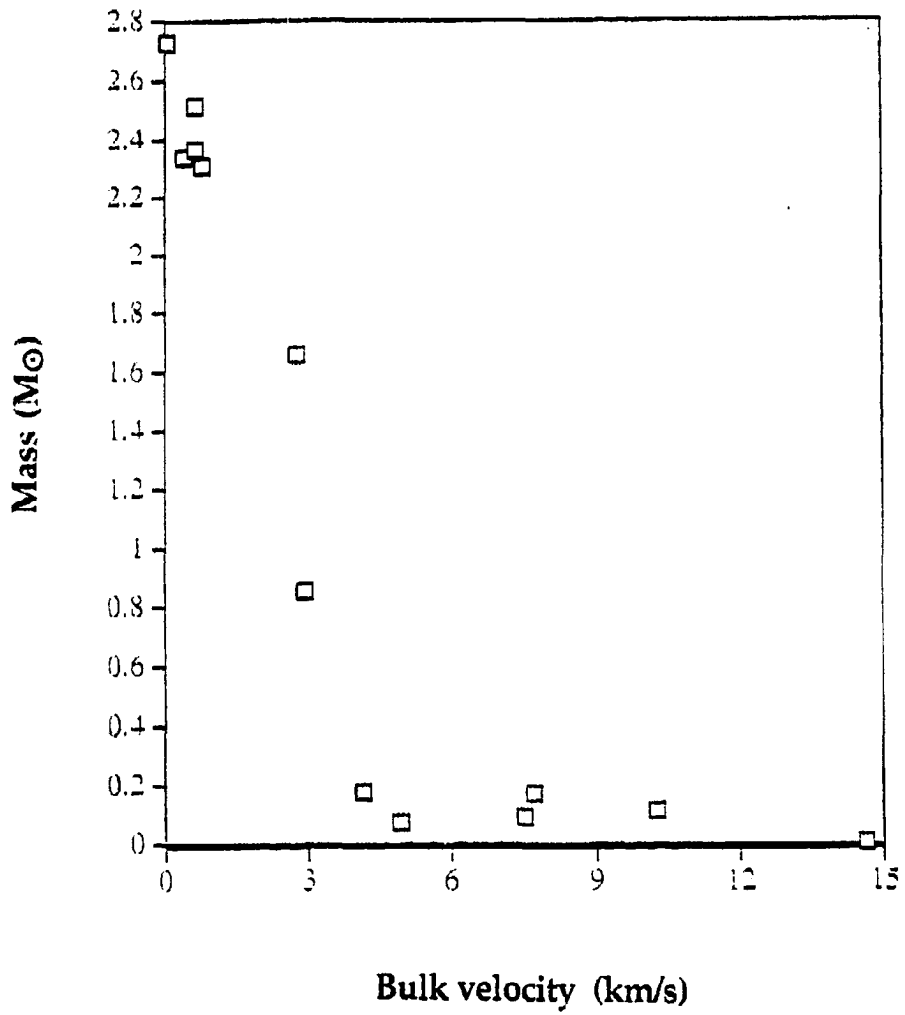


Fig. 33 The CO clump mass versus the bulk velocity of each clump ( $V_b$ ) from Table VI.

**Figure 33** shows the CO clump mass versus the bulk velocity of each clump with respect to the whole cloud. It is evident that the fastest CO clumps have the lowest masses. A model that could explain this velocity distribution of the clumps is proposed by Lada (1985) and Shu et al. (1991). A steady wind would make the small light clumps experience the largest acceleration and move farthest from the central source. CO  $J=2 \rightarrow 1$  observations of the outflow by Meyers-Rice and Lada (1991) with a beam width of 60" suggest that the velocity of the gas increases with increasing distance from IRS 1, which they consider to be the driving source of the outflow. Our higher resolution observations, however, do not indicate that the CO clumps are distributed in space according to ascending velocities; this may suggest that the current motion of the CO clumps is not determined by the larger outflow.

We have calculated that the gravitational binding energy is  $9.2 \times 10^{15}$  ergs, more than an order of magnitude smaller than the kinetic energy of the outflow found by Wolf et al., i.e.  $2.9 \times 10^{17}$  ergs. The large difference suggests that interaction between the outflow and the cloud core is capable of disrupting the cloud core.

## VII. CONCLUSIONS

In this thesis, the star forming core of the Mon R2 cloud is investigated using new, high spatial resolution observations. The new data include: an emission map of  $^{12}\text{CO}$   $J=3\rightarrow 2$ , emission lines at 12 positions for  $^{12}\text{CO}$   $J=2\rightarrow 1$  and  $^{13}\text{CO}$   $J=3\rightarrow 2$ , maps of  $\text{HCN}$   $J=4\rightarrow 3$  and  $\text{H}_2\text{CO}$   $J_{K_1, K_2} = 5_{1,5} \rightarrow 4_{1,3}$ , an infrared M-band spectrum, and finally sub-millimeter and millimeter continuum maps (450  $\mu\text{m}$ , 800  $\mu\text{m}$ , 1100  $\mu\text{m}$  and 1300  $\mu\text{m}$ ).

The results can be summarized as follows:

1. Emission in the  $^{12}\text{CO}$   $J=3\rightarrow 2$  transition shows structure on a variety of scales. The region is characterized by large-scale intensity enhancements (complexes) and by smaller emission peaks (clumps) within the complexes. We identify two different groups of complexes, one for the approaching gas and one for the receding gas. The complexes incorporate 13 smaller intensity peaks (clumps), some of which have large velocity dispersions. The CO clumps are not distributed in a bipolar fashion.
2. The strongest CO emission is distributed around a central area of lower intensity, which corresponds to the compact H II region in the cloud core. The H II region is deficient in molecules probably due to photodissociation, and hence corresponds to an intensity minimum in the molecular maps.

3. From  $^{12}\text{CO}$   $J=3\rightarrow 2$ ,  $J=2\rightarrow 1$ , and  $^{13}\text{CO}$   $J=3\rightarrow 2$  observations we find that the CO excitation temperature,  $T_{\text{ex}}$ , varies between 5 and 60 K. The lowest temperatures occur for the fastest moving gas; the reason is unclear. The agreement between the results using the optically thin and the optically thick methods is very satisfactory.
4. The masses of the clumps range from 2.7 to 0.007  $M_{\odot}$ , on average much larger than those observed in other clumpy outflows, which are typically between 0.5 and  $10^{-4}$   $M_{\odot}$ . The total gas mass of all CO clumps in the Mon R2 core is approximately 15  $M_{\odot}$ , which, although significant, is only 8% of the mass of the quiescent gas in this core ( $\approx 200 M_{\odot}$ ; Henning et al. 1992). Since the CO clumps are dissipating they are not in the process of forming stars.
5. The extended outflow must have injected large amounts of energy into the core region. We believe that the clumps formed from the interaction of the large outflow with the ambient gas. The fact, however, that our high resolution observations do not indicate that the CO clumps are distributed in space according to ascending velocities, suggests that the motion of the CO clumps is no longer determined by the larger outflow.
6. The strongest peak coincides with IRS 3 in the integrated intensity maps of HCN  $J=4\rightarrow 3$  and  $\text{H}_2\text{CO}$   $J_{K_1, K_2} = 5_{1,5} \rightarrow 4_{1,4}$  emission. These molecular maps are used as probes of dense gas since the transitions require high densities for their excitation. By comparing the CO map with the HCN and the  $\text{H}_2\text{CO}$  maps we conclude that the CO  $J=3\rightarrow 2$  transition traces the position of dense gas in Mon R2.

7. The common peak for all sub-millimeter and millimeter continuum maps (close to IRS 1) is spatially coincident with the H II region. We conclude that the IRS 1 peak seen in these maps is due to emission from dust in and around the H II region. Even though the central peak is almost at the same position, there are other features that are not common. One of these features is the enhanced emission seen at 1300  $\mu\text{m}$ , which is probably due to free-free emission from the H II region. Finally, another intriguing peak in the continuum maps is the clump seen 1' west of IRS 3. It also appears in HCO<sup>+</sup> and NH<sub>3</sub> maps, but has no distinct counterpart in CO, HCN or H<sub>2</sub>CO emission. This peak is different from that seen at the location of IRS 3, because it does not appear in maps of all wavelengths. The nature of this clump is not yet clear.
  
8. Analysis of <sup>12</sup>CO absorption lines in an infrared spectrum of IRS 3 indicates that the gas has two components with temperatures of 45 K and 310 K, respectively. The value of the temperature for the 45 K component is in accord with other estimates, including the one presented here from the CO J=3→2 transition. The column density toward IRS 3 deduced from the absorption lines is  $1.1 \times 10^{19} \text{ cm}^{-2}$ , which is in reasonable agreement with that derived from continuum emission,  $2.2 \times 10^{19} \text{ cm}^{-2}$ . The discrepancy of a factor of 2 could be due to approximations used for the latter calculation. If we compare these column densities (from the continuum maps and the infrared absorption) with the column density derived from our CO observations, we conclude that a large fraction of the dense quiescent gas (70-80%) is missed in the CO emission line analysis due to self-absorption.

9. The sum of the magnetic ( $3 \times 10^{45}$  erg) and the gravitational binding energy ( $9 \times 10^{45}$  erg) is somewhat smaller than the total kinetic energy of the inner core of the Mon R2 cloud ( $15 \times 10^{45}$  erg). Therefore, we conclude that, as a result of energy injected by star formation, the Mon R2 core could be either in the process of disruption or in a state of dynamical equilibrium.
  
10. The extended bipolar outflow probably originates from one of the infrared sources. None of the known infrared objects in the Mon R2 core, however, can be clearly identified as the source. The high-velocity gas around IRS 3 (the only infrared source associated with fast moving gas) does not show any obvious preferred direction or any clear connection with the extended outflow. Another possibility is that the originating source of the outflow is no longer active.

## REFERENCES

- André, Ph., Martin-Pintado, J., Despois, D., and Montmerle, T. 1990, *Astr. Ap.*, **236**, 180.
- Aspin, C., and Walther, D.M. 1990 a, *Astr. Ap.*, **235**, 387.
- Aspin, C., and Walther, D.M. 1990 b, *Astrophysics with Infrared Arrays* (eds. Elston).
- Bachiller, R., Cernicharo, J., Martin-Pintado, J., Tafalla, M., and Lazaroff, B. 1990, *Astr. Ap.*, **231**, 174.
- Bachiller, R., Martin-Pintado, J., Tafalla, M., and Planesas, P. 1991, *Astro and Ap*, **251**, 639.
- Bally, J., and Lada, C. J., 1983, *Ap. J.*, **265**, 824.
- Bally, J., and Stark, A. A., 1983, *Ap. J (Letters)*, **266**, L61.
- Beckwith, S., Evans II, N. J., Becklin, E. E., and Neugebauer, G., 1976, *Ap. J.*, **208**, 390.
- Bedijn, P.J. and Tenorio-Tagle, G., 1981, *Astr. Ap.*, **98**, 85.
- Bevington, P.R., 1969, *Data reduction and error analysis for the physical sciences*, New York: McGraw-Hill.
- Blitz, L., and Shu, F.H., 1980, *Ap. J.*, **238**, 148.
- Bodenheimer, P., Tenorio-Tagle, G., and Yorke, H.W., 1979, *Ap. J.*, **233**, 85.
- Chantry, G. W., 1979 *Modern Aspects of Microwave Spectroscopy*, (London: Academic Press Inc.).
- Chini, R., Kreysa, E., Mezger, P.G., and Gemund, H.-P., 1984, *Astr. Ap.*, **137**, 117.

- Downes, D., Winnberg, A., Goss, W.M., and Johansson, L.E.B., 1975, *Astr. Ap.*, **44**, 243.
- Ehrman, J.R., Dixon, R.S., and Kraus, J.D., 1970, *A. J.*, **75**, 351.
- Elmegreen, B.G. 1992, *Star Formation in Stellar Systems*, eds. G. Tenorio-Tagle, M. Prieto, and F. Sanchez (Cambridge: Cambridge University Press), p. 413
- Fukui, Y. 1989, *Low Mass Star Formation and Pre-main Sequence Objects*, ed. B. Reipurth (ESO: Munich), 95
- Garden, R.P., Hayashi, M., Gatley, I., Hasegawa, and T., Kaifu, N., 1991, *Ap. J.*, **374**, 540.
- Gilmore, W., 1980, *A. J.*, **85**, 912.
- Giovanardi, C., Lizano, S., Natta, A., Evans II, N.J., and Heiles, C., 1992, *Ap. J.*, **397**, 214.
- Gonatas, C.P., Palmer, P., Novak, G., 1992, *Ap. J.*, **398**, 118.
- Güsten, R., and Fiebig, D., 1988, *Astr. Ap.*, **204**, 253.
- Hackwell, J.A., Grasdalen, G.L., and Gehrz, R.D., 1982, *Ap. J.*, **252**, 250.
- Henning, T., Chini, R., and Pfau, W., 1992, *Astr. Ap.*, **263**, 285.
- Herbst, W., and Racine R., 1976, *A. J.*, **81**, 840.
- Heyer, M.H., Snell, R.L., Goldsmith, P.F., Strom, S.E., and Strom, K.M., 1986, *Ap. J.*, **308**, 134.
- Hodapp, K.-W., 1987, *Astr. Ap.*, **172**, 304.
- Hughes, V.A., and Viner M.R., 1976, *Ap. J.*, **204**, 55.
- Hughes, V.A., and Baines, J.G., 1985, *Ap. J.*, **289**, 238.
- Israel, F.P., 1978, *Astr. Ap.*, **70**, 769.
- Knapp, G.R., and Brown, R.L., 1976, *Ap. J.*, **204**, 21.
- Königl, A., 1982, *Ap. J.*, **261**, 115.
- Kutner, M.L., and Tucker, K.D., 1975, *Ap. J.*, **199**, 79.
-

- Lada, C.J., and Wilking, B.A., 1984, *Ap. J.*, **287**, 610.
- Lada, C.J., 1985, *Ann. Rev. Astron. Astrophys.*, **23**, 267.
- Langer, W.D., and Penzias, A.A. 1990, *Ap. J.*, **357**, 477.
- Lee, S.-W. 1992, M. Sc. Thesis.
- Lizano, S., Heiles, C., Rodriguez, L.F., Koo, B.-C., Shu, F.H., Hasegawa, T.,  
Hayashi, S., and Mirabel, I.F. 1988, *Ap. J.*, **328**, 763
- Loren, R.B., Peters, W.L., and Vander Bout, P.A., 1974, *Ap. J. (Letters)*, **194**,  
L103.
- Loren, R.B., 1977, *Ap. J.*, **215**, 129.
- Macdonald, G.H., Little, L.T., Brown, A.T., Riley, P.W., Matheson, D.N., and  
Felli, M., 1981, *M.N.R.A.S.*, **195**, 387.
- Maddalena, R.J., Morris, M., Moscowitz, J., and Thaddeus, P., 1986, *Ap. J.* **303**,  
375.
- Massi, M., Felli, M., and Simon, M., 1985, *Astr. Ap.*, **152**, 387.
- Matthews, H.E., May 1, 1992, *The James Clerk Maxwell Telescope: A guide for  
the Prospective User* (Hilo, Hawaii: Joint Astronomical Centre).
- Meyers-Rice, B.A., and Lada, C.J., 1991, *Ap. J.*, **368**, 445.
- Mitchell, G.F., 1992 in press
- Mitchell, G.F. and Maillard, J.-P. 1993 in press
- Mitchell, G.F., Lee, S.W., Maillard, J.-P., Matthews, H.E., Hasegawa, T.I., and  
Harris, A.I., 1993, *Ap. J.*, in press.
- Montalban, J., Bachiller, R., Martin-Pintado, J., Tafalla, M., and Gomez-  
Gonzalez, J., 1990, *Astr. Ap.*, **233**, 527.
- Myers, P.C., 1985, *Protostars and Planets II*, eds. D.C. Black and M.S.  
Matthews (Tucson, Arizona: The University of Arizona Press).
- Myers, P.C., 1987, *IAU 33, Star Forming Regions*, eds M. Peimbert and J.  
Jugaku.

- Natta, A., Beckwith S., Evans II, N.J., Beck, S.C., Moorwood, A.F.M., and Oliva, E., 1986, *Astr. Ap.*, **158**, 143.
- Norman, C. and Silk, S., 1980, *Ap. J.*, **238**, 158.
- Padman, R. 1988, *SPECX V5.3 Users' Manual* (Cambridge: Cavendish Laboratory).
- Panagia, N., 1973, *A. J.*, **78**, 929.
- Pudritz, R.E., and Norman, C.A., 1983 *Ap. J.*, **274**, 677.
- Pudritz, R.E., 1985, *Ap. J.*, **293**, 216.
- Racine, R. 1968, *A. J.*, **73**, 233.
- Racine, R., and van den Bergh 1970, IAU, *The Spiral Structure of Our Galaxy*, 219.
- Richardson, K.J., White, G.J., Monteiro, T.S., and Hayashi, S.S. 1988, *Astr. Ap.*, **198**, 237.
- Rubin, R.H. 1968, *Ap. J.*, **154**, 391.
- Sasselov, D., and Rucinski, S. 1990, *Ap. J.*, **351**, 578.
- Shimmins, A.J., Clarke, M.E., and Ekers, R.D. 1966, *Australian J. Phys.*, **19**, 649.
- Shu, F.H., Adams, C.A., and Lizano, S. 1987, *Ann. Rev. Astron. Astrophys.*, **25**, 23.
- Shu, F.H., Ruden, S.P., Lada, C.J., and Lizano, S. 1991, *Ap. J. (Letters)*, **370**, L31.
- Snell, R.L., 1987, *IAU 115, Star Forming Regions*, eds. M. Peimbert, J. Jugaku, 213.
- Spitzer, L., Jr. 1978, *Physical Processes in the Interstellar Medium* (New York: Wiley).
- Thronson, H.A., Gatley, I., Harvey, P.M., Sellgren, K., and Werner, M.W. 1980, *Ap. J.*, **237**, 66.
- Tirion, W., Rappaport, B., and Lovi, G. 1992, *Uranometriu 2000.0, Volume II*, Library of Congress Cataloguing-in Publication Data, 271.

- Torrelles, J.M., Rodriguez, L.F., Cantó, J., Carral, P., Marcaide, J., Moran, J.M., and Ho, P.T.P., 1983, *Ap. J.*, **274**, 214.
- Torrelles L.F., Ho, P.T.P., J.M., Rodriguez, and Cantó, J., 1990, *Ap. J.*, **349**, 529.
- van den Bergh, S., 1966, *A. J.*, **71**, 990.
- van der Werf, P.P., Dewdney, P.E., Goss, W.M., and Vanden Bout, P.A. 1989, *Astr. Ap.*, **216**, 215.
- Walker, C.K., Adams, F.C., and Lada, C.J. 1990, *Ap. J.*, **349**, 515.
- Walmsley, C.M., and Wilson, T.F. 1990, European Regional Symp. of the IAU, Toulouse, 1984, *Nearby Molecular Clouds*, Springer, Berlin Heidelberg New York.
- Willson, R.F., and Folch-Pi, F.J., 1981, *A. J.*, **86**, 1084.
- Wolf, G.A., Lada, C.J., Bally, J., 1990, *A. J.*, **100**, 1892.
- Wood, D.O.S., and Churchwell, E., 1989, *Ap. J. Suppl. S*, **69**, 831.
- Zuckerman, B., and Palmer, P., 1974, *Ann. Rev. Astron. Astrophys.*, **12**, 279.

**CIRRICULUM VITAE**

**Name:** Jean Giannakopoulou

**Birthplace:** Toronto, Canada

**Birthday:** September 18, 1967

**Post-Secondary Education:** B. Sc. (Honours), 1991  
University of Athens  
Athens, Greece

M. Sc., 1993  
Saint Mary's University  
Halifax, Nova Scotia, Canada

**Awards:** Saint Mary's University Graduate Fellowship  
1992-1993

**Experience:** Observatory Assistant  
Burke-Gaffney Observatory  
Saint Mary's University 1991-1992

Research/Teaching Assistantships  
Saint Mary's University 1992-1993

---

**Observing run at the 15-m James Clark Maxwell Telescope  
Mauna Kea, Hawaii 1992**